

IMAGE BASED COMPUTATIONAL HEMODYNAMICS FOR NON-INVASIVE
AND PATIENT-SPECIFIC ASSESSMENT OF ARTERIAL STENOSIS

A Thesis

Submitted to the Faculty

of

Purdue University

by

Md Mosnurul Islam Khan

In Partial Fulfillment of the

Requirements for the Degree

of

Master of Science in Mechanical Engineering

August 2019

Purdue University

Indianapolis, Indiana

THE PURDUE UNIVERSITY GRADUATE SCHOOL
STATEMENT OF THESIS APPROVAL

Dr. Huidan Yu, Chair

Department of Mechanical and Energy Engineering

Dr. Likun Zhu

Department of Mechanical and Energy Engineering

Dr. Diane Wagner

Department of Mechanical and Energy Engineering

Approved by:

Dr. Sohel Anwar

Chair of the Graduate Program

To my beloved parents and brother

ACKNOWLEDGMENTS

First, I would like to thank Almighty Allah for giving me strength, ability and opportunity to involve in this research, to hold on and finish. I express my sincere gratitude to my thesis supervisor, Dr. Whitney Yu, for her guidance, cooperation, motivation and support to the completion of my thesis. I found her as a person of vast knowledge and capable of critical problem-solving. I would like to thank her for keeping the faith in my hard time over the research and motivate me until the end of my thesis. I thank my lab-mates Rou Chen, Anurag Deb, Xiaoyu Zhang, Arya Abootorabi, Xin Jin for their valuable time and support towards my research. Anurag Deb helped me to start my research and give me idea about different useful software to execute different purposes. I got immense help from Rou Chen during the set up of numerical model and execution. They were always ready to help and kept me motivated during the tough time. I am grateful to my parents for their support and for being source of inspiration to pursue my dream. Without their continuous encouragement, this accomplishment would never come true.

PREFACE

The research pioneers a new and reliable noninvasive means, named *InVascular*, to assess the true severity of arterial stenosis based on patients radiological imaging data and thereby predict the benefits of vascular stenting to the patients. *InVascular* is robust, applicable for renal, coronary, carotid, cerebral, iliac, femoral, and mesenteric vascular beds, computing pressure gradients and flow changes prior to and after potential vascular interventions helping to guide successful vascular therapy. The preliminary results of this research demonstrate the reliability and clinical applicability of *InVascular*.

TABLE OF CONTENTS

	Page
LIST OF TABLES	viii
LIST OF FIGURES	ix
SYMBOLS	xiii
ABBREVIATIONS	xiv
ABSTRACT	xvi
1. INTRODUCTION	1
1.1 Stenosis	1
1.1.1 Renal Arterial Stenosis	1
1.1.2 Coronary Arterial Stenosis	3
1.2 Computational Hemodynamics	4
1.3 Objective	6
2. METHODOLOGY	7
2.1 Segmentation of artery	7
2.2 Lattice Boltzmann method for Computational Fluid Dynamics	10
2.3 Boundary conditions	13
2.3.1 Inlet boundary condition	14
2.3.2 Outlet boundary condition, WK3 model	16
2.3.3 Outlet boundary condition, lumped parameter network model for coronary outlet	17
2.4 Integration of outlet boundary conditions	22
2.5 Parametrization for stenosis severity	25
2.6 Patient cases	25
3. APPLICATION STUDY : PATIENT SPECIFIC COMPUTATIONAL HEMO- DYNAMICS IN ARTERIAL SYSTEMS	28
3.1 Aortorenal arterial system	28
3.1.1 Case I	29
3.1.2 Case II	35
3.1.3 Case III	40
3.1.4 Case IV	46
3.1.5 Case V	51
3.2 Statistical analysis	56
3.3 Coronary artery	57

	Page
4. ASSESSMENT OF TRUE SEVERITY OF ARTERIAL STENOSIS AND THERAPEUTIC GUIDELINES	63
4.1 Characterization of stenosis degree : lumen diameter vs. volume reduction	63
4.2 Assessment of true severity of RAS	63
4.2.1 Case IV-left renal artery	66
4.2.2 Case IV-right renal artery	69
4.2.3 Case V	72
4.2.4 Case VI	75
4.3 Assessment of true severity of coronary arterial stenosis	78
5. SUMMARY	81
REFERENCES	84
VITA	90

LIST OF TABLES

Table	Page
2.1 Study Cases for Renal Artery	26
3.1 Values of resistances and compliances parameters in WK3 model at corresponding outlet of Case I	31
3.2 Comparison of TSPG in LRA and RRA based on MAP or p_{sys} in Case I	33
3.3 Values of resistances and compliances parameters in WK3 model at corresponding outlet of Case II	36
3.4 Comparison of TSPG in LRA and RRA based on MAP or p_{sys} in Case II	36
3.5 Values of resistances and compliances parameters in WK3 model at corresponding outlet of Case III	41
3.6 Comparison of TSPG in LRA and RRA based on MAP or p_{sys} in Case III	41
3.7 Values of resistances and compliances parameters in WK3 model at corresponding outlet of Case IV	47
3.8 Comparison of TSPG in LRA and RRA based on MAP or p_{sys} in Case IV	49
3.9 Values of resistances and compliances parameters in WK3 model at corresponding outlet of Case V	52
3.10 Comparison of TSPG in LRA and RRA based on MAP or p_{sys} in Case V	54
3.11 Values of resistances and compliances parameters in LPN model at coronary outlet	60
3.12 Values of resistances and compliances parameters in ascending aorta outlet	60
3.13 Comparison of MAP and FFR in the LCX artery	62
4.1 Varying volume reduction from 38% to 60% for an RAS with fixed diameter reduction (75%)	64
4.2 Varying diameter reduction from 53% to 69% for an RAS with fixed volume reduction (45%)	65

LIST OF FIGURES

Figure	Page
2.1 Schematic steps of <i>InVascular</i> : (1) anatomical extraction of morphology from patient's CTA; (2) quantification of $\Delta P (= P_p - P_d)$, using the morphology together with boundary conditions at inlet and outlets based on patient's DUS and related pathophysiological information; (3) parametric deterioration of the RAS characterized by volume reduction of lumen; (4) establishment of the correlation between ΔP and S to derive thresholds of S_m and S_s and new guidelines for a medical treatment.	8
2.2 Schematic steps of segmentation: (1) Thresholding based on the region of interest after importing CTA in Mimics; (2) Cropping the mask to remove unnecessary part; (3) 3-D calculation for generating 3D geometry; (4) Smoothing and wrapping the geometry in 3 Matic; (5) Modify the geometry in paraview for cutting the boundary parallel to XY or YZ plane; (6) Cutting the geometry smaller in paraview to reduce computational power and time	9
2.3 Schematic of cell-based space in VLBM distinguishing types of lattice cells: fluid cell ($\mathcal{P} = 0$), solid cells ($\mathcal{P} = 1$), and boundary cell ($0 < \mathcal{P} < 1$). The solid line represent an arbitrary boundary of the flow domain	11
2.4 Schematic of <i>InVascular</i> : (1) 3D anatomical extraction of vessel segment from CT/MRI image data; (2) CHD with the inputs of $\mathcal{P}(\mathbf{x})$ and inlet/outlet boundary conditions based on DUS image data as well as lumped parameter model; and (3) post-processing for medical guidelines and insights. The VLBM part is accelerated by GPU parallelism.	12
2.5 Illustration of inlet boundary condition from DUS image data for an irregular artery plane (a) A generic DUS image recording velocity magnitude wave $u_{in}(t)$ (b) An example of indexing to construct an irregular paraboloid velocity profile on inlet plane (c) Normalized velocity distribution on inlet plane varying from unit at the center to zero at boundary with side (left) and top (right) views.	15
2.6 WK3 model consists of one capacitor (C), modeling vessel compliance and two resistors (r and R) modeling proximal and distal resistance respectively	17
2.7 Coronary outlet LPN	18

Figure	Page
3.1 Integration of <i>InVascular</i> with velocity BC from DUS and pressure BC through the WK3 model at outlets in aortorenal system	29
3.2 Aortorenal system extracted from patient's CTA : Case I	30
3.3 Inlet velocity profile from DUS : Case I	30
3.4 Comparisons of pressure waves in Case I between noninvasive CHD (solid line) and invasive catheterization (dashed line)	32
3.5 Flowrate at different positions in aortorenal system for Case I	33
3.6 Pressure contours at systole for Case I	34
3.7 Velocity contours and streamlines for Case I	34
3.8 Aortorenal system extracted from patient's CTA : Case II	35
3.9 Inlet velocity profile from DUS : Case II	35
3.10 Comparisons of pressure waves in Case II between noninvasive CHD (solid line) and invasive catheterization (dashed line)	37
3.11 Flowrate at different slices for Case II	38
3.12 Pressure contour at systole for Case II	39
3.13 Velocity contours and streamline for Case II	39
3.14 Aortorenal system extracted from patient's CTA : Case III	40
3.15 Inlet velocity profile from DUS : Case III	40
3.16 Comparison of pressure waves in Case III between noninvasive CHD (solid line) and invasive catheterization (dashed line)	42
3.17 Flowrate at different positions of aortorenal system for Case III	43
3.18 Pressure contours at systole for Case III	44
3.19 Velocity contours and streamlines for Case III	44
3.20 Aortorenal system extracted from patient's CTA : Case IV	46
3.21 Inlet velocity profile from DUS : Case IV	47
3.22 Comparison of pressure waves in Case IV between noninvasive CHD (solid line) and invasive catheterization (dashed line)	48
3.23 Flowrate at different positions of aortorenal system for Case IV	49
3.24 Pressure contours at systole for Case IV	50
3.25 Velocity contours and streamlines for Case IV	50

Figure	Page
3.26 Aortorenal system extracted from patient's CTA : Case V	51
3.27 Inlet velocity profile from DUS : Case V	52
3.28 Comparison of pressure waves in Case V between noninvasive CHD (solid line) and invasive catheterization (dashed line)	53
3.29 Flowrate at different positions of the aortorenal system for Case V	54
3.30 Pressure contours at systole for Case V	55
3.31 Velocity contours and streamlines for Case V	55
3.32 Bland-Altman plot of 95% confidence for systolic blood pressure difference	57
3.33 Integration of <i>InVascular</i> with velocity BC from ECHO and pressure BC through the WK3 model at aorta and LPN at coronary artery	58
3.34 Coronary artery extracted from patient's CTA	59
3.35 Inlet velocity profile from ECHO.	60
3.36 Comparisons of pressure waves in coronary patient between noninvasive CHD (solid line) and invasive catheterization (dashed line)	61
3.37 Pressure contours at systole for coronary Case	62
4.1 Existing RAS extracted from CTA : Case IV LR artery	66
4.2 Parametric deterioration of the RAS characterized by volume reduction of lumen: Case IV LR artery	67
4.3 Severity of the existing RAS in Case IV with volumetric lumen reduction 10%.(a) Correlation of pick systolic trans-stenotic pressure gradient, (left, solid line) and FFR-CT (right, dashed line) (b) Flow ratio from aorta to LR ,Q(left, solid line) and RI (right, dashed line) vs. volumetric stenosis degree.	68
4.4 Existing RAS extracted from CTA : Case IV RR artery	69
4.5 Parametric deterioration of the RAS characterized by volume reduction of lumen: Case IV LR artery	70
4.6 Severity of the existing RAS with volumetric lumen reduction 15%.(a) Correlation of pick systolic TSPG, (left, solid line) and FFR-CT (right, dashed line) (b) Flow ratio from aorta to RR Q(left, solid line) RI (right, dashed line) vs. volumetric stenosis degree	71
4.7 Existing RAS extracted from CTA : Case V	72

Figure	Page
4.8 Parametric deterioration of the RAS characterized by volume reduction of lumen: Case V	73
4.9 Severity of the existing RAS in case V with volumetric lumen reduction 55%.(a) Correlation of pick systolic TSPG, (left, solid line) and FFR-CT (right, dashed line) (b) Flow ratio from aorta to LR Q(left, solid line) and RI (right, dashed line) vs. volumetric stenosis degree	74
4.10 Existing RAS extracted from CTA : Case VI	75
4.11 Parametric deterioration of the RAS characterized by volume reduction of lumen: Case VI	76
4.12 Severity of the existing RAS in case VI with volumetric lumen reduction 65% .(a) Correlation of pick systolic TSPG, (left, solid line) and FFR-CT (right, dashed line) (b) Flow ratio from aorta to LR Q(left, solid line) and resistive index (RI) (right, dashed line) vs. volumetric stenosis degree.	77
4.13 Existing CAS extracted from CTA	78
4.14 Parametric deterioration of the CAS characterized by volume reduction of lumen	79
4.15 Severity of the existing CAS with volumetric lumen reduction 13%.(a) Correlation of pick systolic TSPG, (left, solid line) and FFR-CT (right, dashed line) (b) Flow from aorta to LCX Q (left, solid line) and resistive index (RI) (right, dashed line) vs. volumetric stenosis degree	80

SYMBOLS

m	mass
v	velocity
S	stenosis
S_m	mild stenosis
S_s	severe stenosis
S_e	existing stenosis
P	pressure
Q	flowrate
t	time

ABBREVIATIONS

AS	Arterial stenosis
RAS	Renal Arterial Stenosis
CFD	Computational Fluid Dynamics
CTA	Computed tomography angiography
DUS	Doppler Ultrasound
FFR	fractional flow reserve
ICA	Invasive Coronary Angiography
MRI	Magnetic Resonance Imaging
CHD	Computational Hemodynamics
BC	Boundary Condition
WK3	3-element WindKessel model
LBM	Lattice Boltzmann method
CFD	Computational Fluid Dynamics
NS	Navier-stokes
GPU	Graphic processing unit
DSA	digital subtraction angiography
AA	Aortic Artery
RRA	Right Renal Artery
LRA	Left Renal Artery
TPSG	Trans-stenotic pressure gradient
CAS	Coronary Artery Stenosis
LBM	Lattice Boltzmann Method
VLBM	Volumetric Lattice Boltzmann Method
LPN	Lumped parameter network
ODE	Ordinary Differential Equation

LCX Left circumflex artery
LAD Left anterior descending artery
RCA Right coronary artery

ABSTRACT

Khan, Md Monsurul Islam M.S.M.E., Purdue University, August 2019. Image based computational hemodynamics for non-invasive and patient-specific assessment of arterial stenosis. Major Professor: Huidan (Whitney) Yu Professor, School of Mechanical Engineering.

While computed tomographic angiography (CTA) has emerged as a powerful non-invasive option that allows for direct visualization of arterial stenosis(AS), it cant assess the hemodynamic abnormality caused by an AS. Alternatively, trans-stenotic pressure gradient (TSPG) and fractional flow reserve (FFR) are well-validated hemodynamic indices to assess the ischemic severity of an AS. However, they have significant restriction in practice due to invasiveness and high cost. To fill the gap, a new computational modality, called *InVascular* has been developed for non-invasive quantification TSPG and/or FFR based on patient's CTA, aiming to quantify the hemodynamic abnormality of the stenosis and help to assess the therapeutic/surgical benefits of treatment for the patient. Such a new capability gives rise to a potential of computation aided diagnostics and therapeutics in a patient-specific environment for ASs, which is expected to contribute to precision planning for cardiovascular disease treatment. *InVascular* integrates a computational modeling of diseases arteries based on CTA and Doppler ultrasonography data, with cutting-edge Graphic Processing Unit (GPU) parallel-computing technology. Revolutionary fast computing speed enables noninvasive quantification of TSPG and/or FFR for an AS within a clinic permissible time frame. In this work, we focus on the implementation of inlet and outlet boundary condition (BC) based on physiological image date and and 3-element Windkessel model as well as lumped parameter network in volumetric lattice Boltzmann method. The application study in real human coronary and renal arterial system demonstrates the reliability of the in vivo pressure quantification through the

comparisons of pressure waves between noninvasive computational and invasive measurement. In addition, parametrization of worsening renal arterial stenosis (RAS) and coronary arterial stenosis (CAS) characterized by volumetric lumen reduction (S) enables establishing the correlation between TSPG/FFR and S, from which the ischemic severity of the AS (mild, moderate, or severe) can be identified. In this study, we quantify TSPG and/or FFR for five patient cases with visualized stenosis in coronary and renal arteries and compare the non-invasive computational results with invasive measurement through catheterization. The ischemic severity of each AS is predicted. The results of this study demonstrate the reliability and clinical applicability of *InVascular*.

1. INTRODUCTION

Normal arteries are flexible and has smooth inner wall that carries oxygen from the heart to the rest of the body. Atherosclerosis refers to hardening of arteries through deposition of plaque in the artery wall which are made of fats, cholesterol, fatty substances etc. High blood pressure, smoking and high cholesterol causes the damage of endothelium and starts the process of atherosclerosis. Low density lipoproteins (LDL) enters the wall of the artery through damaged epithelium and cause the white blood cell to digest the LDL. The cholesterol and cells become plaque over years. As the plaque develops , it limits the flow of blood to the body. Atherosclerosis does not show symptoms other than minor pain until it is severe enough to block an artery. It is a slow process and patient does not have symptoms until the artery get so narrowed that enough blood cant flow to the organ or tissues.

1.1 Stenosis

Stenosis means narrowing the arteries in the process of atherosclerosis over time. It can happen to different arteries through out the body i.e. renal, carotid, coronary, iliac arteries. Depending on the location it can cause stroke, heart attack, kidney damage and other vascular complications. For current research, we are looking into renal and coronary arterial stenosis.

1.1.1 Renal Arterial Stenosis

Renal artery delivers blood from the aorta to the kidney. There are two renal arteries that deliver to left and right kidney respectively. Due to RAS, renal artery get narrowed. So, it cant deliver enough to the kidney which can cause kidney damages.

RAS has been known to be one of the primary contributors to elevated renal resistance [1]. It may result in reduced juxtamedullary blood pressure [2] in the kidney causing renovascular hypertension that may induce direct kidney failure in the synergy with the harmful effects of diabetes if present [3].

While a RAS can be observed by radiological imaging modalities such as CTA or magnetic resonance imaging (MRI) as well as Doppler Ultrasonography (DUS), determination of the benefit from therapeutic/surgical intervention such as stenting or bypass to a patient remains challenges. The major hurdle is a lack of an appropriate means to assess the true contribution of RAS to renal physiology and pathology.

Although heavily used in clinical practice, the lumen reduction of a RAS has not been proven as an effective indicator to determine the necessity of a therapeutic/surgical intervention. The last two reported and largest randomized trials, AS-TRAL [4] and coral [5,6], of percutaneous renal artery intervention have generated much debate and controversy [7] as both have not been able to demonstrate clinical benefits from stenting therapy for patients with RAS. The reason might be the inappropriate stenosis severity criterion, which has 60% [8] of lumen diameter reduction.

Evidence has shown that hemodynamic severity is present where a significant pressure gradient across a RAS exists [9]. Due to the fact that a decrease in renal pressure distal to the stenosis is the fundamental trigger of renovascular hypertension, measurement of the TSPG would provide the most accurate means of assessing renal resistance. The TSPG, referred to as $\delta P = P_a - P_d$, is obtained through invasive measurement of the aortic pressure (P_a) through a guiding catheter and the poststenotic renal pressure (P_d) using a pressure wire advanced a least 4 cm distal to the renal stenosis under resting conditions. There is consensus that a resting peak systolic pressure gradient $> 20\text{mmHg}$ is significant in RAS, but it has not been clinically proven [10]. In case of coronary stenosis, FFR, defined as P_d/P_a , during invasive coronary angiography under adenosine-induced hyperemia has been established as a gold standard for the functional assessment of myocardial ischemia [11]. There have been attempts to determine the effectiveness of renal FFR for quantify-

ing functional significance of RAS but the FFR thresholds are not uniform [12–18]. The reason might be due to the hemodynamic difference between renal and coronary circulation[19]. It remains to be evaluated, whether TSPG or FFR, is an appropriate indicator to evaluate the functional hemodynamics in aortorenal vascular bed.

1.1.2 Coronary Arterial Stenosis

Coronary artery supplies blood to the heart. Due to gradual build up of plaque, coronary artery get narrowed and it can't deliver enough oxygen-rich blood to the heart. At the beginning of the stenosis, there may be no symptoms. As the plaque continue to grow, patients can feel pain in chest and shortness in breathe. When coronary stenosis become hemodynamically significant, it can cause ischemic heart disease.

Coronary heart disease is the major cause of death in general people, resulting in 7.6 millions death every year all over the world [19]. It is also leading cause of death in the United states. Coronary artery stenosis is one of the major causes of myocardial infraction (heart attack) [20].

Non-invasive imaging is considered as primary strategy to test patient suspected coronary artery stenosis [21]. But decision depending on only imaging causes frequent inaccurate selection of patient for invasive coronary angiography [22]. Even though noninvasive coronary CTA reveals the presence of coronary artery stenosis, it overestimates the relation between the coronary artery stenosis to myocardial ischemia [23]. FFR, defined as P_d/P_a , during invasive coronary angiography under adenosine-induced hyperemia has been established as a gold standard for the functional assessment of myocardial ischemia [11] : $FFR < 0.75$ (hemodynamically significant), $FFR > 0.8$ (hemodynamically insignificant), and $0.75 < FFR < 0.80$ (to be determined based on a patient clinical history). The largest randomized trials have shown threshold 0.8 of FFR to distinguish who will be benefited from revascularization of coronary and who will not [24–27]. But the question remains about the

generalization of the FFR threshold as different patient has different hemodynamic response and patient specific assessment is necessary to find the threshold FFR for individual patient.

1.2 Computational Hemodynamics

In recent years, a well-established engineering technique, named computational fluid dynamics (CFD), has been adopted to study biological flow [28,29]. Advances in medical imaging, computational power, and mathematical algorithms have provided new means to noninvasively compute 4-D (space+time) hemodynamics based on radiologically imaging such as CTA/MRI and DUS in the heart and major blood vessels for the patients with cardiovascular diseases, giving rise to a promising field of computation aided diagnostics and therapeutics in a patient-specific environment [11,30,31]. Based on CTA, MRI, and DUS image data, computational hemodynamics (CHD) enables noninvasive and patient specific computation of a full wealth dynamics information in *in vivo* blood flow in human vessel. Such data, including flow, pressure, vorticity, and wall-shear stress in the entire artery. These data are not readily available from the current standard clinical measurements, yet it can offer key insights into diseases progression and subsequent physiological response, thus aiding in clinical decision making for various cardiovascular diseases [32–36].

With patient-specific CHD, either the assessment of true hemodynamic abnormality or the prediction of potential therapeutic/surgical outcomes may aid in clinical decision making for various cardiovascular diseases. In principal, the image-based noninvasive computation may be more accurate and cost effective than invasive measurements such as FFR-CT [32], which has been a promising for the functional evaluation of coronary stenosis [33] with a growing body of evidence for diagnostic accuracy compared with invasive FFR.

A typical patient-specific CHD consists of three steps:

1. 3-D anatomical extraction for the morphology of the diseases vessel from CTA/MRI image data.
2. Quantification of 4-D hemodynamics employing physical parameters together with initial and boundary conditions based on DUS.
3. Post processing with parametric study, statistical analysis, and visualization to the key insights of the disease progression and subsequent physiological response.

Since only a segment of a vessel anatomy is included in CHD due to the limit of computational power and time, boundary conditions must be applied at inlets and outlets of the segmented vessel to accurately represent the vascular network outside of the local domain. The introduction of inlet BC is relatively simple, imposing either a parabolic flow profile using the poiseuille solution for flow in a circular pipe or using the analytical solution for womersley flow in a pipe based on a velocity wave from DUS measurement. The choice of outflow BC in CHD are diverse including zero pressure or zero traction conditions, resistance or impedance conditions, reduced-order models which can be open or closed loop, or reduced-order one dimensional wave propagation equations [37–39] to capture the interaction between the local 3D domain and the global circulation, the 3D Navier-Stokes (NS) solver must be coupled to a reduced order lumped parameter network model. The lumped parameter model [40–44] has been commonly used to construct such a network, in which a electrical circuit is adopted to model the distal vasculature with capacitor, modeling vessel compliance, and resistors , modeling patient specific flow downstream to the domain. Evidence have shown that lumped parameter can well reproduce physiological pressure wave [45, 46] in large vessel.

Lattice Boltzmann method (LBM) [47, 48] is a class of CFD method for simulating complex flows. Instead of directly solving a set of nonlinear partial differential equations, i.e. NS equations, LBM uses a discretized kinetic model on a regular lattice

to reproduce the dynamic of inexpressible fluid flow, in which the non-linearity is separated from the non-locality. Due to its particulate nature and local dynamics, the LBM has several advantages over NS-based CFD method, especially in dealing with complex boundaries [36, 49], incorporating microscopic interactions [28, 50] in multiphase flows, and implementing GPU parallelization of the algorithm [28, 49–51]. However, the LBM has not been extensively used for patient specific CHD do far and the majority attempts have imposed zero pressure boundary condition [52–55] at the outlets. The zero pressure boundary conditions, although easy to implement is well known to lead to unrealistic solution in CHD, in part because of its inability to capture physiological levels of pressure [31]. Few other studies have used fully developed boundary conditions [36, 56] at the outlet, which is also inappropriate for a pulsatile flow in arbitrary flow domains.

1.3 Objective

In this work, we develop physiological inlet/outlet BCs in LBM for patient-specific CHD in arterial system, based on CTA and DUS image data to quantify the in vivo 4-D hemodynamics. To validate the reliability of the computational results, the noninvasive computed pressure waves are compared with the corresponding invasive pressure measurements during digital subtraction angiography in clinic.

We also pioneer non-invasive and patient specific true severity of stenosis through the quantification of TSPG and FFR and its correlation to the parametric worsening of the stenosis characterized by lumen volume reduction. A developed image based CFD solver [36], which synergistically combines the newly developed volumetric lattice Boltzmann method (VLBM) for CFD with the GPU technology [36, 49], is adapted for image-based computational hemodynamics in human arterial system. Parameterization of stenosis worsening establishes the correlation between the TSPG (ΔP), FFR and the corresponding degree of stenosis (S), enabling the identification of the severity of the stenosis (mild, moderate, or severe).

2. METHODOLOGY

As depicted in Figure 2.1 the noninvasive and patient-specific *InVascular* assessment of the severity of stenosis consists of four steps. The first two steps, including (1) Segmentation of vessel morphology from CTA / MRI and (2) CFD quantification of TSPG and FFR utilizing the extracted vessel morphology and boundary conditions, are adapted from an in-house computational modeling technique [49]. The outstanding advantage of this in-house computational technique is its revolutionary fast computation speed realized by the cutting-edge GPU parallel computing technology thus *InVascular* is ideal for clinical oriented applications. Steps (3) and (4) in *InVascular* are specifically designed for the determination of true severity of an existing stenosis and the potential benefit of a stenting therapy through parametric study.

2.1 Segmentation of artery

Materialise's Interactive Medical Image Control System (Mimic) is a commercial software to process medical images and create 3-D geometry. It uses 2D cross sectional images like CTA, MRI to construct 3-D models which will be used for simulation. The medical images from CTA or MRI have grayscale information. A grayvalue is a number associated with a pixel of the image measuring the shade (white, grey and black). The association between material density and grayvalue to each pixel gives the flexibility to create any models separable in the scanned data.

Segmentation is a process to convert anatomical data from medical imaging data to 3-D models. We load stack of images in Mimic in the XY plane (axial images). Mimics then automatically create XZ (coronal) and YZ (sagittal) directional images.

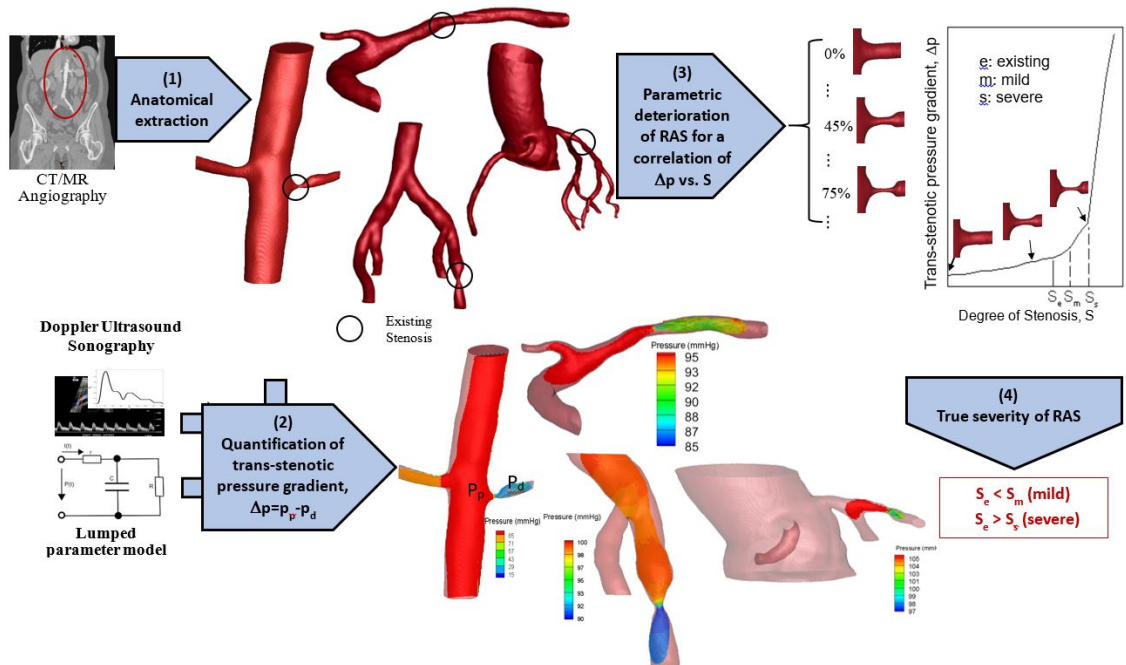


Figure 2.1. : Schematic steps of *InVascular*: (1) anatomical extraction of morphology from patient's CTA; (2) quantification of $\Delta P (= P_p - P_d)$, using the morphology together with boundary conditions at inlet and outlets based on patient's DUS and related pathophysiological information; (3) parametric deterioration of the RAS characterized by volume reduction of lumen; (4) establishment of the correlation between ΔP and S to derive thresholds of S_m and S_s and new guidelines for a medical treatment.

It gives us opportunity to modify the images from all three direction. Steps to segment region of interest we used Mimics for primary segmentation is showed in Figure 2.2.

Thresholding is used to classify all pixels within a certain range as the same colour named mask. By setting a particular lower threshold value, all the pixels higher than the set value will be under the same mask. First we need to find the region of interest from the CTA and fix a threshold value that highlights the particular region. Calculate 3D feature converts 2-D images to 3-D geometry. During the threshold,

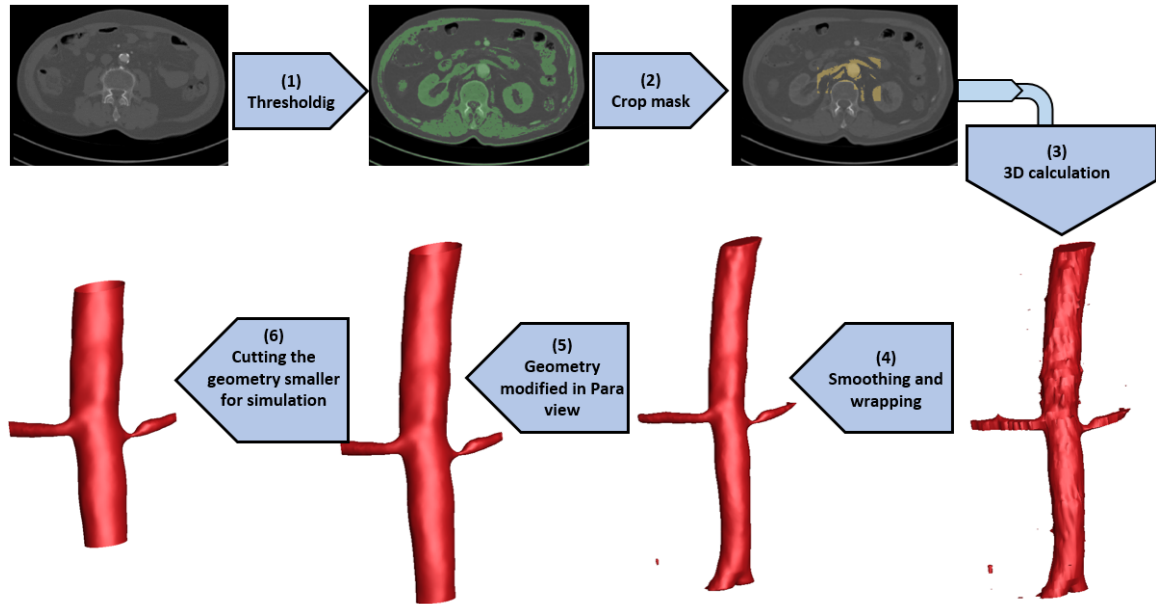


Figure 2.2. : Schematic steps of segmentation: (1) Thresholding based on the region of interest after importing CTA in Mimics; (2) Cropping the mask to remove unnecessary part; (3) 3-D calculation for generating 3D geometry; (4) Smoothing and wrapping the geometry in 3 Matic; (5) Modify the geometry in paraview for cutting the boundary parallel to XY or YZ plane; (6) Cutting the geometry smaller in paraview to reduce computational power and time

many unnecessary part with the region of interest will come through. Crop mask can manually change the boundaries of the mask and can also delete the unnecessary part. After finalizing the geometry, file is exported as STL format. STL file is the mesh file of triangulated surface. The file has three nodes at each triangle denoting the normal direction of the triangle.

After importing the STL file in 3-matic software, we find the surface is very rough compared to original geometry. We used local smoothing feature to make the geometry smoother. For parametric analysis we needed to modify the geometry and used push and pull features to modify the part in the stenosis. The corresponding

volume was also calculated to measure the percent of stenosis. The final geometry was imported to paraview to make the geometry smaller for simulation.

2.2 Lattice Boltzmann method for Computational Fluid Dynamics

As aforementioned, patient specific CHD includes image segmentation for anatomical extraction of vessel morphology and quantify *in vivo* velocity and pressure fields. We used GPU paralleled volumetric lattice Boltzmann method (VLBM) as a tool for CFD analysis to quantify 4-D hemodynamics. The VLBM was specifically developed for complex flows in arbitrary and willfully moving boundaries [36], in which the fluid particles are uniformly distributed in lattice cells, see Figure 2.3, as opposed to sitting at lattice nodes in conventional LBM. As schematized in Figure2.3, an arbitrary boundary (black line) separated a fluid domain (without dots) from a solid boundary structure (with dots). Three distinct cells are characterized through the occupation of solid volume $\Delta V_s(\mathbf{x})$ in the cell with total volume $\Delta V(\mathbf{x})$, defines as $\mathcal{P}(\mathbf{x}) \equiv \Delta V_s(\mathbf{x})/\Delta V(\mathbf{x})$. Thus three different cells, fluid cell ($\mathcal{P} = 0$), solid cell ($\mathcal{P} = 1$), and boundary cell ($0 < \mathcal{P} < 1$), can be distinguished through the value of \mathcal{P} . The detail formulation of LBM for CFD is referred to our group's previous publication [49]. The VLBM equation deals with the time evolution of the particle population, $n_i(\mathbf{x}, t)$, corresponding to the i th velocity for $i = 0, \dots, b$:

$$n_i(\mathbf{x} + \mathbf{e}_i \delta t, t + \delta t) = n_i(\mathbf{x}, t) - [n_i(\mathbf{x}, t) - n_i^{eq}(\mathbf{x}, t)]/\tau \quad (2.1)$$

where τ is the relaxation time of molecular motion relate to the kinematic viscosity and $n_i^{eq}(\mathbf{x}, t)$ is the equilibrium particle distribution function formulated as

$$n_i^{eq}(\mathbf{x}, t) = N\omega_i \left[1 + \frac{\mathbf{e}_i \cdot \mathbf{u}}{c_s^2} + \frac{(\mathbf{e}_i \cdot \mathbf{u})^2}{2c_s^4} - \frac{\mathbf{u} \cdot \mathbf{u}}{2c_s^2} \right] \quad (2.2)$$

with ω_i is an appropriate weight of the i -th velocity direction, c_s is the speed of sound, $N(\mathbf{x}, t) (= \sum n_i(\mathbf{x}, t))$ and $N(\mathbf{x}, t)\mathbf{u}(\mathbf{x}, t) (= \sum \mathbf{e}_i n_i(\mathbf{x}, t))$ are the total particle population and particle momentum in the cell respectively.

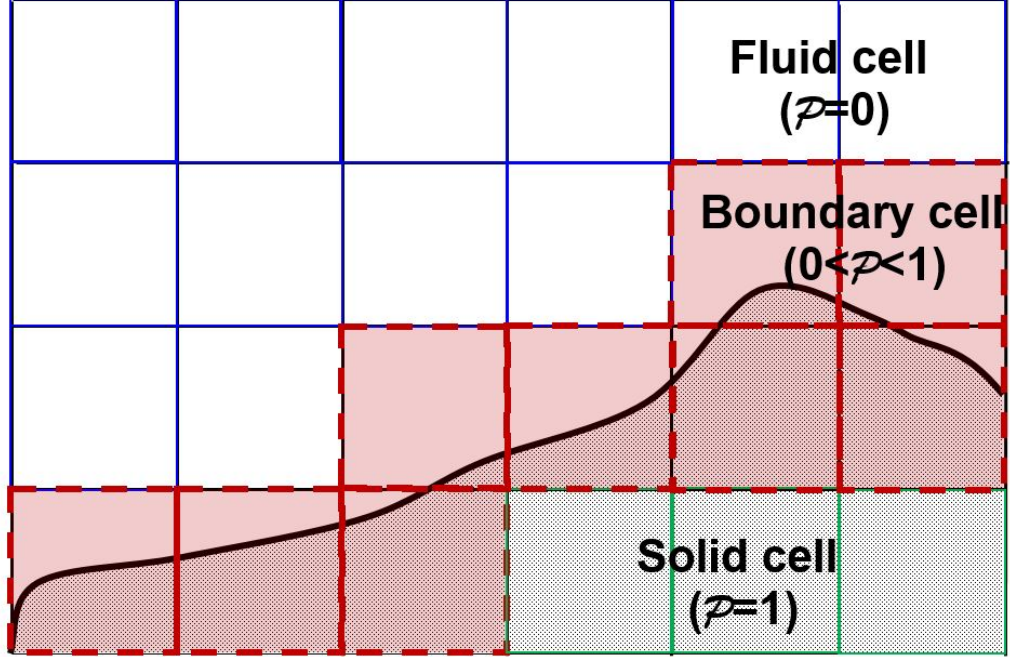


Figure 2.3. : Schematic of cell-based space in VLBM distinguishing types of lattice cells: fluid cell ($\mathcal{P} = 0$), solid cells ($\mathcal{P} = 1$), and boundary cell ($0 < \mathcal{P} < 1$). The solid line represent an arbitrary boundary of the flow domain

To depict the streaming part, we rewrite the right-hand side of equation(2.1) as

$$n'_i(\mathbf{x}, t) = n_i(\mathbf{x}, t) - [n_i(\mathbf{x}, t) - n_i^{eq}(\mathbf{x}, t)]/\tau \quad (2.3)$$

where $n'_i(\mathbf{x}, t)$ represents the "post-collision" particle population. Due to the existence of boundary cells, there would be only an appropriate volume fraction of fluid particles streaming to its neighboring cell. Particles in cell \mathbf{x} at time $t + \Delta t$ after a streaming operation are from two sources: (i) streaming from its upwind neighboring cells, $[1 - \mathcal{P}(\mathbf{x}, t)]n'_i(\mathbf{x} - \mathbf{e}_i\Delta t, t)$, and (ii) bounce-back from the downwind cells, $\mathcal{P}(\mathbf{x} + \mathbf{e}_{i*}\Delta t, t)n'_{i*}(\mathbf{x}, t)$, as shown below.

$$n''_i(\mathbf{x}, t + \Delta t) = [1 - \mathcal{P}(\mathbf{x}, t)]n'_i(\mathbf{x} - \mathbf{e}_i\Delta t, t) + \mathcal{P}(\mathbf{x} + \mathbf{e}_{i*}\Delta t, t)n'_{i*}(\mathbf{x}, t) \quad (2.4)$$

where i^* corresponds to the direction opposite to the i th direction $\mathbf{e}_{i^*} = -\mathbf{e}_i$. This modified streaming process ensures that particles are reflected to their appropriate places in the fluid domain but does not introduce any extra mass.

For current research, we focus on the integration of inlet/outlet BCs with VLBM. The entire computational platform is called *InVascular* [30, 57, 58]. As schematized in Figure 2.4 *InVascular* starts with feeding the $\mathcal{P}(\mathbf{x})$ of each cell to VLBM [36] (with D3Q19 lattice model), together with the inlet/outlet boundary conditions, for CHD.

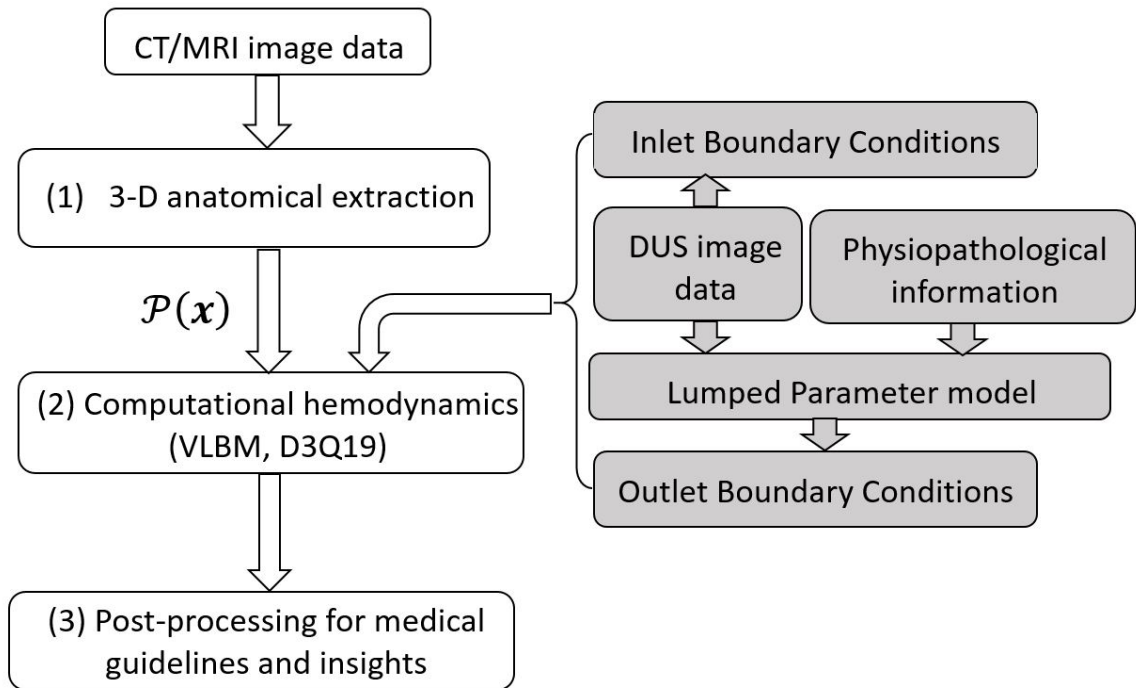


Figure 2.4. : Schematic of *InVascular*: (1) 3D anatomical extraction of vessel segment from CT/MRI image data; (2) CHD with the inputs of $\mathcal{P}(\mathbf{x})$ and inlet/outlet boundary conditions based on DUS image data as well as lumped parameter model; and (3) post-processing for medical guidelines and insights. The VLBM part is accelerated by GPU parallelism.

The resulting density, velocity, and pressure are obtained as $\rho(\mathbf{x}, t) = \sum n_i(\mathbf{x}, t)/[1 - \mathcal{P}(\mathbf{x}, t)]$ and $\mathbf{u}(\mathbf{x}, t) = \sum \mathbf{e}_i n_i(\mathbf{x}, t)/\sum n_i(\mathbf{x}, t)$. In LBM including node-based and cell-based representation, the relationship between density and pressure is

$$p(\mathbf{x}, t) - p_0 = c_s^2[\rho(\mathbf{x}, t) - \rho_0] \quad (2.5)$$

For inlet and outlet BCs, we employ the non-equilibrium extrapolation boundary condition as follows

$$n_i(\mathbf{x}_b, t) - n_i^{eq}(\mathbf{x}_b, t) = n_i(\mathbf{x}_f, t) - n_i^{eq}(\mathbf{x}_f, t) \quad (2.6)$$

for i th direction where \mathbf{x}_b and \mathbf{x}_f are the boundary cell and the fluid cell next to the boundary cell in the i -th direction. If velocity is known at the boundary $\mathbf{u}(\mathbf{x}_b, t)$ cell, the **velocity BC** is

$$n_i(\mathbf{x}_b, t) = n_i^{eq}(\rho(\mathbf{x}_f, t), \mathbf{u}(\mathbf{x}_b, t)) + n_i(\mathbf{x}_f, t) - n_i^{eq}(\mathbf{x}_f, t) \quad (2.7)$$

whereas if pressure $p(\mathbf{x}_b, t)$ is given, the **pressure BC** reads

$$n_i(\mathbf{x}_b, t) = n_i^{eq}(\rho(\mathbf{x}_b, t), \mathbf{u}(\mathbf{x}_f, t)) + n_i(\mathbf{x}_f, t) - n_i^{eq}(\mathbf{x}_f, t) \quad (2.8)$$

where $\rho(\mathbf{x}_b, t)$ is calculated from equation 2.5. The outstanding advantage of *InVascular* is its revolutionary fast computation speed realized by the cutting-edge GPU parallel computing technology thus *InVascular* is ideal for clinical oriented applications.

2.3 Boundary conditions

In patient specific CHD, the vessel wall is considered static and rigid. The boundary conditions include a non-slip condition on the vessel walls, pulsatile velocity condition based on DUS evaluation at inlet, and pressure conditions using lumped parameter model. Blood was considered as newtonian fluid having density 1.06gm/cc and dynamics viscosity 0.04 dynes/sq cm. We assumed the walls to be rigid in all cases.

2.3.1 Inlet boundary condition

DUS measures velocity wave, $u_{in}(t)$, has been commonly used as the inflow BC in patient specific CHD [31]. For a static wall, the typical way to introduce the pulsatile velocity to drive the blood flow into the segmented vessel is to construct a parabolic profile of Poiseuille flow, $u(r, t) = u_{in}(r, t)(1 - r^2/R^2)$, in which R is the vessel radius at the inlet and r is the distance to vessel center. Since real vessel lumens are usually not circular, we introduce the following algorithm, as illustrated in Figure 2.5, to construct an irregular paraboloid velocity profile varying the velocity magnitude from $u_{in}(t)$, digitized from patient's DUS shown in Figure 2.5(a), at the lumen center to zero on the wall. It should be noted that, for a blood flow, the inflow velocity is pulsatile thus the irregular velocity profiles need to be constructed at every time point and the time resolution should be fine enough determined through temporal convergence check. To refine the temporal resolution, an interpolation is needed.

We assume that the inlet plane is perpendicular to z direction (the direction of the blood stream) and located at $z = z_0$. On the inlet plane, each cell has known $\mathcal{P}(i, j, z_0)$ with $i = 1, \dots, N_x$ and $j = 1, \dots, N_y$. The algorithm to generate an irregular paraboloid velocity profile at time t includes the following steps, schematized in Figure 2.5(b).

1. Declare a matrix $N_x \times N_y$, *i.e.* ($i = 1, \dots, N_x, j = 1, \dots, N_y$) and initialize as $L_{ij} = 0$.
2. Loop i from 1 to N_x and j from 1 to N_y , if
 - (a) a cell's \mathcal{P} is neither 0 nor 1 indicating the cell is a boundary cell, index the cell as $L_{ij} = 1$ and define its velocity magnitude 0.
 - (b) a cell's \mathcal{P} is 0 (fluid cell) and $L_{ij} = 1$ value of its neighbouring cell is 1, index the cell as $L_{ij} = 2$

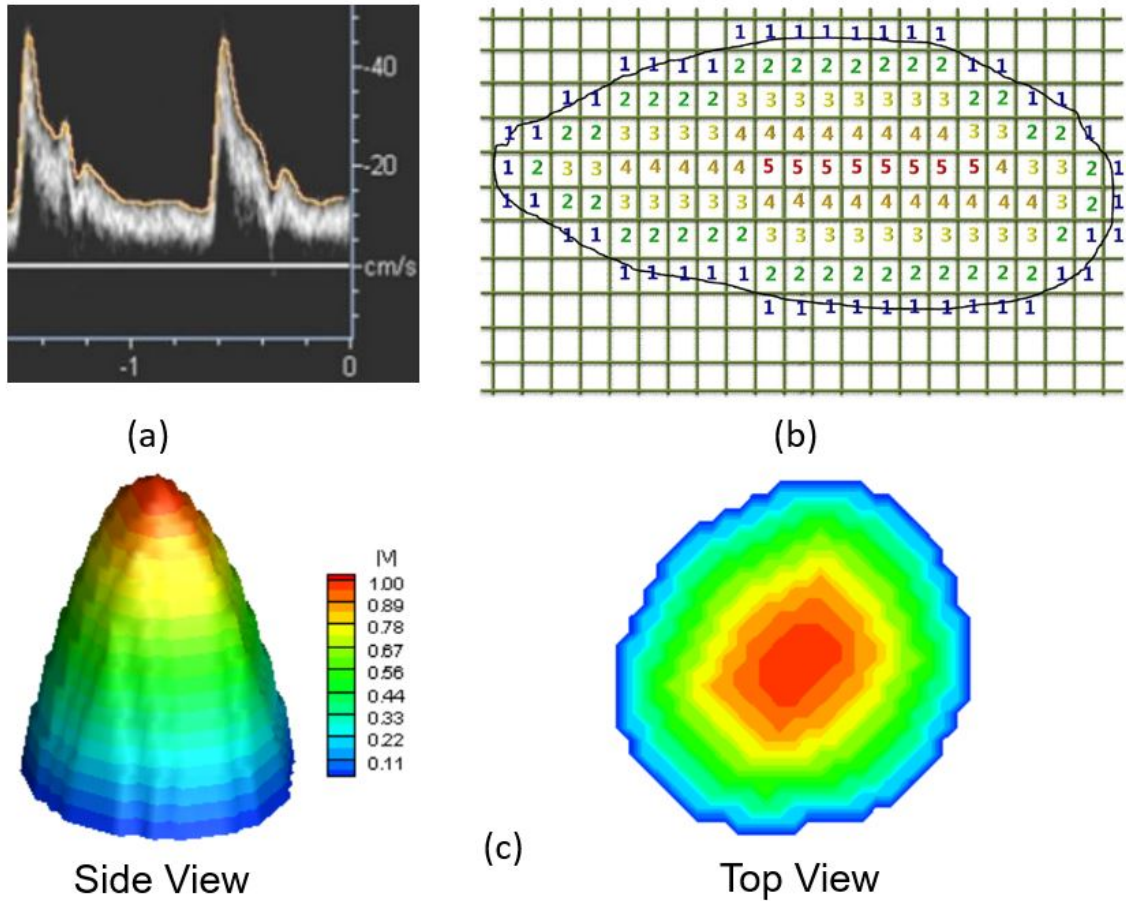


Figure 2.5. : Illustration of inlet boundary condition from DUS image data for an irregular artery plane (a) A generic DUS image recording velocity magnitude wave $u_{in}(t)$ (b) An example of indexing to construct an irregular paraboloid velocity profile on inlet plane (c) Normalized velocity distribution on inlet plane varying from unit at the center to zero at boundary with side (left) and top (right) views.

- (c) a cell's \mathcal{P} is 0 and $L_{ij} = 1$ value of its neighbouring cell is 2, index the cell as $L_{ij} = 3$, continue till all the fluid cells are indexed.
- (d) ... (continues)

(e) a cell's \mathcal{P} is 0 and $L_{ij} = 1$ value of its neighbouring cell is M-1, index the cell as $L_{ij} = M$, continue till all the fluid cells are indexed. Here M is the last index of the cell labeling.

3. Loop i from 1 to N_x and j from 1 to N_y if a cell's $\mathcal{P} = 0$ and $L_{ij} = n$ index with $n = 1, \dots, M$, define velocity magnitude for as $u_{in}^n(t) = n \times u_{in}(t)/M$.

Figure 2.5(c) shows two views of a parabolic velocity distribution on the irregular inlet plane at a time point. The inflow boundary condition is implemented through equation (3) in *InVascular*.

2.3.2 Outlet boundary condition, WK3 model

As shown in Figure 2.6, WK3 [39,40] is an analogy to an electrical circuit, which models the distal vasculature with one capacitor, C , modeling vessel compliance and two resistor, r and R , modeling proximal and distal resistance respectively, thus also known as RCR model. The flow (Q) and the mean pressure (P) over these boundaries are related by an ODE

$$\frac{dp}{dt} + \frac{1}{RC}p = r \frac{dQ}{dt} + \frac{1}{RC}(r + R)Q \quad (2.9)$$

where r and R represents the proximal and distal resistances, and C is the compliance of the distal vasculature. Specifically, r is used to absorb the incoming waves and reduce artificial wave reflections [41]. It has been well known that WK3 is the best compromising outlet BC model among other physiologically relevant 0-D outflow model to simulate the peripheral vasculature [59]. Equation 2.9 has an analytical solution

$$p(t) = e^{-t/RC} \int_0^t e^{s/RC} [r dQ(s)/ds + (r + \frac{RQ(s)}{RC})] ds + p_0 \quad (2.10)$$

where p_0 is the initial pressure at the outlet. It should be noted that the RCR circuit can be used for the large vessels such as the aorta and branch vessels going through to the hard and neck.

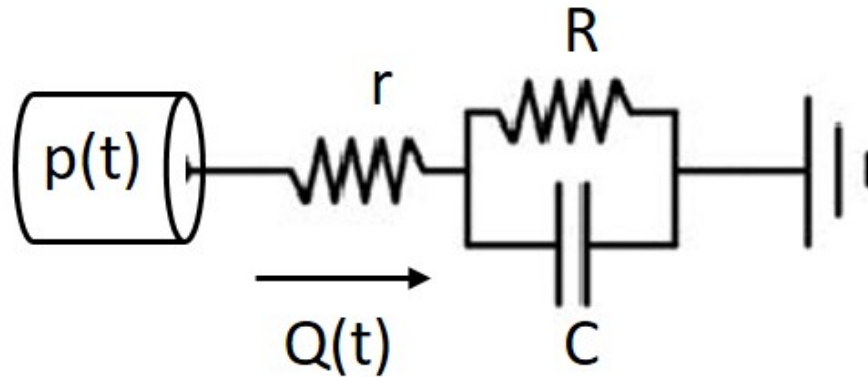


Figure 2.6. : WK3 model consists of one capacitor (C), modeling vessel compliance and two resistors (r and R) modeling proximal and distal resistance respectively

In patient-specific CHD, the three elements, r , C , R , specified at each outlet, must be tuned to obtain the physiological values for the mean flow rate (\bar{Q}_{out}) at the outlets and target systolic (p_{sys}) and diastolic (p_{dia}) pressure, with the mean arterial pressure, $\bar{p}_{in} = (p_{sys} + 2p_{dia})/3$, at the inlet based on patient's clinical data. For an aortorenal system, we used brachial pressure for a pressure target and MRI or DUS imaging data based on the availability for the flow target value (\bar{Q}_{out}). With the understanding that the capacitor and resistor have independent functionalities in WK3 circuit: a capacitor reflects the pulsatility of blood flow whereas a resistor determines flow rate [44].

2.3.3 Outlet boundary condition, lumped parameter network model for coronary outlet

Coronary artery delivers blood to the heart by surrounding them. As a result, contraction and relaxation of heart affects the flow of the coronary artery and flow pattern is different from systemic circulation. In systemic circulation, blood flow is maximum during systole and minimum during diastole. But for coronary artery, during systole, due to the contraction of heart, distal coronary resistance is increased

which impedes the flow. On the other hand, during diastole heart is relaxed and coronary resistance is decreased. So majority of the flow in coronary artery will be during diastole. To model the physiological coronary pressure and flow, a lumped parameter network (LPN) has been developed [60]. As shown in Figure 2.7, the LPN consists of resistor to model flow and pressure, capacitor to model vessel compliance or pulsatility and time varying pressure to model relaxation or contraction of the heart. In the Figure2.7, the LPN coronary model has seven electrical components [61]. They

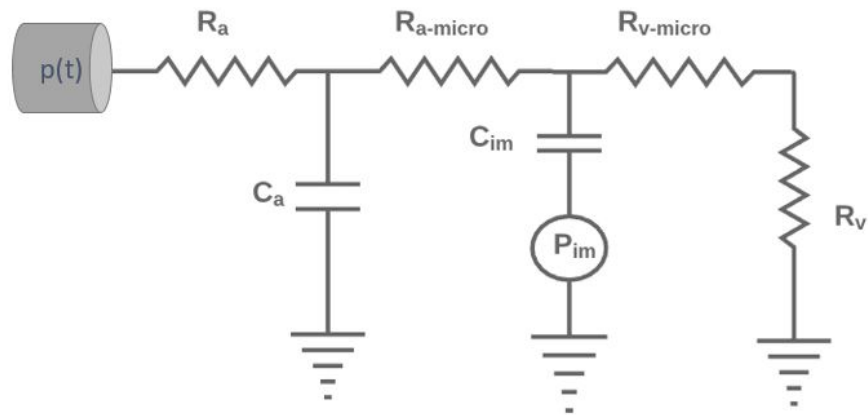


Figure 2.7. : Coronary outlet LPN

are

1. Arterial resistance, R_a
2. Microcirculation resistance, $R_{a-micro}$
3. Venous resistance, R_v
4. Venous microcirculation resistance, $R_{v-micro}$
5. Microcirculation compliance, C_a
6. Myocardial compliance, C_{im}
7. Intramyocardial pressure, P_{im}

For the LPN model, $P(t)$ and $Q(t)$ at coronary outlet is related by an ODE which has an analytical solution [61]

$$\begin{aligned}
 P(t) = & \left(RQ(t) + \int_0^t e^{\lambda_1(t-s)} Z_1 Q(s) ds \right) \\
 & - \int_0^t e^{\lambda_2(t-s)} Z_2 Q(s) ds + \left(Ae^{\lambda_1 t} - Be^{\lambda_2 t} \right) \\
 & + \left(\int_0^t e^{\lambda_1(t-s)} Y_1 P_{im}(s) ds - \int_0^t e^{\lambda_2(t-s)} Y_2 P_{im}(s) ds \right) \quad (2.11)
 \end{aligned}$$

where

$$\lambda_1 = \frac{-p_1 + \sqrt{p_1^2 - 4P_0P_2}}{2P_2}$$

$$\lambda_2 = \frac{-p_1 - \sqrt{p_1^2 - 4P_0P_2}}{2P_2}$$

$$A = \frac{-1}{\sqrt{p_1^2 - 4p_0p_2}} \left[(q_2\lambda_1 + q_1)Q(0) + q_2 \frac{dQ}{dt}(0) + b_1P_{im}(0) + p_2 \left(\lambda_2 P(0) - \frac{dp}{dt}(0) \right) \right]$$

$$B = \frac{-1}{\sqrt{p_1^2 - 4p_0p_2}} \left[(q_2\lambda_2 + q_1)Q(0) + q_2 \frac{dQ}{dt}(0) + b_1P_{im}(0) + p_2 \left(\lambda_1 P(0) - \frac{dp}{dt}(0) \right) \right]$$

$$R = \frac{q_2}{p_2}$$

$$Z_1 = \frac{q_2\lambda_1^2 + q_1\lambda_1 + q_0}{\sqrt{p_1^2 - 4p_0p_2}}$$

$$Z_2 = \frac{q_2\lambda_2^2 + q_1\lambda_1 + q_0}{\sqrt{p_1^2 - 4p_0p_2}}$$

$$Y_1 = \frac{b_1 * \lambda_1 + b_0}{\sqrt{p_1^2 - 4p_0p_2}}$$

$$Y_2 = \frac{b_1 * \lambda_2 + b_0}{\sqrt{p_1^2 - 4p_0p_2}}$$

$$p_0 = 1$$

$$p_1 = R_{a-micro}C_a + (R_v + R_{v-micro})(C_a + C_{im})$$

$$p_2 = C_a C_{im} R_{a-micro} (R_v + R_{v-micro})$$

$$q_0 = R_a + R_{a-micro} + R_v + R_{v-micro}$$

$$q_1 = R_a C_a (R_{a-micro} + R_v + R_{v-micro}) + C_{im} (R - a + R_{a-micro}) (R_v + R_{v-micro})$$

$$q_2 = C_a C_{im} R_a R_{a-micro} (R_v + R_{v-micro})$$

$$b_0 = 0$$

$$b_1 = C_i m (R_v + R_{v-micro})$$

During the selection of parameter for coronary outlet, it is assumed 4% of the cardiac output is assumed to go through coronary artery [60,62]. And flow ratio corresponds right and left coronary artery were chosen as 2:3 of the total coronary flow which was constructed by P_{im} ratio between left and right coronary artery [63].

Resistance calculation

First of all, vascular resistance of the system has been calculated by the ratio between mean arterial pressure and flowrate from DUS.

$$R_{total} = \frac{P_{mean}}{Q} \quad (2.12)$$

As it was assumed that coronary flow is 4% of the cardiac output, total coronary resistance will be 24 times [60] the vascular resistance.

$$R_{cor,tot} = 24 \times R_{total} \quad (2.13)$$

After calculating the total coronary resistance, we split the resistance for each coronary outlet according to the ratio of the area to 2.6 power, which is a generalization of the Murray's law [61]. So the total coronary resistance at each outlet is given by following expression where where A_j is area at each coronary outlets.

$$R_{cor,i} = \frac{\sum_j \sqrt{A_j}^{2.6}}{\sqrt{A_j}^{2.6}} R_{cor,tot} \quad (2.14)$$

To find R_a , $R_{a-micro}$ and R_v , we used the following ratios [64]

$$R_{a-i} = 0.32 * R_{cor,i}; R_{a,micro} = 0.52 * R_{cor,i}; R_v = 0.16 * R_{cor,i} \quad (2.15)$$

Capacitance calculation

The capacitor is tuned iteratively to find a stable simulation. $C_{cor,tot}$ is assumed to be $3.6 * 10^{-5} cm^5/dyne$ for left coronary artery and $2.5 * 10^{-5} cm^5/dyne$ for right coronary artery [64]. After $C_{cor,tot}$ is calculated, it is split among coronary outlets based on the ratio of the outlets.

$$C_{cor,i} = \frac{A_i}{\sum_j A_j} C_{cor,tot} \quad (2.16)$$

Once capacitance for each outlet is specified, C_a and C_{im} is calculated by following equations [64]

$$C_{a,i} = 0.11 * C_{cor,i}; C_{im,i} = 0.89 * C_{cor,i} \quad (2.17)$$

Intramyocardial Pressure

The pressure source P_{im} represents intramyocardial pressure that is responsible for the opposite phase behaviour of the coronary artery with systemic circulation. Modeling of heart can provide P_{im} to accommodate the change in intramyocardial pressure but for simplicity we used a pulsatile wave as P_{im} provided in one of the literature [61]. The pressure was varied iteratively to get a stable solution.

2.4 Integration of outlet boundary conditions

WK3 model integration

The integration of WK3 model with solver at an outlet plane is described as follows:

1. Determine the resistance at each outlet
 - (a) Assume the total system compliance $C_t = 0.001cm^5/dynes$.
 - (b) Calculate the total resistance $R_t(= r + R) = \bar{P}_{in}/\bar{Q}_{out}$.
 - (c) Determine r and R based on previous studies. the proximal resistance r weights 28% [5, 65] and 5.6% [66] out of the total resistance in renal artery. For abdominal aorta the proximal and distal resistance are found by $r = 0.91 * R_{tot}$, $R = 0.09 * R_{tot}$.

2. Tune the resistance r and R based on MRI or DUS data at each outlet.
 - (a) Integrate the WK3, equation 2.10, with 3D VLBM and run CHD. In one pulsation, r , R and C remains the same but $Q(t)$ at each outlet is obtained from CHD.
 - (b) Once a CHD simulation is done, check if the mean flow rate at each outlet matches with that calculated from MRI or DUS imaging data. If yes, r , R are determined; If not, adjust R_t and repeat 1)b and c and 2)a and b.

3. Determine compliance at each outlet
 - (a) Distribute C_t to each outlet proportional to the corresponding mean flow rate.
 - (b) Check if the pressure difference between $P_{(sys)}$ and $P_{(dia)}$ from CHD matches with the Arm pressure measurement. if not, adjust C_t in 1)a and repeat 1) and 2).

The outlet BC at each outlet is introduced in VLBM through equation 2.8 after the pressure is obtained from equation 2.10 at each time step.

LPN model integration

The integration of LPN model with solver at an outlet plane is described as follows:

1. Determine the total resistance, R_{tot} at Aorta Outlet
 - (a) Assume the total system compliance $C_t = 0.001cm^5/dynes$
 - (b) Calculate the total resistance from equation 2.12
 - (c) Determine r and R based on previous studies. The proximal and distal Resistance are found by [64] $r = 0.91 * R_{tot}$, $R = 0.09 * R_{tot}$.
2. Tune the resistance r and R based on DUS data at the aorta
 - (a) Integrate the WK3, equation 2.10, with 3D VLBM and run CHD. In one pulsation, r , R and C remains the same but $Q(t)$ at aorta outlet is obtained from CHD.
 - (b) Once a CHD simulation is done, check if the mean flow rate at aorta outlet matches with that calculated from DUS imaging data. If yes, r , R are determined; If not, adjust R_t and repeat 1)b and c and 2)a and b.
3. Determine C_t compliance for the aorta

- (a) Check if the pressure difference between $P_{(sys)}$ and $P_{(dia)}$ from CHD matches with the arm pressure measurement. If not, adjust C_t in 1)a and repeat 1) and 2).
4. Determine Resistance for the coronary outlet
- (a) $R_{cor,tot}$ is calculated from equation 2.13 and total resistance for each coronary artery is calculated using equation 2.14 . The components of Resistance for each outlet is calculated using equation 2.15.
 - (b) Assume $C_{cor,tot}$ to be $3.6 * 10^{-5} cm^5 / dyne$ for left coronary artery and $2.5 * 10^{-5} cm^5 / dyne$ for right coronary artery. Components of capacitance for each outlet is calculated by equation 2.17.
 - (c) Assume P_{im} for left coronary artery as $2 * P_{im}$ and $0.5 * P_{im}$ for right coronary artery [64].
5. Tune the P_{im} based on the stability
- (a) Integrate the LPN, equation 2.11, with 3D VLBM, see Figure 2.4 and run CHD.
 - (b) Once a CHD simulation is done, check if the flow and pressure is stable or not.
 - (c) If yes, P_{im} is determined. If not, change the P_{im} and repeat 5)a until a stable solution is achieved.

The outlet BC at aorta is introduced in VLBM through equation 2.8 after pressure is obtained from equation 2.10 at each time point. At the same time coronary BC is employed through equation 2.8 after pressure is obtained from equation 2.11 at each time step.

2.5 Parametrization for stenosis severity

From DUS and CTA, it is straight forward to diagnose the stenosis in human artery. But the main challenge is to determine the severity of stenosis. *InVascular* is specifically designed for the determination of the true severity of existing stenosis and the potential benefit of stenting therapy. Instead of the lumen diameter reduction, although heavily used in the current clinic practice, lumen volume reduction is employed to characterize the degree of stenosis (S). Parametric analysis though volume reduction at the stenosis location was done from 0% to 96% with an increment of 5%. For each incremental degree of stenosis, S, Step 2 in Figure 2.1 is executed to obtain the corresponding TSPG and FFR. A relation between TSPG and S is then established. From the TSPG-S diagram, one can find out two thresholds of S, S_m (mild) and S_s (severe), where the slopes of the curve change rapidly. Figure 2.1 Step 4 determine the severity of S_e (existing stenosis) based on its location on the TSPG-S. The clinical guidelines might be derived as follows: If $S_e < S_m$, the existing stenosis is mild and no immediate treatment is needed; If $S_e > S_s$, the existing stenosis is severe and a stenting therapy might be a reasonable option with further clinical clarification. If $S_m < S_e < S_s$, the existing stenosis is moderate and medical management might be the best option.

2.6 Patient cases

Renal artery cases

As listed in Table 2.1, six patient cases are studied. All the patients are male. Totally 18 aortic and renal arteries are studied. The imaging data including computed tomography angiography (CTA) and doppler ultrasound (DUS) were obtained from the electronic medical libraries in Methodist Hospital of Indianapolis, Indiana, USA (Case I and case II) and Hangzhou First People's Hospital, Hangzhou, China (case III-VI), respectively. The CTA resolution is approximately $0.75^2 \times 2.5mm^3$ (Cases I

and II) and $0.65^2 \times 0.6mm^3$ (Cases III and VI). case I-V have the invasive pressure measurement in the aorta (AA), left renal (LR), and right renal (RR) arteries during DSA (digital subtraction angiography). The invasively measured pressure profiles are used to validate the *InVascular* computed pressure in the aortorenal system. The pulsatile pressure in AA (P_A) was measured directly with a catheter placed in the aorta and a pressure transducer. Pressure waves in RR (P_{RR}) and LR (P_{LR}) arteries were measured with a pressure wire. The measurements were repeated after a renal artery vasodialator infusion of 25mg Papaverine. The complete pressure waveform and electrocardiogram was recorded over three cardiac cycles for each location. Case

Table 2.1. : Study Cases for Renal Artery

Cases	Age	RAS	Stenting Therapy	Invasive pressure measurement
I	74	No	No	Yes
II	75	No	No	Yes
III	83	Minor	No	Yes
IV	64	Minor	No	Yes
V	87	Severe	yes	Yes
VI	77	Severe	yes	No

I and II, with no renal artery stenosis (RAS), were collected only for validating the computed pressure. The pressure measurements for these two cases were made when the patient underwent renal artery stent placement for fenestrated aortic aneurysm repairs. In Cases III-VI, RAS ere observed, followed by DSA assessment to determine if a stenting is needed. Among the four cases, Cases V and VI underwent a stenting procedure. In case of V, the invasive pressure measurement was done before and after stenting.

Coronary artery cases

For coronary artery, one patient case has been studied. The imaging data including CTA and Echocardiography (ECHO) were obtained from Hangzhou First People's Hospital, Hangzhou, China. The CTA resolution is approximately $0.33^2 \times 1.0\text{mm}^3$. We have the invasive pressure measurement of Aorta (AA), proximal(P_d) and (P_d) distal of stenosis and corresponding fractional flow reserve (FFR) during digital subtraction angiography (DSA). The invasively measured pressure profile and FFR are used to validate the *InVascular* computed pressure in the coronary arterial system.

3. APPLICATION STUDY : PATIENT SPECIFIC COMPUTATIONAL HEMODYNAMICS IN ARTERIAL SYSTEMS

We first demonstrate the reliability of *InVascular* for the quantification of 4-D pressure field in arterial systems. The comparison of pressure profile in one cardiac cycle is between noninvasive computation and invasive measurement. The pressure gradient can be calculated via either systolic pressure (P_{sys}) or mean arterial pressure (MAP) defined as one-third peak systolic pressure plus two-thirds end of diastolic pressure (P_{dia}). Besides the pressure field, *InVascular* simultaneously quantifies the 4-D velocity field thus vorticity and shear stress fields can be calculated. Velocity field with magnitude contours and streamlines and vorticity contours at systole (heart contraction, flow acceleration), diastole (heart relaxation, flow deceleration), and the end of diastole in one cardiac cycle have been shown.

3.1 Aortorenal arterial system

Figure 3.1 depicts the computation platform to quantify 4-D flow through *InVascular* in aortorenal system. Parabolic velocity profile from DUS was used as inlet and WK3 model BC was used at each outlet.

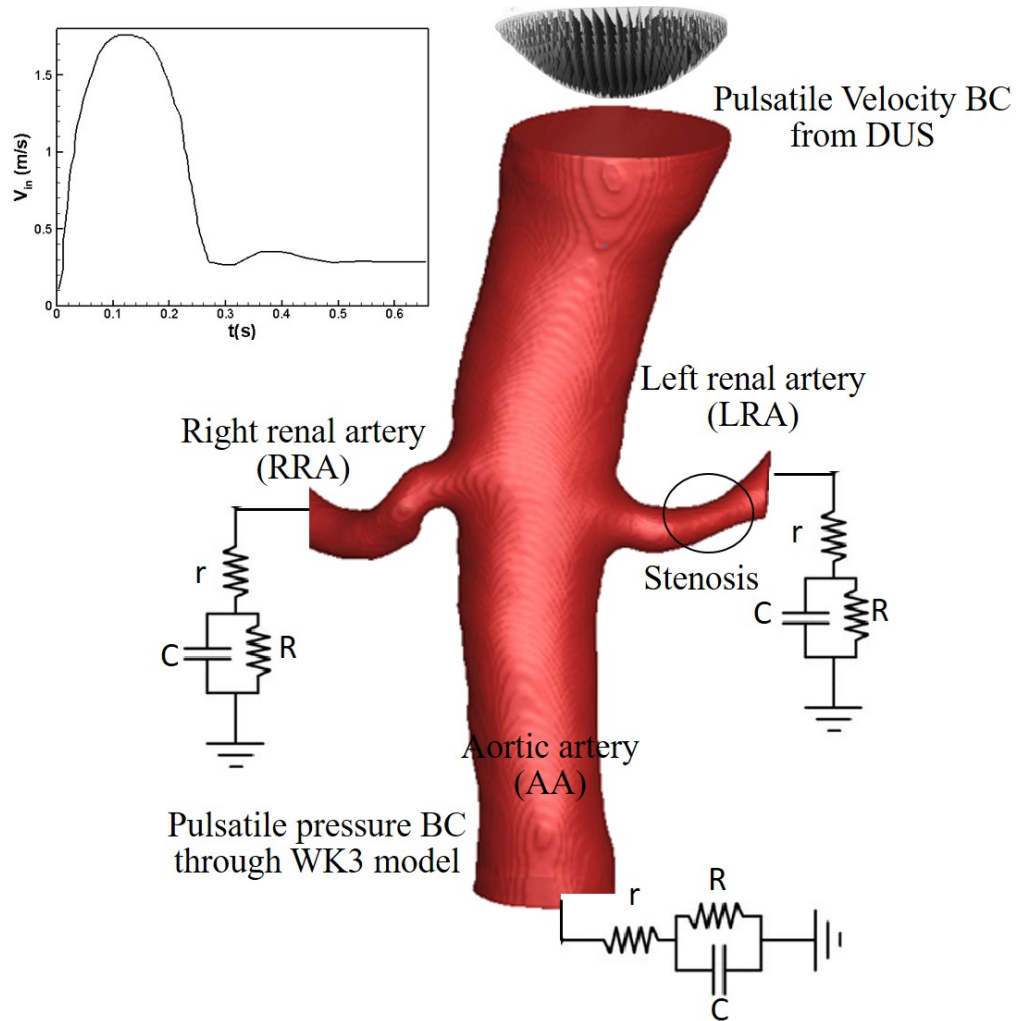


Figure 3.1. : Integration of *InVascular* with velocity BC from DUS and pressure BC through the WK3 model at outlets in aortorenal system

3.1.1 Case I

The segmented geometry of patient Case I from CTA using Mimic is shown in Figure 3.2. The r , R and C values used at each outlet tuned from DUS are shown in Table 3.1. Figure 3.4 shows the comparison of the cyclic pressure waves in (a) abdominal aorta (AA), (b) right renal artery (RRA), and (c) left renal artery (LRA) between noninvasive computation (solid lines) and invasive measurement (dashed lines). The

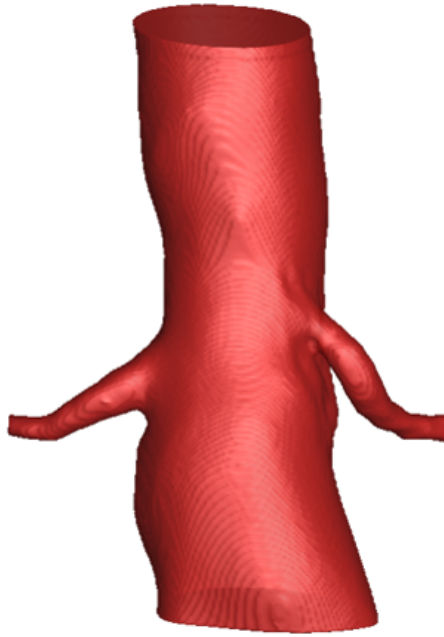


Figure 3.2. : Aortorenal system extracted from patient's CTA : Case I

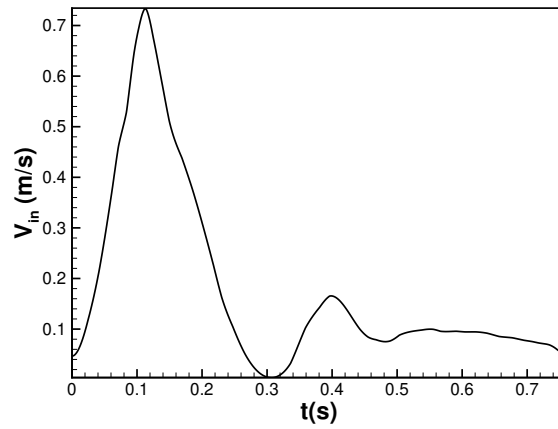


Figure 3.3. : Inlet velocity profile from DUS : Case I

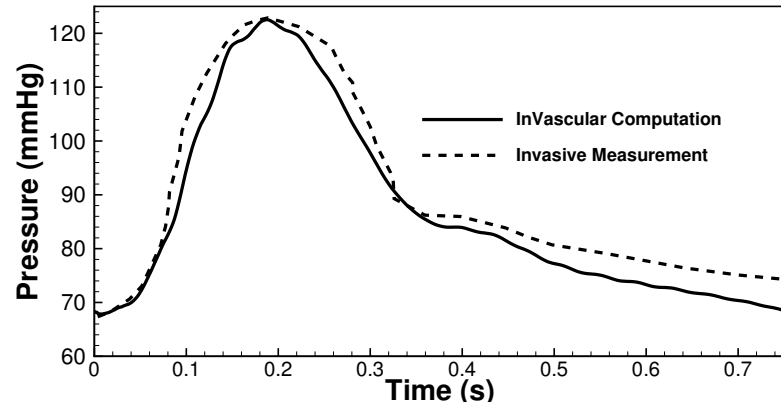
Table 3.1. : Values of resistances and compliances parameters in WK3 model at corresponding outlet of Case I

Outlets	r (dynes.s/cm^5)	R (dynes.s/cm^5)	$10^{-5}C$ (cm^5/dynes)
AA	88.0	2773.1	1.8
LRA	2982.4	7666.03	0.36
RRA	5972.8	15358.7	0.32

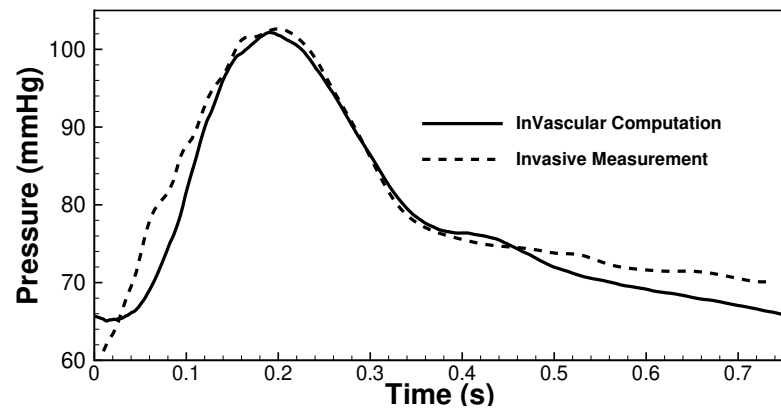
computed pressure waves agree very well with the medical measured images. For case I, we find some minor deviation in the beginning of diastolic region with the invasive measurement. The TSPG was calculated via MAP and systolic pressure. The comparison between noninvasive computation and invasive measurement is shown in Table 3.2. We see that *InVascular* can capture the systolic pressure quite accurately. But as there was some deviation in the diastolic region, we find some difference when compared the MAP.

InVascular quantified the 4-D pressure and velocity field in the aortorenal system. Figure 3.6 shows the 4-D pressure contour in LRA, RRA and cross section of the aortorenal system.

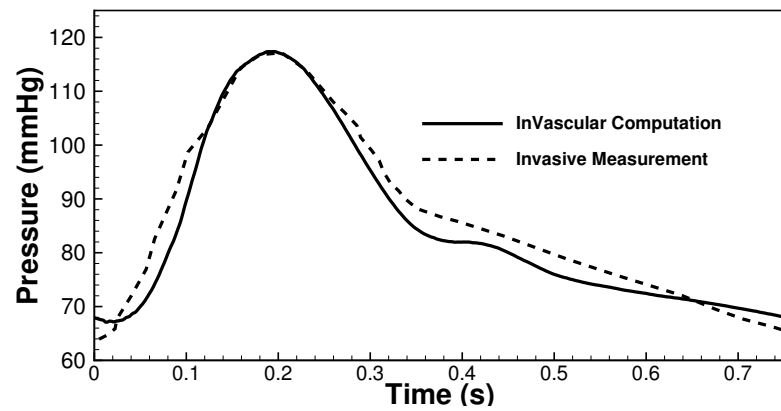
Velocity field with magnitude contours and streamline respectively at (a) $t=0.17$ (s), b= 0.29 (s) and (c)= .75 (s) in one cardiac cycle corresponding to systole (heart contraction, flow acceleration), diastole (heart relaxation, flow deceleration), and the end of diastole respectively are shown in Figure 3.7. Flow in AA is stronger in systole (a) than at diastole (b) but remains intensive in LRA and RRA at both time points and is better organized at systole than at diastole. Whereas at the end of diastole, the flow is weak, but chaotic.



(a) AA



(b) LR

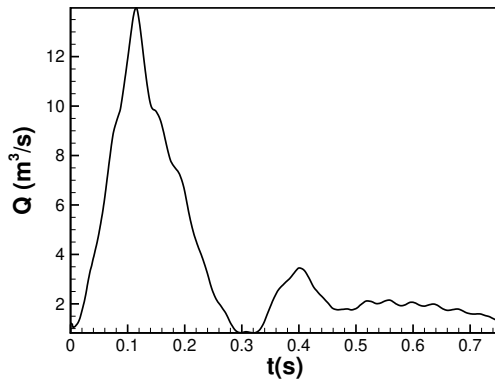


(c) RR

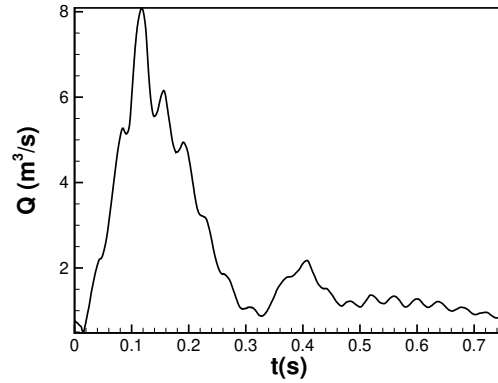
Figure 3.4. : Comparisons of pressure waves in Case I between noninvasive CHD (solid line) and invasive catheterization (dashed line)

Table 3.2. : Comparison of TSPG in LRA and RRA based on MAP or p_{sys} in Case I

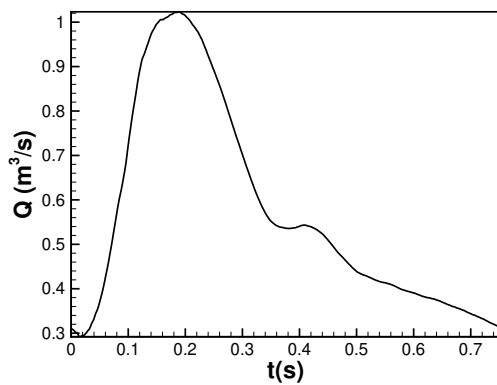
TSPG (mmHg)	MAP		P_{sys}	
	Noninvasive computation	Invasive measurement	Noninvasive computation	Invasive measurement
$p_{AA} - p_{LRA}$	2.0	2.6	4.1	4.0
$p_{AA} - p_{RRA}$	2.0	2.0	4.0	4.0



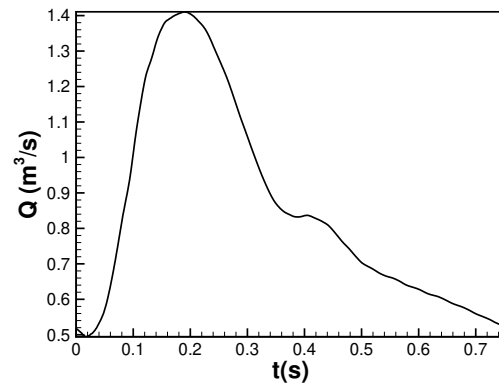
(a) AA near inlet



(b) AA near outlet



(c) RR



(d) LR

Figure 3.5. : Flowrate at different positions in aortorenal system for Case I

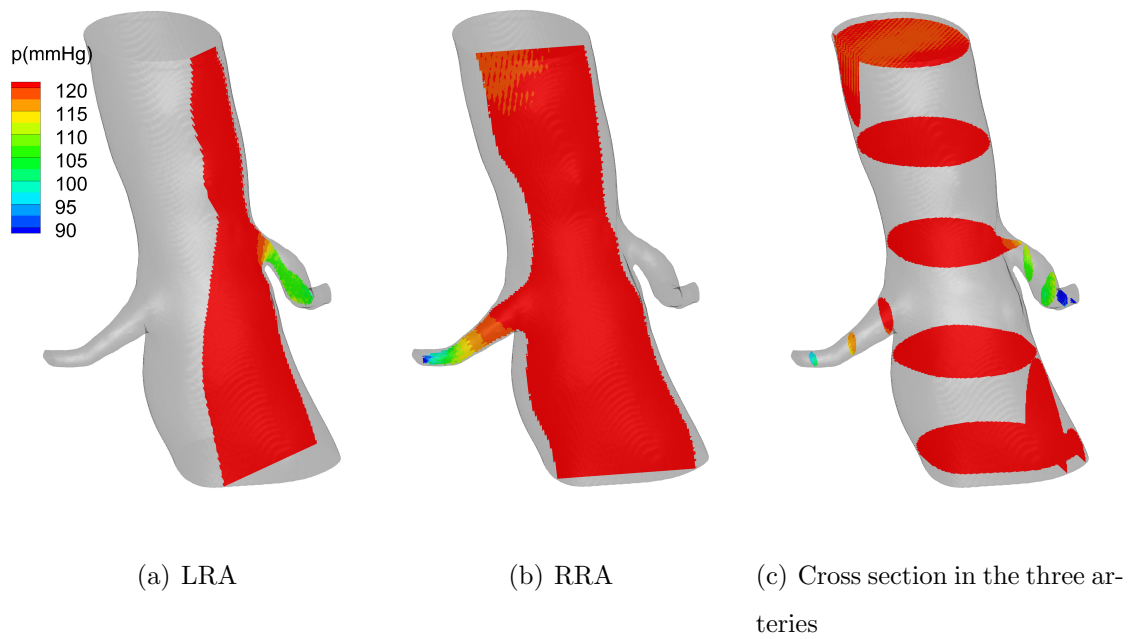


Figure 3.6. : Pressure contours at systole for Case I

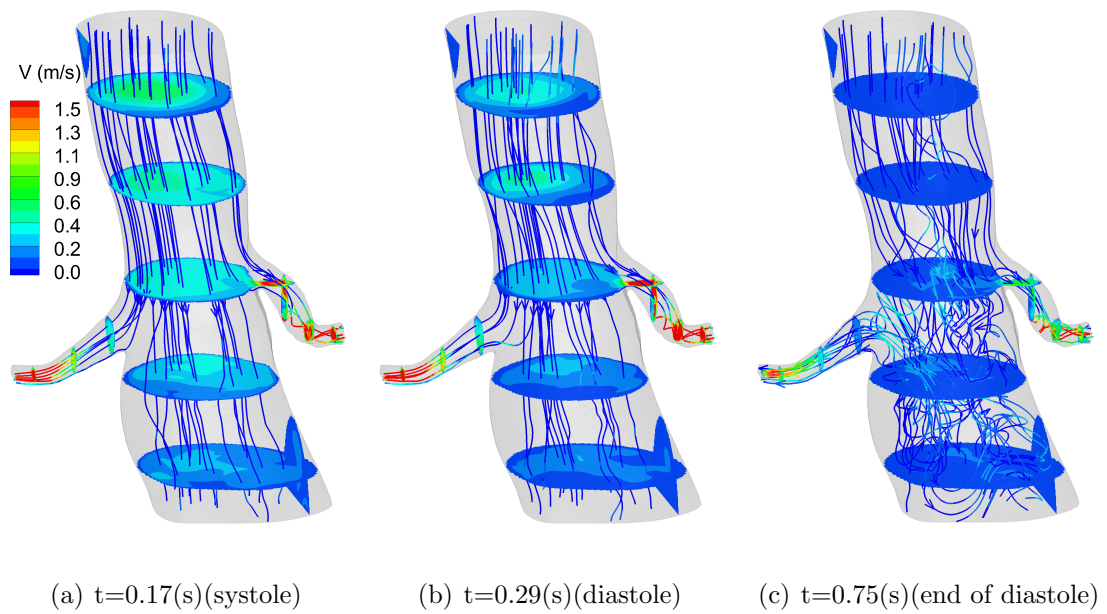


Figure 3.7. : Velocity contours and streamlines for Case I

3.1.2 Case II

The segmented geometry of patient case II from CTA using Mimic is shown in Figure 3.8. The r , R and c values used at each outlet tuned from DUS are shown in Table 3.3.

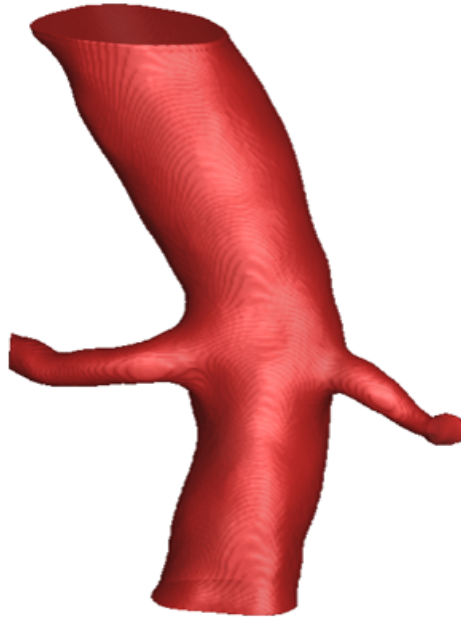


Figure 3.8. : Aortorenal system extracted from patient's CTA : Case II

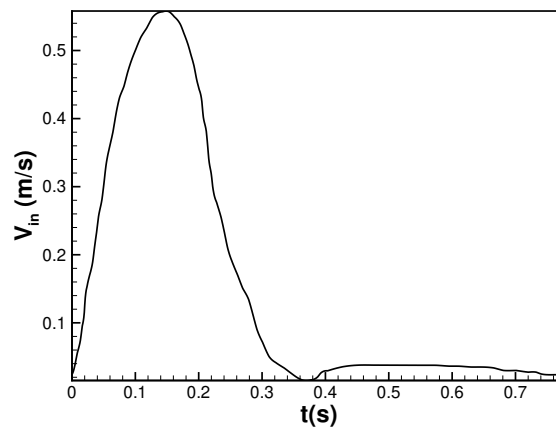


Figure 3.9. : Inlet velocity profile from DUS : Case II

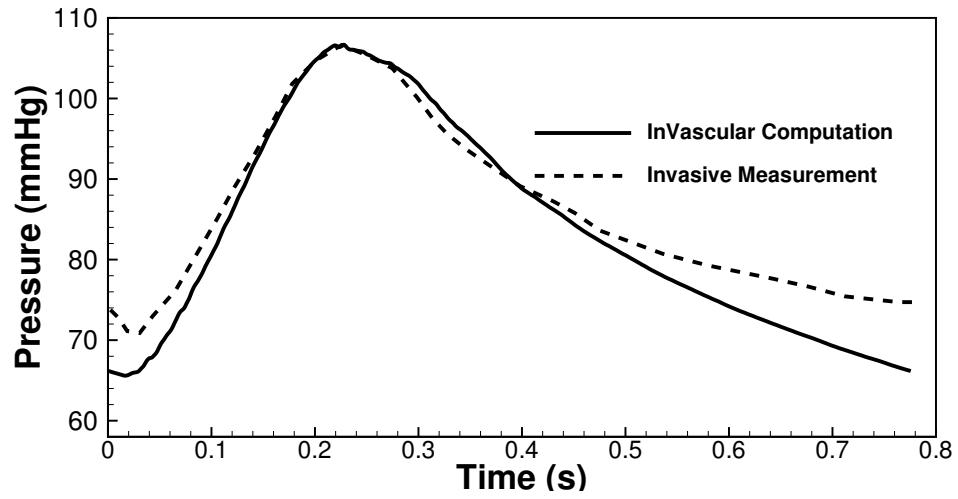
Table 3.3. : Values of resistances and compliances parameters in WK3 model at corresponding outlet of Case II

Outlets	r (dynes.s/cm^5)	R (dynes.s/cm^5)	$10^{-5}C$ (cm^5/dynes)
AA	97.32	3053.08	9.44
LRA	1399.88	3597.03	0.57
RRA	6122.16	15742.70	0.35

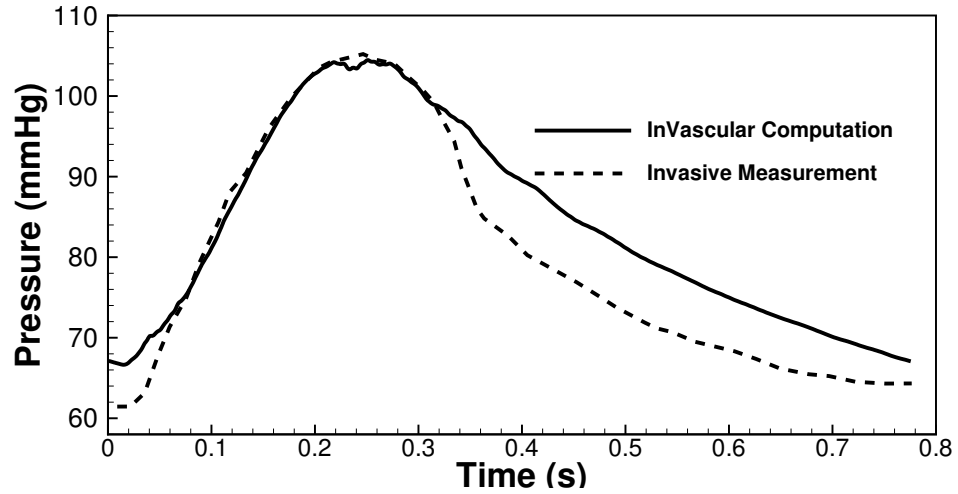
Table 3.4. : Comparison of TSPG in LRA and RRA based on MAP or p_{sys} in Case II

TSPG (mmHg)	MAP		P_{sys}	
	Noninvasive computation	Invasive measurement	Noninvasive computation	Invasive measurement
$p_{AA} - p_{RRA}$	2.0	1.9	10	6.0

Figure 3.10 shows the comparison of the cyclic pressure waves in (a) AA, (b) RRA between noninvasive computation (solid lines) and invasive measurement (dashed lines). The deviation is much higher than case I in the diastolic region. Figure 3.12 shows the 4-D pressure in LRA, RRA and cross section of the aortorenal system. Velocity field with magnitude contours and streamline respectively at (a) $t= 0.19(\text{s})$, $b= 0.32(\text{s})$ and $(c)= .67(\text{s})$ in one cardiac cycle corresponding to systole (heart contraction, flow acceleration), diastole (heart relaxation, flow deceleration), and the end of diastole respectively are shown in 3.13 . The flow rate at each time point, calculated at renal artery and abdominal aorta near inlet and outlet are shown in Figure 3.11.

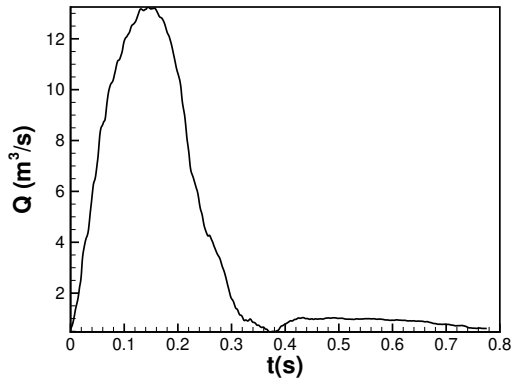


(a) AA

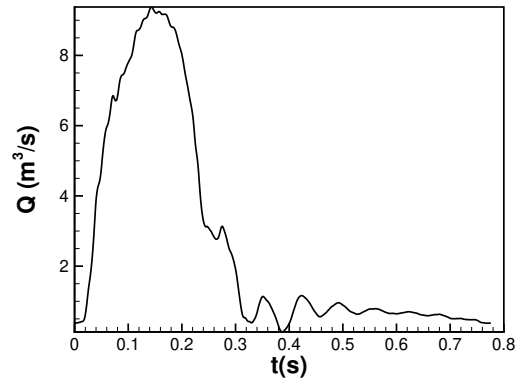


(b) RR

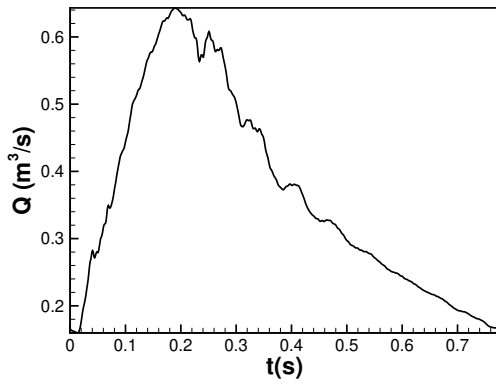
Figure 3.10. : Comparisons of pressure waves in Case II between noninvasive CHD (solid line) and invasive catheterization (dashed line)



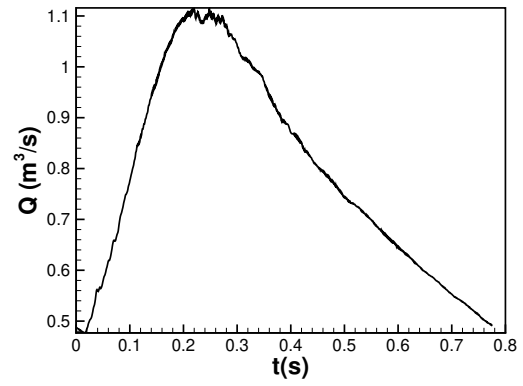
(a) AA near inlet



(b) AA near outlet



(c) RR



(d) LR

Figure 3.11. : Flowrate at different slices for Case II

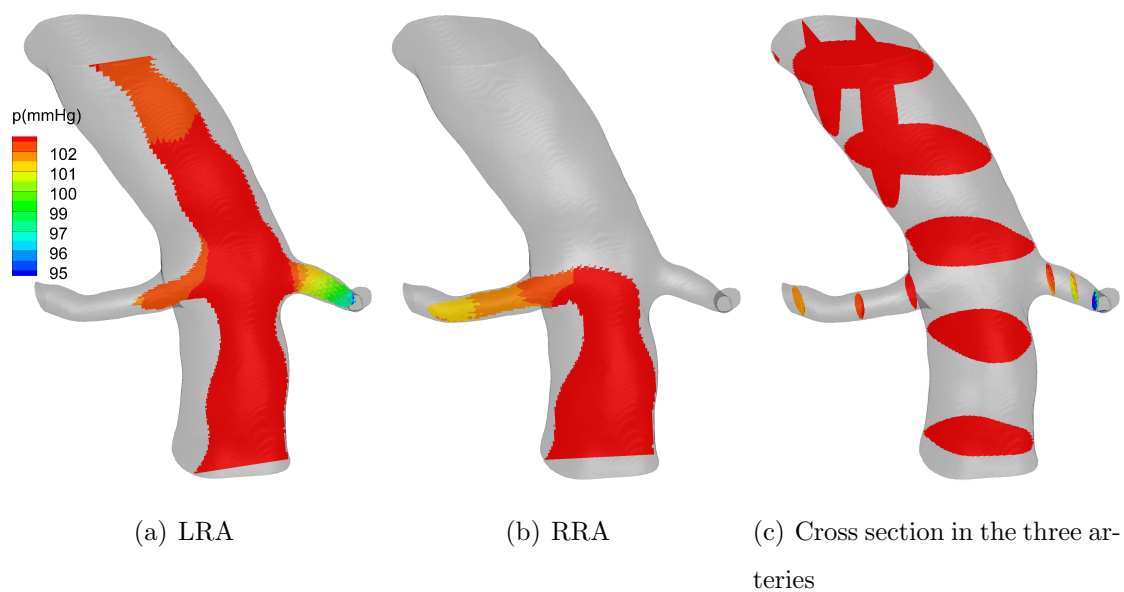


Figure 3.12. : Pressure contour at systole for Case II

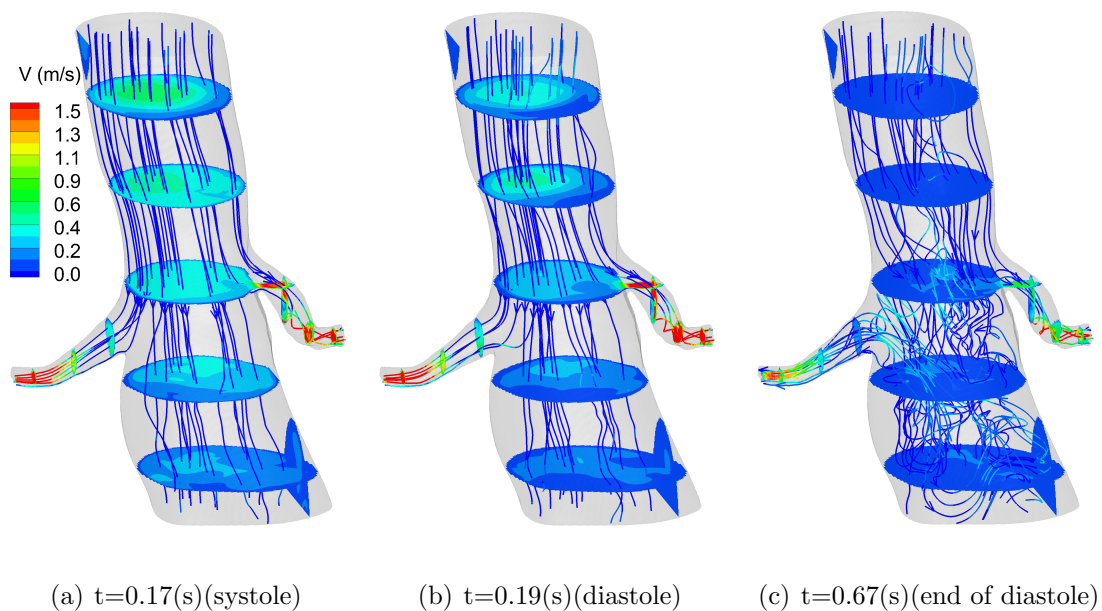


Figure 3.13. : Velocity contours and streamline for Case II

3.1.3 Case III

The segmented geometry of patient Case III from CTA using Mimic is shown in Figure 3.14. It has minor stenosis on LRA and RRA. Figure 3.16 shows the

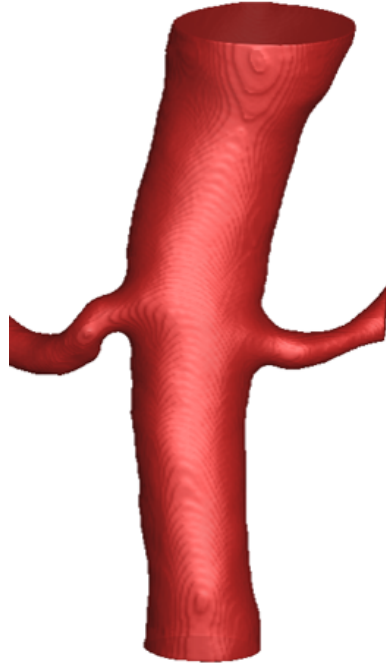


Figure 3.14. : Aortorenal system extracted from patient's CTA : Case III

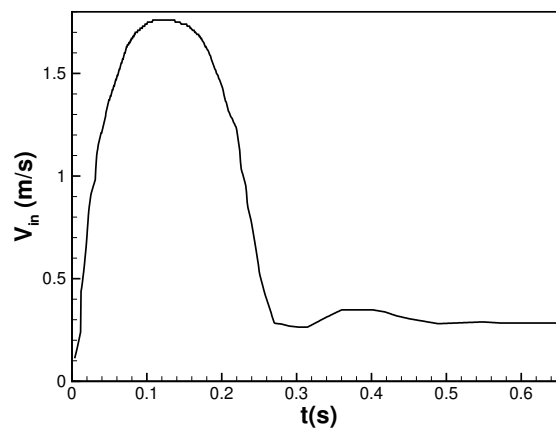


Figure 3.15. : Inlet velocity profile from DUS : Case III

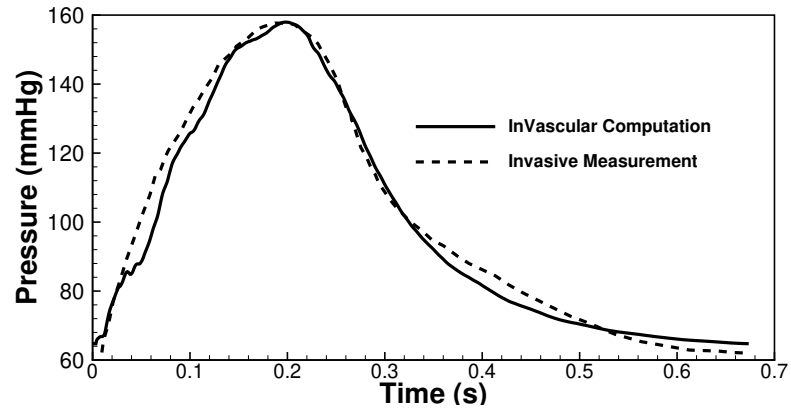
Table 3.5. : Values of resistances and compliances parameters in WK3 model at corresponding outlet of Case III

Outlets	r (dynes.s/cm^5)	R (dynes.s/cm^5)	$10^{-5}C$ (cm^5/dynes)
AA	87.992	2773.1	1.8
LRA	3533.04	9105.91	0.36
RRA	5412.88	13918.85	0.317

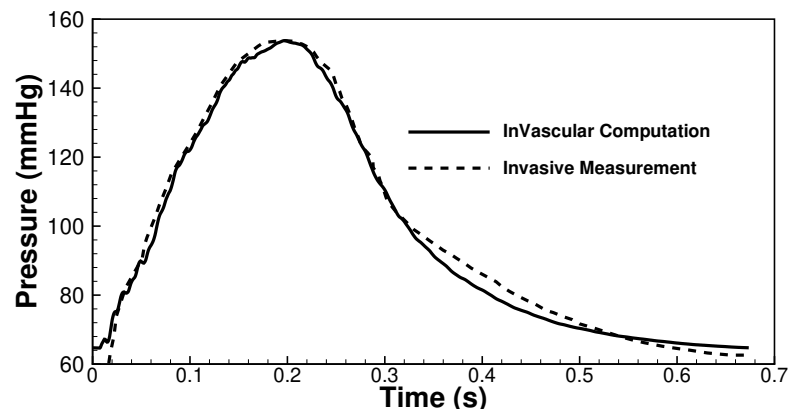
comparison of the cyclic pressure waves in (a) AA, (b) RRA, and (c)LRA between noninvasive computation (solid lines) and invasive measurement (dashed lines). The computed pressure waves agree very well with the medical measure images in both systole and diastole region. The comparison between noninvasive computation and invasive measurement is shown in Table 3.6. This case got one of the best comparison with invasive measurement.

Table 3.6. : Comparison of TSPG in LRA and RRA based on MAP or p_{sys} in Case III

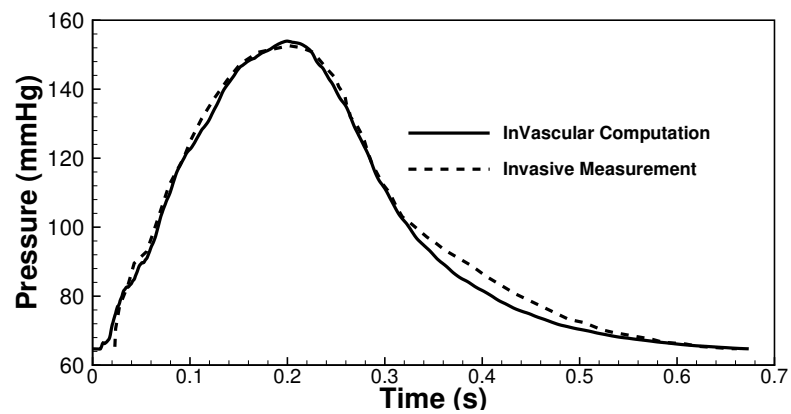
TSPG (mmHg)	MAP		P_{sys}	
	Noninvasive computation	Invasive measurement	Noninvasive computation	Invasive measurement
$p_{AA} - p_{LRA}$	4.0	4.05	2.6	2.0
$p_{AA} - p_{RRA,prox}$	4.0	4.01	2.6	1.30
$p_{AA} - p_{RRA,dist}$	6.0	5.9	2.0	2.0



(a) AA



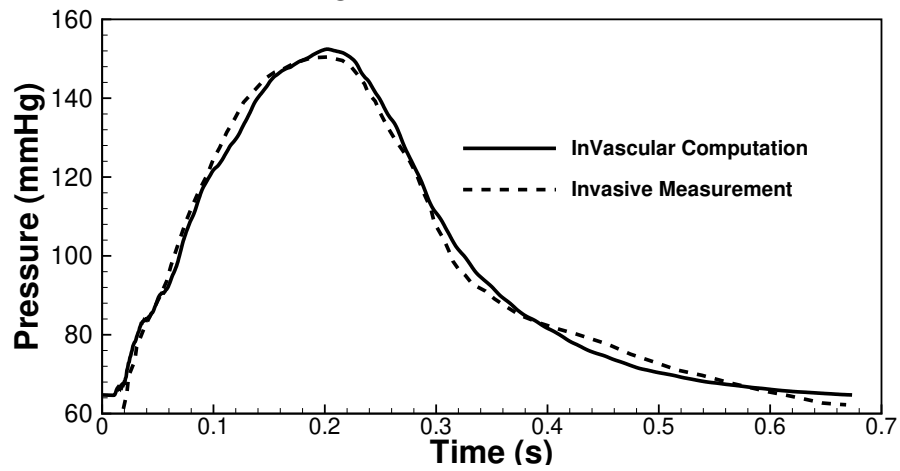
(b) LR



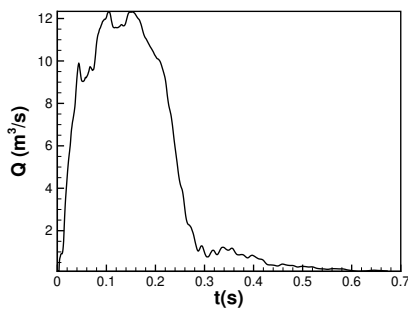
(c) RR proximal

Figure 3.16. : Comparison of pressure waves in Case III between noninvasive CHD (solid line) and invasive catheterization (dashed line)

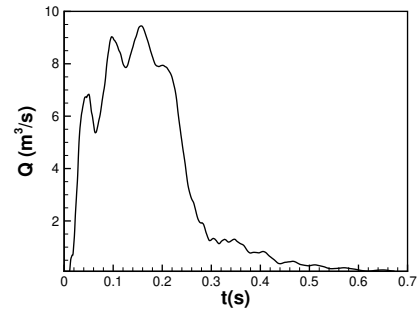
Figure 1.16 continued



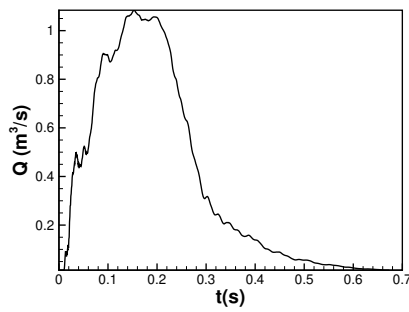
(a) RR distal



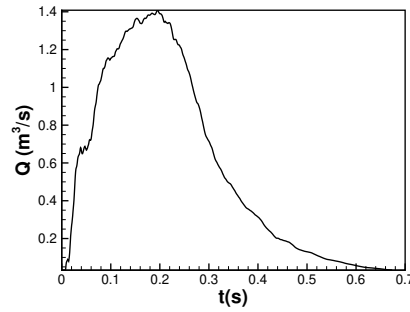
(b) AA near inlet



(c) AA near outlet



(d) RR



(e) LR

Figure 3.17. : Flowrate at different positions of aortorenal system for Case III

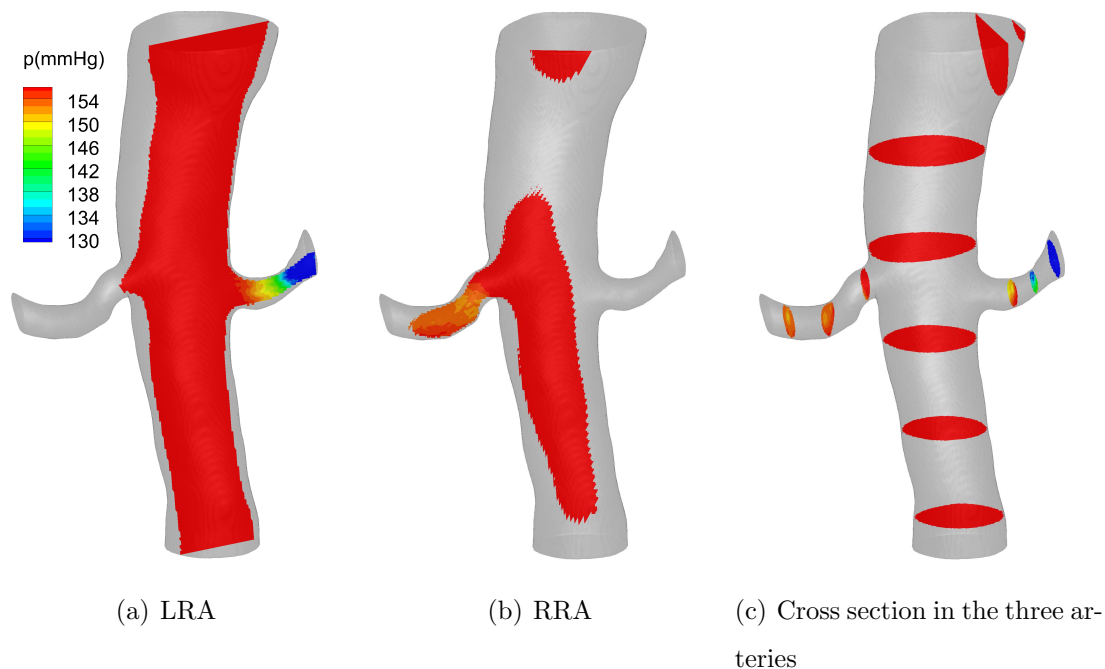


Figure 3.18. : Pressure contours at systole for Case III

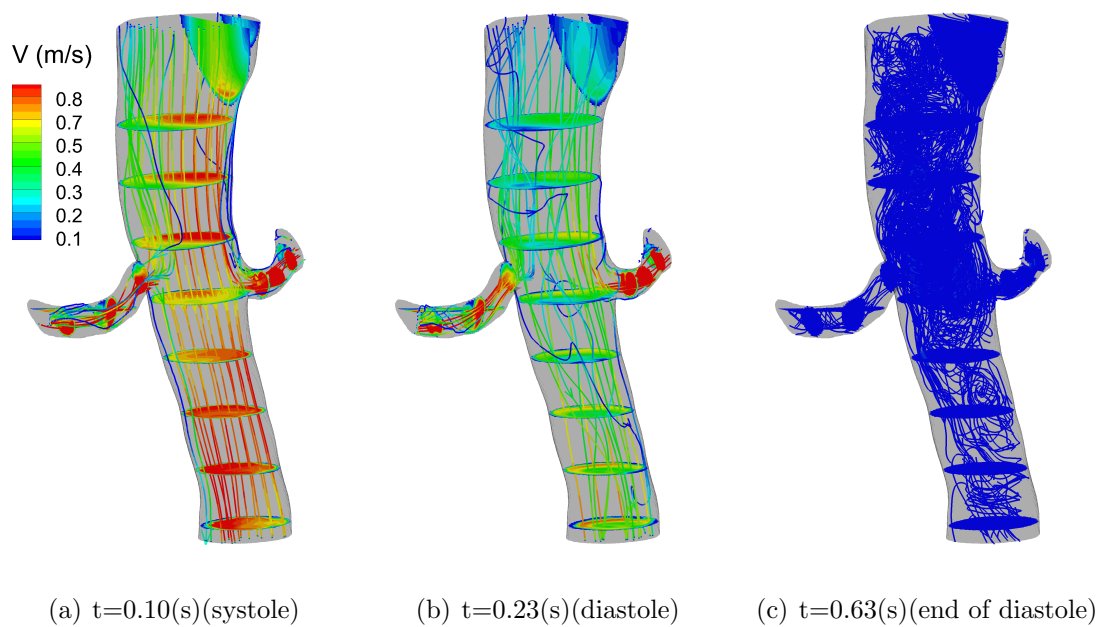


Figure 3.19. : Velocity contours and streamlines for Case III

Figure 3.18 shows 4-D pressure contour in different locations. Velocity field with magnitude contours and streamline respectively at (a) $t= 0.10(s)$, $b= 0.23 (s)$ and (c)= $.63 (s)$ in one cardiac cycle corresponding to systole (heart contraction, flow acceleration), diastole (heart relaxation, flow deceleration), and the end of diastole respectively are shown in 3.19.

3.1.4 Case IV

The segmented geometry of patient Case IV from CTA using Mimic is shown in Figure 3.20. The inlet velocity profile extracted directly from DUS is shown in Figure

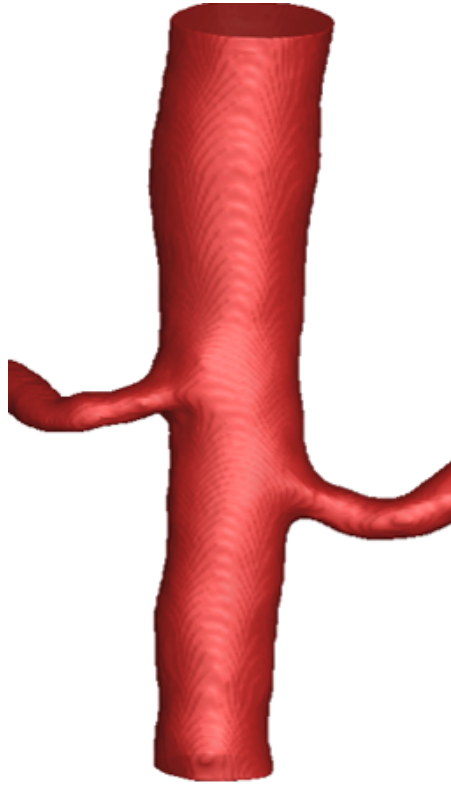


Figure 3.20. : Aortorenal system extracted from patient's CTA : Case IV

3.21. The r , R and c values used at each outlet tuned from DUS are shown in Table 3.7 Figure 3.22 shows the comparison of the cyclic pressure waves in (a) AA, (b) RRA, and (c) LRA between noninvasive computation (solid lines) and invasive measurement (dashed lines). For case IV, we find minor deviation in the beginning of systolic region and higher deviation in the diastolic region with the invasive measurement.

The TSPG was calculated via MAP and systolic pressure. The comparison between noninvasive computation and invasive measurement is shown in Table 3.8 The flow rate at each time point, calculated at Renal artery and Abdominal aorta near inlet and outlet, are shown in 3.23.

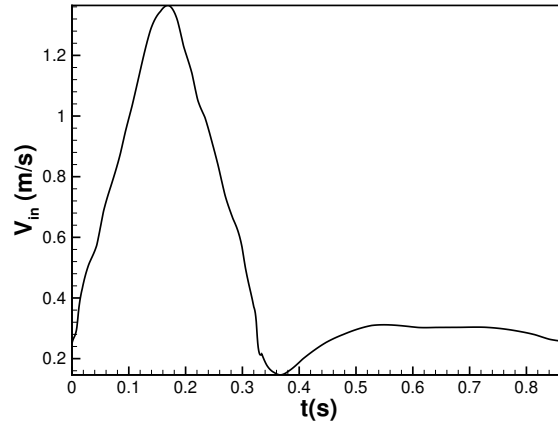
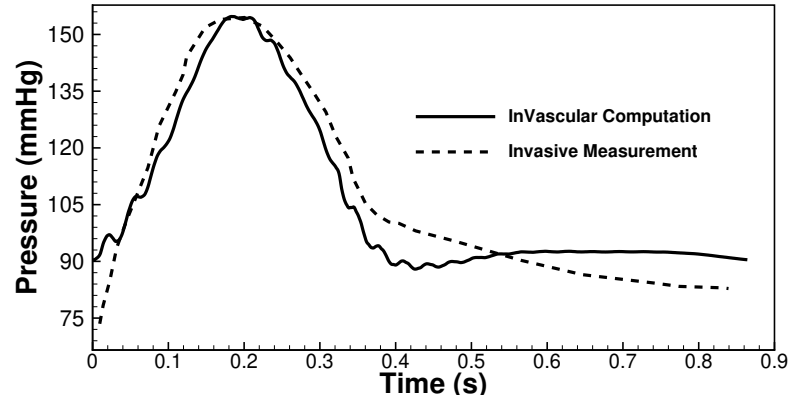


Figure 3.21. : Inlet velocity profile from DUS : Case IV

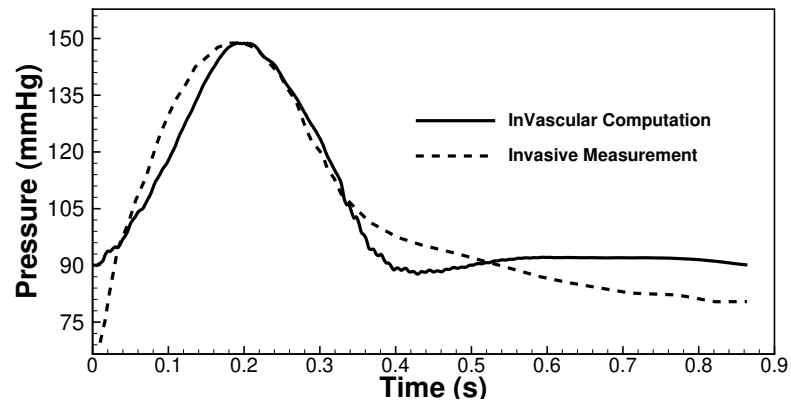
Table 3.7. : Values of resistances and compliances parameters in WK3 model at corresponding outlet of Case IV

Outlets	r ($dynes.s/cm^5$)	R ($dynes.s/cm^5$)	$10^{-5}C$ ($cm^5/dynes$)
AA	108.12	3386.38	1.0
LRA	2879.76	7386.06	0.54
RRA	3306.39	8505.96	0.476

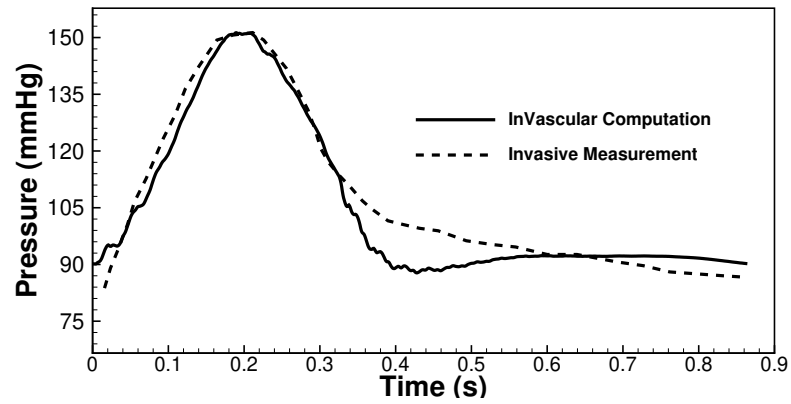
InVascular quantified 4-D pressure are shown in Figure 3.24. Velocity field with magnitude contours and streamline respectively at (a) $t= 0.19(s)$, b= $0.49(s)$ and (c)= $.82(s)$ in one cardiac cycle corresponding to systole (heart contraction, flow acceleration), diastole (heart relaxation, flow deceleration), and the end of diastole respectively are shown in 3.25.



(a) AA



(b) LR

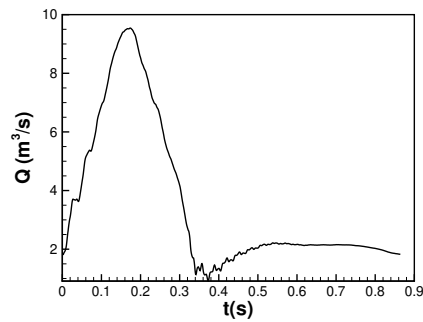


(c) RR

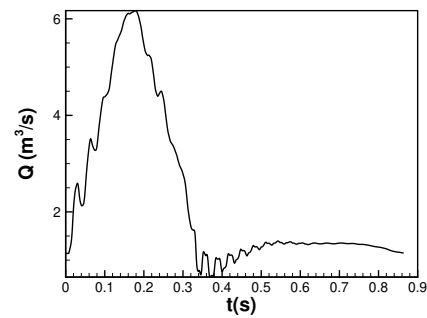
Figure 3.22. : Comparison of pressure waves in Case IV between noninvasive CHD (solid line) and invasive catheterization (dashed line)

Table 3.8. : Comparison of TSPG in LRA and RRA based on MAP or p_{sys} in Case IV

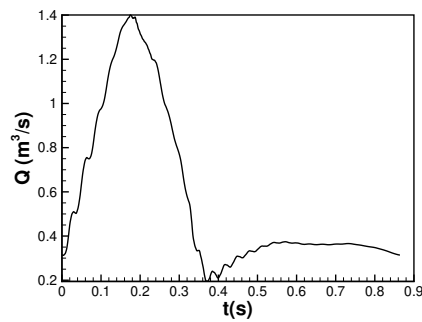
TSPG (mmHg)	MAP		P_{sys}	
	Noninvasive computation	Invasive measurement	Noninvasive computation	Invasive measurement
$p_{AA} - p_{LRA}$	5	5.1	3.0	2.0
$p_{AA} - p_{RRA}$	2.0	2.22	7.34	1.0



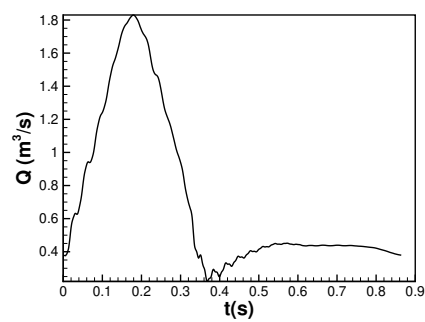
(a) AA near inlet



(b) AA near outlet



(c) RR



(d) LR

Figure 3.23. : Flowrate at different positions of aortorenal system for Case IV

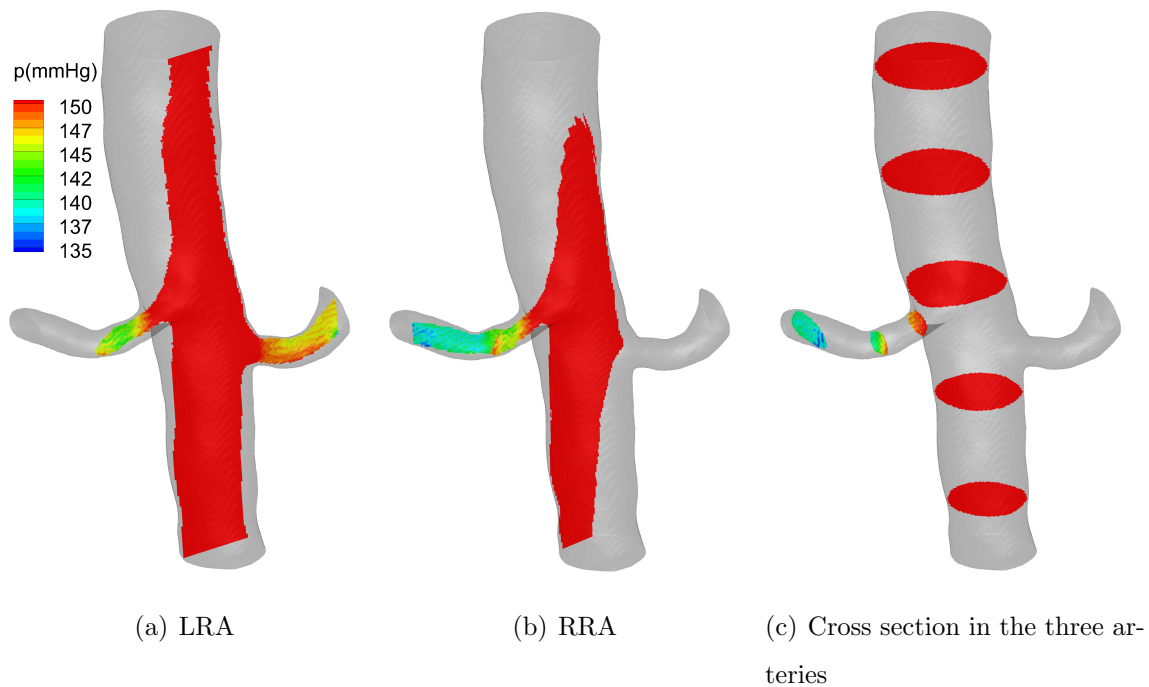


Figure 3.24. : Pressure contours at systole for Case IV

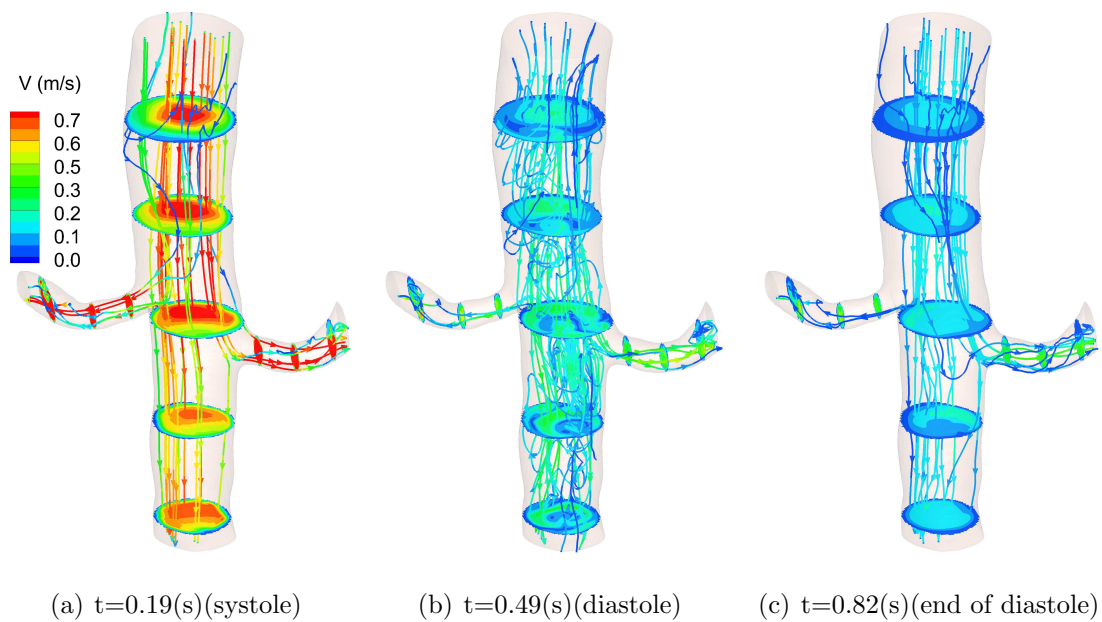


Figure 3.25. : Velocity contours and streamlines for Case IV

3.1.5 Case V

The segmented geometry of patient Case V from CTA using Mimic is shown in Figure 3.26. It has stenosis in LRA. The inlet velocity profile extracted directly from

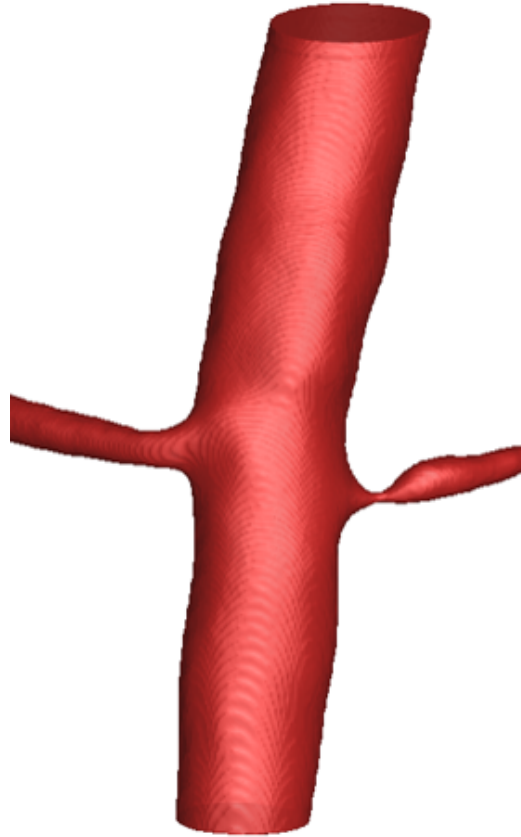


Figure 3.26. : Aortorenal system extracted from patient's CTA : Case V

DUS is shown in Figure 3.27. The r , R and c values used at each outlet tuned from DUS are shown in Table 3.9. Figure 3.28 shows the comparison of the cyclic pressure waves in (a) AA, (b) RRA, and (c) LRA between noninvasive computation (solid lines) and invasive measurement (dashed lines). For case V, the deviation is higher before surgery compared to after surgery between invasive and non-invasive measurement .

The TSPG was calculated via MAP and systolic pressure. The comparison between noninvasive computation and invasive measurement is shown in Table 3.10. *InVascular* quantified 4-D pressure are shown in Figure 3.30. Velocity field with

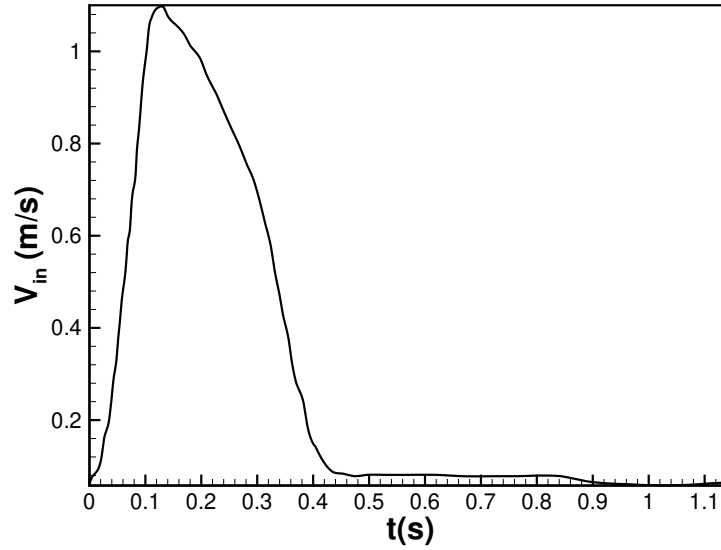
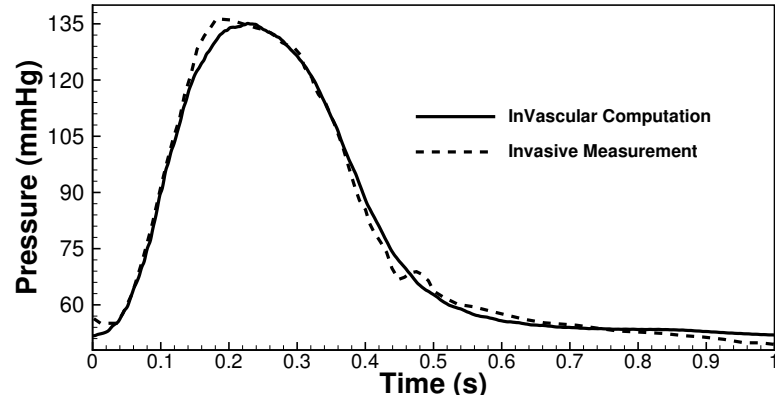


Figure 3.27. : Inlet velocity profile from DUS : Case V

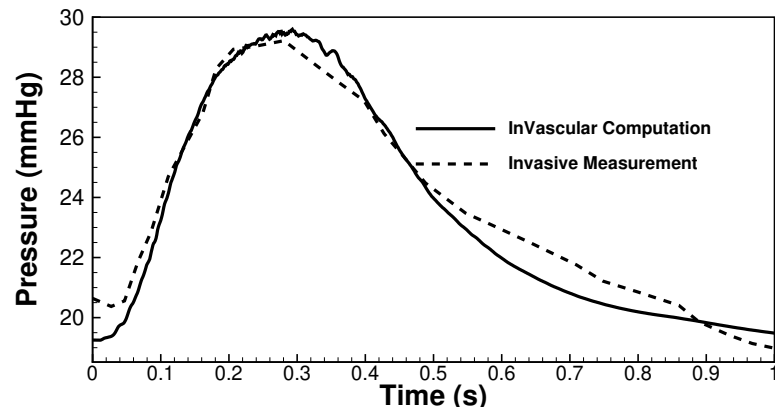
Table 3.9. : Values of resistances and compliances parameters in WK3 model at corresponding outlet of Case V

Outlets	r (<i>dynes.s/cm⁵</i>)	R (<i>dynes.s/cm⁵</i>)	$10^{-5}C$ (<i>cm⁵/dynes</i>)
AA	86.659	2719.77	3.14
LRA	3093.07	7959.34	0.18
RRA	3173.07	8159.3	0.72

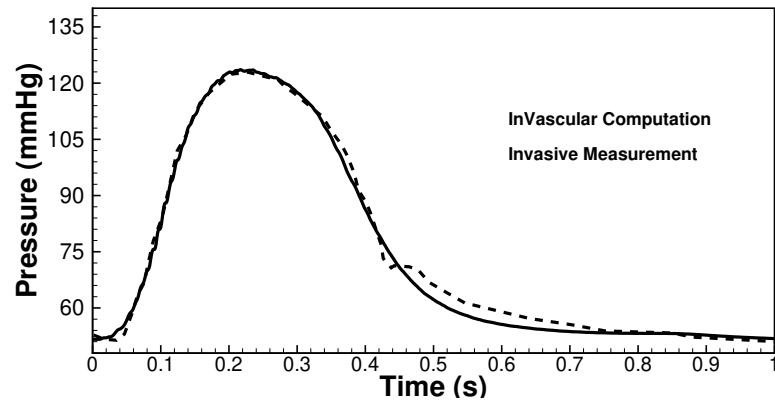
magnitude contours and streamline respectively at (a) $t= 0.34(s)$, $b= 0.90(s)$ and (c)= $1.08(s)$ in one cardiac cycle corresponding to systole (heart contraction, flow acceleration), diastole (heart relaxation, flow deceleration), and the end of diastole respectively are shown in 3.31.



(a) AA



(b) LR (before surgery)

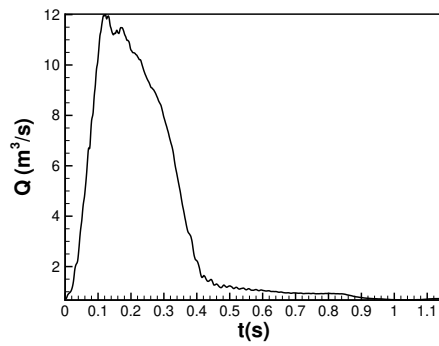


(c) LR (after surgery)

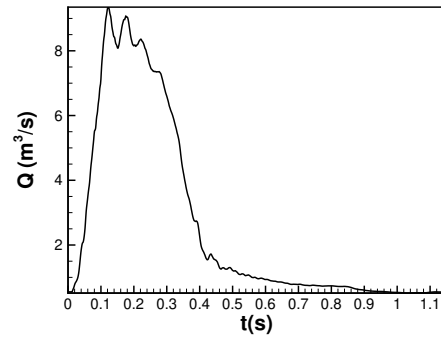
Figure 3.28. : Comparison of pressure waves in Case V between noninvasive CHD (solid line) and invasive catheterization (dashed line)

Table 3.10. : Comparison of TSPG in LRA and RRA based on MAP or p_{sys} in Case V

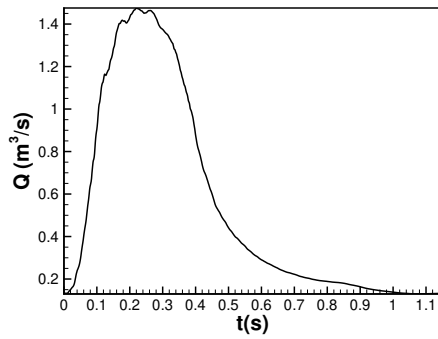
TSPG (mmHg)	MAP		P_{sys}	
	Noninvasive computation	Invasive measurement	Noninvasive computation	Invasive measurement
$p_{AA} - p_{LRA}$	11.8	12.0	5.0	7.0



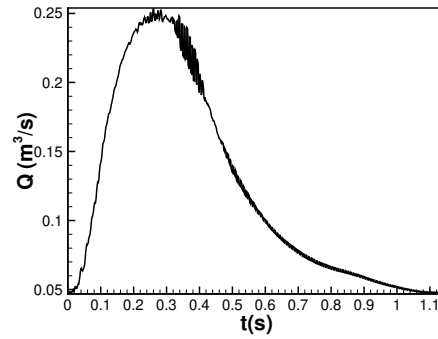
(a) AA near inlet



(b) AA near outlet



(c) RR



(d) LR

Figure 3.29. : Flowrate at different positions of the aortorenal system for Case V

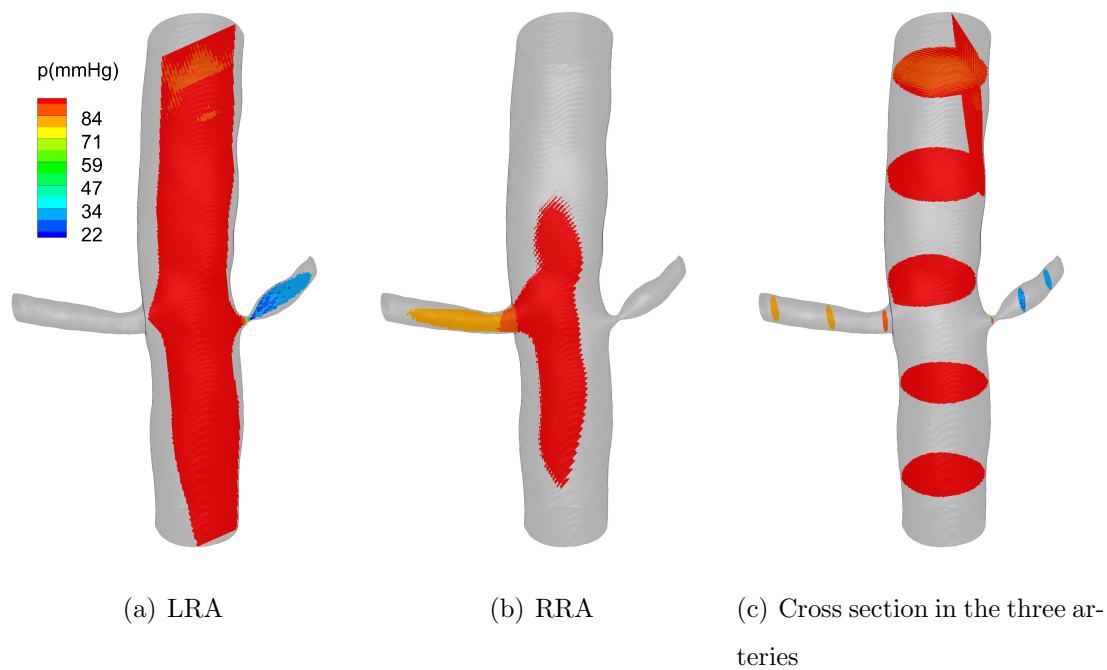


Figure 3.30. : Pressure contours at systole for Case V

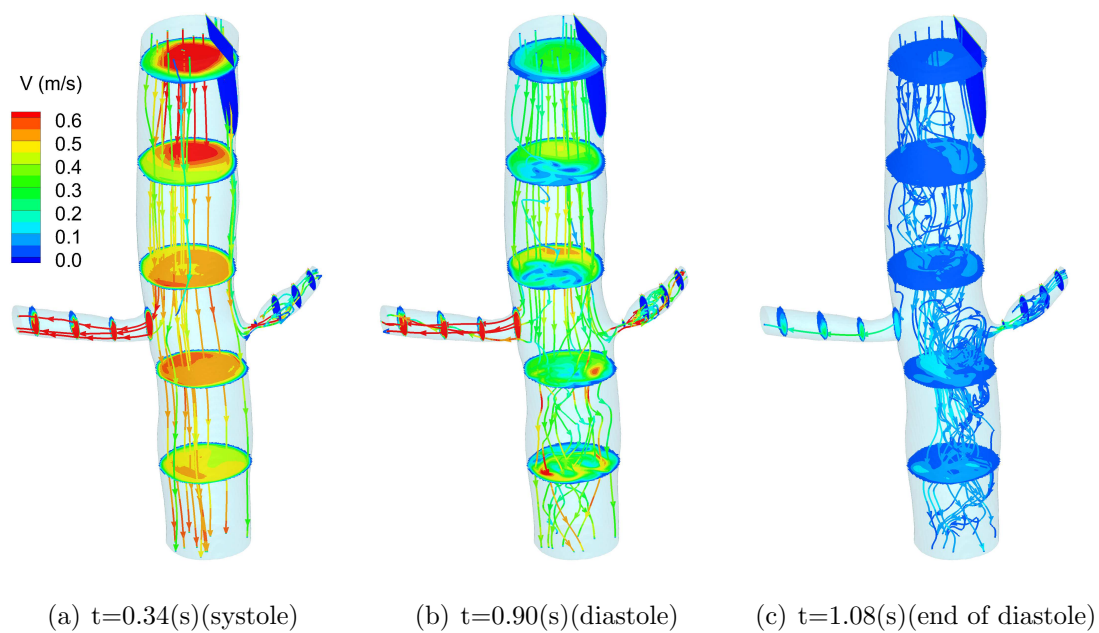


Figure 3.31. : Velocity contours and streamlines for Case V

In summary, the computed pressure waves agree very well with the medical measured images. We find good match in the systolic region but some deviation in the diastolic region with the invasive measurement. From streamline profile we find flow in AA is stronger in systole (a) than at diastole (b) but remains intensive in LRA and RRA at both time points and is better organized at systole than at diastole. Whereas at the end of diastole, the flow is weak, but chaotic.

3.2 Statistical analysis

A statistical analysis for Cases I-V including 14 artery samples demonstrates the statistical equivalence between the computed and measured blood pressure. The mean computed systolic blood pressure matches exactly with the in-vivo measured one i.e. 128 torr (mmHg). The mean difference between computed and measured systolic blood pressure was -0.14 torr (mmHg) $+0.32$ torr (mmHg). There was no difference in these values by the paired t-Test ($p=0.123$), with a value greater than 0.05, implying no statistical difference. As shown in Figure 3.32, the Bland-Altman plot of the data shows that only one measurement falls minimally outside the 95 percent confidence interval. The calculated systolic blood pressure were correlated with the measured one with a correlation coefficient of 1 ($p<0.001$) and the Beta values for a linear regression analysis was 0.003, demonstrating a consistent correlation between the pressures at all the measurements. The mean difference between computed and measured diastolic blood pressure was 5.00 torr (mmHg) $+7.37$ torr (mmHg), $p=0.02$. The mean difference between computed and measured mean blood pressure was 3.24 (mmHg) $+4.89$ torr (mmHg), $p=0.22$, which indicates a statistical difference between the calculated and measured values, so we cant go any further in this analysis.

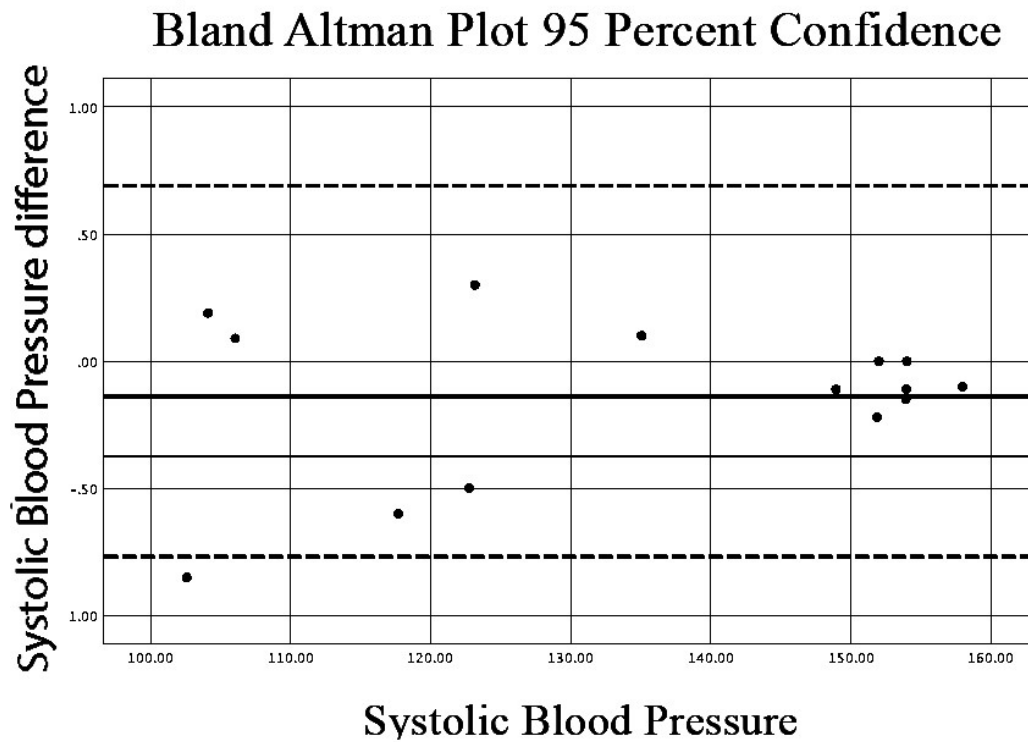


Figure 3.32. : Bland-Altman plot of 95% confidence for systolic blood pressure difference

3.3 Coronary artery

Besides aortorenal system, in this section we demonstrate the reliability of *InVascular* for the quantification of 4-D pressure field in coronary arteries. Velocity field with magnitude contours and streamline at systole, diastole and the end of diastole in one cardiac cycle have been shown. Figure 3.33 depicts the computation platform to quantify 4-D flow through *InVascular* in coronary artery. RCR boundary condition was employed for aorta and LPN was introduced at the outlet of each coronary artery.

The coronary artery was segmented using mimic is shown in Figure 3.34(a). But due to computational time and memory, it has been cut short. The main interest

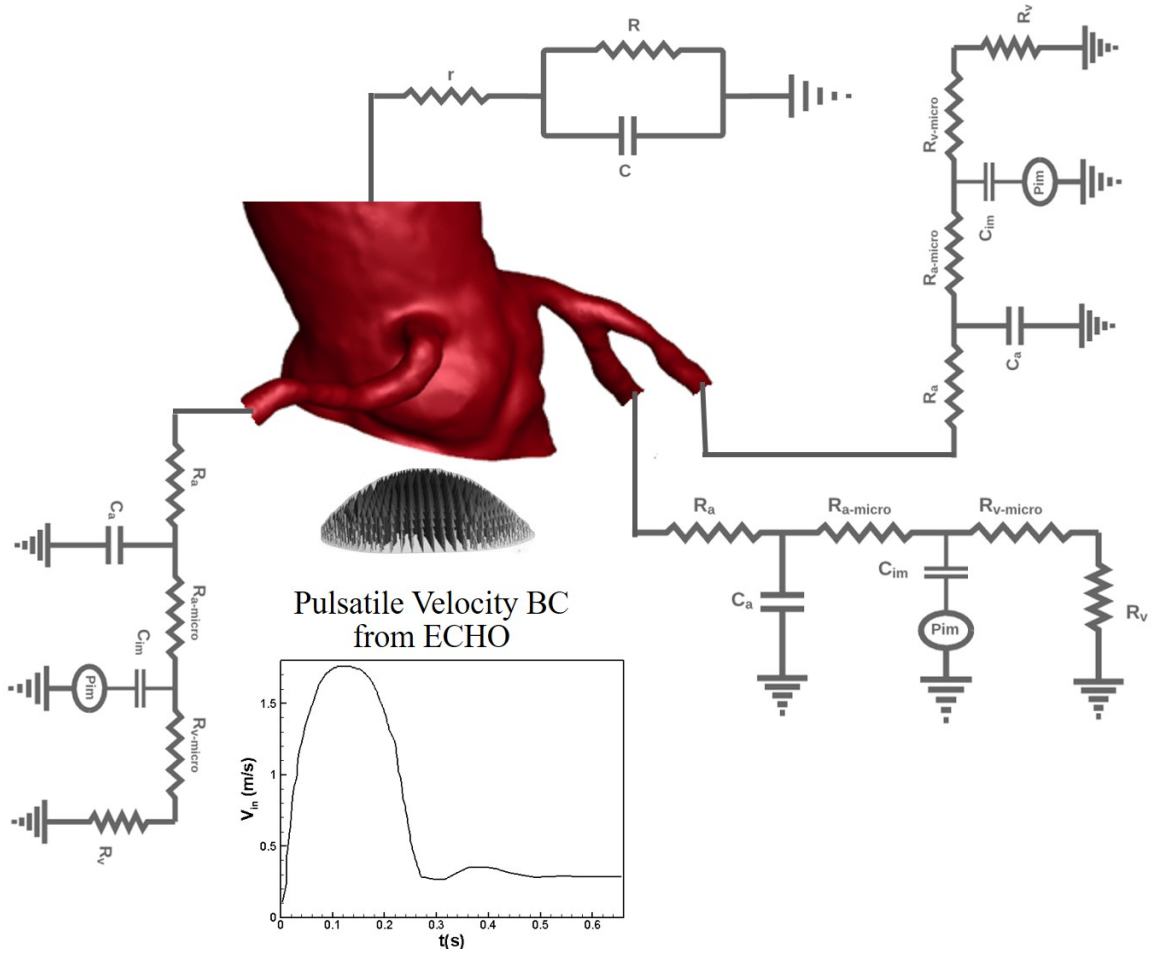


Figure 3.33. : Integration of *InVascular* with velocity BC from ECHO and pressure BC through the WK3 model at aorta and LPN at coronary artery

is stenosis in Left circumflex artery (LCX). So the region of computational platform is consists of Aorta, left circumflex artery and left anterior descending artery (LAD) and right coronary artery. The simulated part is shown in Figure 3.34(b). The inlet

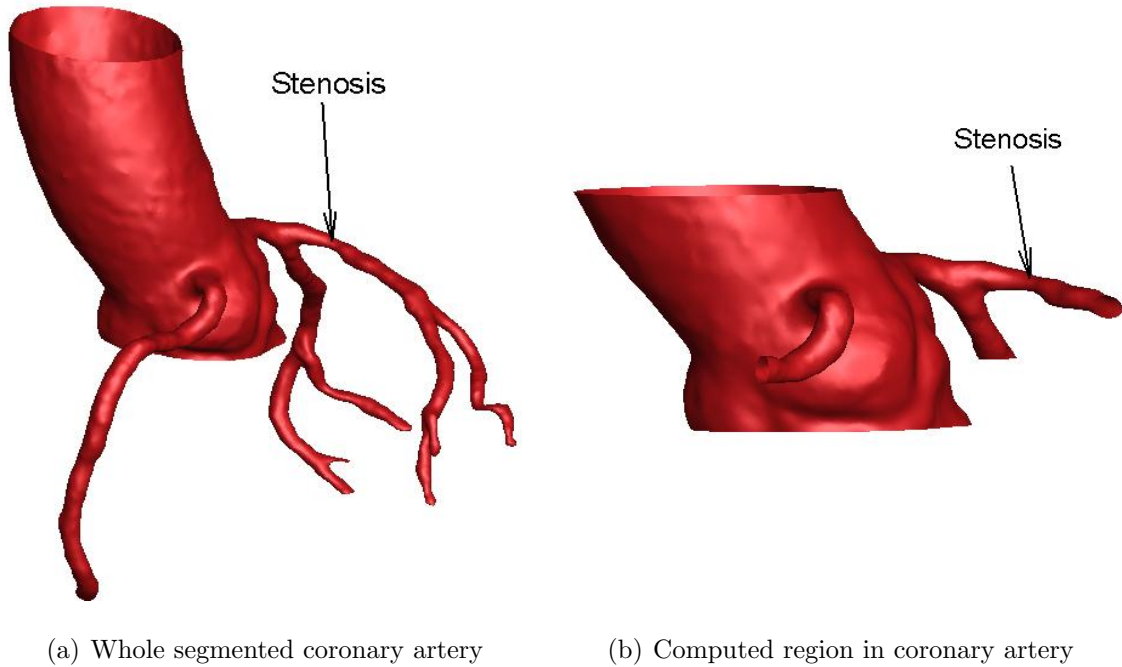


Figure 3.34. : Coronary artery extracted from patient's CTA

velocity profile extracted from ECHO is shown in 3.35. The corresponding values for LPN and WK3 model parameters are shown in Table 3.11 and 3.12. For coronary case, we received invasive measurement in ascending aorta, proximal and distal to stenosis in LCX artery. Figure 3.36 shows the comparison of the cyclic pressure waves. The computed pressure waves agrees well in the systolic region, but show deviation in the diastolic region. The deviation is much higher for the LCX artery distal to stenosis.

The MAP at proximal and distal to stenosis matches very closely with the invasive measurement. And also FFR agreement proves that *InVascular* is ideal to noninvasively capture the severity of CAS.

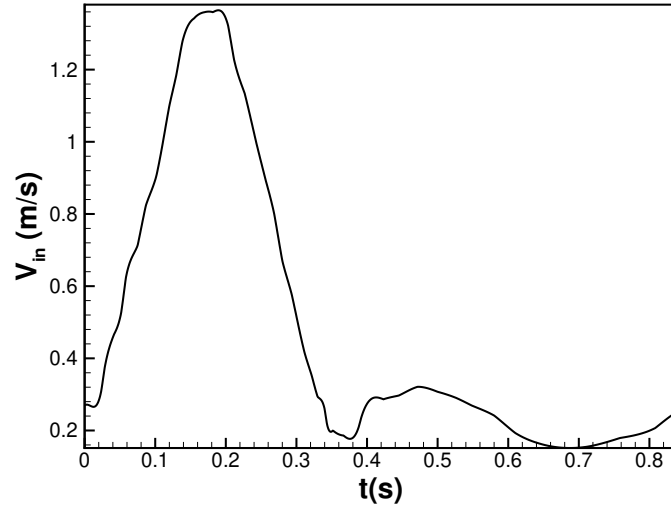


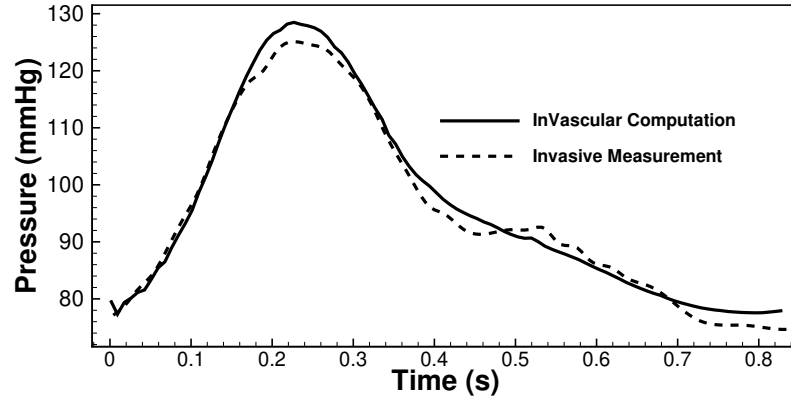
Figure 3.35. : Inlet velocity profile from ECHO.

Table 3.11. : Values of resistances and compliances parameters in LPN model at coronary outlet

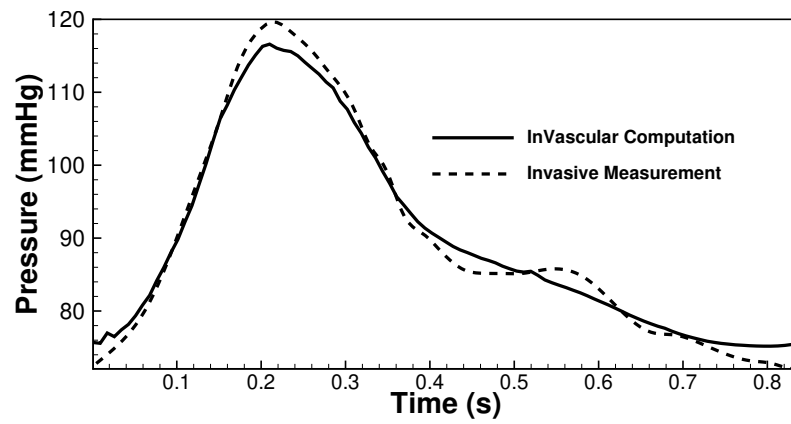
Outlets	R_a (dynes.s/cm ⁵)	$R_{a-micro}$ (dynes.s/cm ⁵)	$R_{v-micro} + R_v$ (dynes.s/cm ⁵)	$10^{-6}C_a$ (cm ⁵ /dynes)	$10^{-6}C_{im}$ (cm ⁵ /dynes)
LAD	23.21	37.722	11.607	0.0073	0.0594
LCX	9.496	15.43	4.75	0.018	0.01457

Table 3.12. : Values of resistances and compliances parameters in ascending aorta outlet

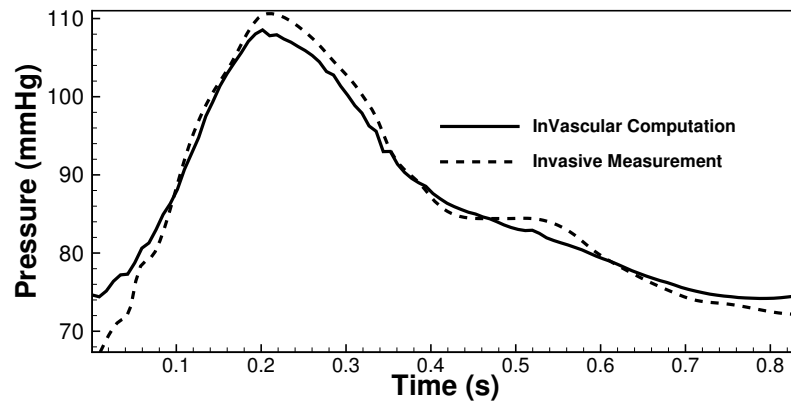
Outlets	$10^3 R_a$ (dynes.s/cm ⁵)	$10^3 R_d$ (dynes.s/cm ⁵)	$10^{-6}C$ (cm ⁵ /dynes)
Ascending Aorta	.157	1.549	50



(a) Ascending Aorta



(b) LCX artery proximal to stenosis



(c) LCX artery distal to stenosis

Figure 3.36. : Comparisons of pressure waves in coronary patient between noninvasive CHD (solid line) and invasive catheterization (dashed line)

Table 3.13. : Comparison of MAP and FFR in the LCX artery

Position	MAP		FFR	
	Noninvasive computation	Invasive measurement	Noninvasive computation	Invasive measurement
P_a	91	88	0.884	0.90
P_d	81.33	80		

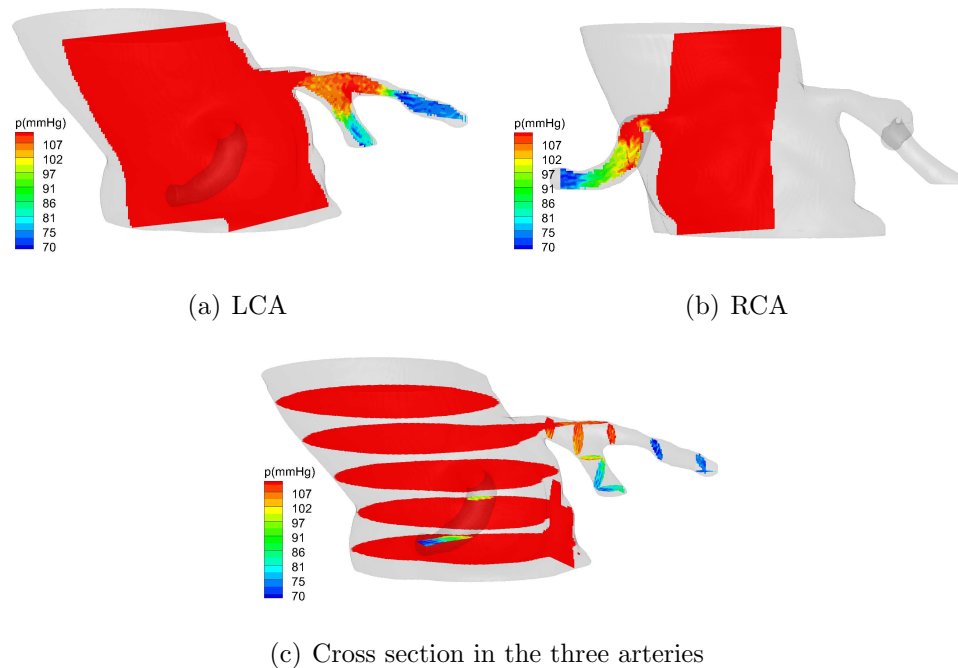


Figure 3.37. : Pressure contours at systole for coronary Case

InVascular quantified the 4-D pressure and velocity field in the coronary arterial system. Figure 3.37 shows pressure in left coronary artery, right coronary artery and cross section in the arteries. Comparing the pressure in the left and right coronary artery, we observe that pressure gradient between aorta and coronary artery is higher in the left coronary artery.

4. ASSESSMENT OF TRUE SEVERITY OF ARTERIAL STENOSIS AND THERAPEUTIC GUIDELINES

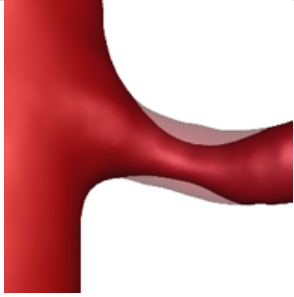
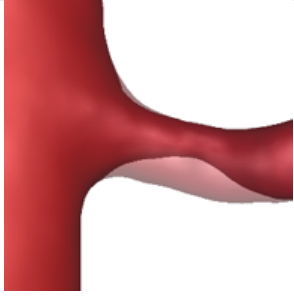
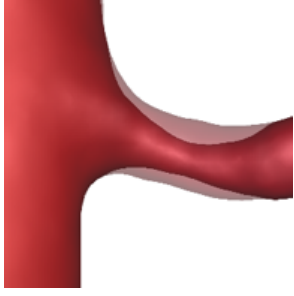
4.1 Characterization of stenosis degree : lumen diameter vs. volume reduction

Although the lumen diameter reduction of arterial stenosis is extensively used in current clinical practice to characterize the degree of stenosis, lumen volume reduction would be more related to the impact of stenosis on TSPG and FFR given the fact that the blood flow is 3-D. In table 4.1, two parametric scenarios are shown varying the lumen volume reduction from 38% to 60% for a renal artery with fixed lumen diameter reduction (75%) and varying the lumen diameter reduction from 53% to 69% for a RAS with fixed lumen volume reduction (45%). The TSPG of each stenosis is quantified by *InVascular*. In (a) with fixed diameter reduction, one percent volume reduction causes a 0.66 mmHg increase of TSPG whereas, in (b) with a fixed volume reduction, one percent diameter reduction causes a 0.2 mmHg increase of TSPG, implying that the volume reduction of the vessel lumen tracts closer to TSPG. Thus we use lumen volume reduction to establish the TSPG-S and FFR-S correlation below unless otherwise mentioned.

4.2 Assessment of true severity of RAS

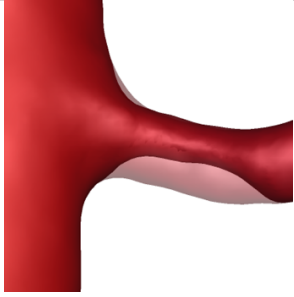
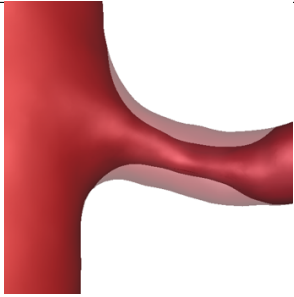
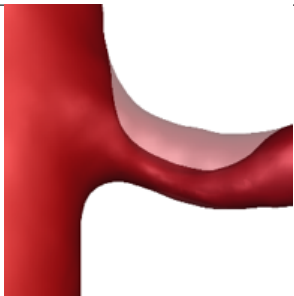
Parametric study was performed for cases IV, V and VI. For case IV, mild RAS were observed from computed tomography angiography (CTA) and stenting therapy were not done. For case V and VI, severe stenosis were found and stenting therapy were provided in clinical setting. Detailed results of case IV, V and VI in renal artery are presented. From *InVascular*, the mean TSPG and FFR-CT of existing stenosis (S_e) were computed. For determining how severe the RAS is, a computational analysis

Table 4.1. : Varying volume reduction from 38% to 60% for an RAS with fixed diameter reduction (75%)

Diameter reduction (%)	Volume reduction (%)	TSPG (mmHg)	Morphological geometry
75	38	46	
	50	62	
	60	84	

were performed via a parametric deterioration of the RAS by increasing lumen volume reduction, S , from 0% to 80% with an increment of 5%. It is noted that 0% of lumen volume reduction represents the scenario of no remaining stenosis (after stenting). Through *InVascular* quantification, the correlations between TSPG and mean FFR-CT vs. S were established for the cases. Based on the slope of the curves, S_m (mild)

Table 4.2. : Varying diameter reduction from 53% to 69% for an RAS with fixed volume reduction (45%)

Diameter reduction (%)	Volume reduction (%)	TSPG (mmHg)	Morphological geometry
45	53	44	
	60	50	
	69	50	

and S_s (severe) are identified for individual patients. The therapeutic guidelines for the RAS would be if $S_e < S_m$, no stenting is needed and if $S_e > S_s$, stenting therapy would be suggested. The dependence of the mean flow ratio, Q from renal artery and resistive index (RI) on S are also calculated.

4.2.1 Case IV-left renal artery

As shown in Figure 4.1, mild RAS were observed from computed tomography angiography (CTA) and stenting therapy were not done in the clinical setting.

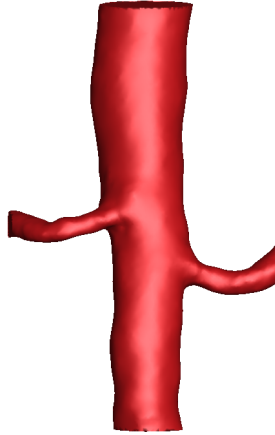


Figure 4.1. : Existing RAS extracted from CTA : Case IV LR artery

For determining the severity for the particular patients, computational analysis were performed through a parametric study of RAS by increasing lumen reduction, S , from 0% to 75% with an increment of 5%. Through CFD analysis, the correlation of systolic Peak systolic TSPG (left, solid line) and mean FFR-CT (right, dashed line) vs S . were shown in Figure 4.3. Based on the slope of the curves, S_m (mild) and S_s (severe) are identified as 30% and 50% for the particular patient respectively. The therapeutic guidelines for the RAS would be if $S_e < 30\%$, no stenting is needed and if $S_e > 50\%$, stenting therapy would be suggested. Since the $S_e (= 10\%)$ of the existing stenosis is smaller than 30%, the existing stenosis is assessed as mild and stenting therapy is not recommended, which agrees with the clinical practice for the patient.

The dependence of the mean flow ratio Q from AA to LRA (left, solid line) and RI (right, dashed line) on S are shown. From the Q-S correlation, 18% blood is supplied from AA to LR artery, suggesting that the kidney is getting enough blood and no sign of ischemia. The RI does not show a monotonic relationship with S .

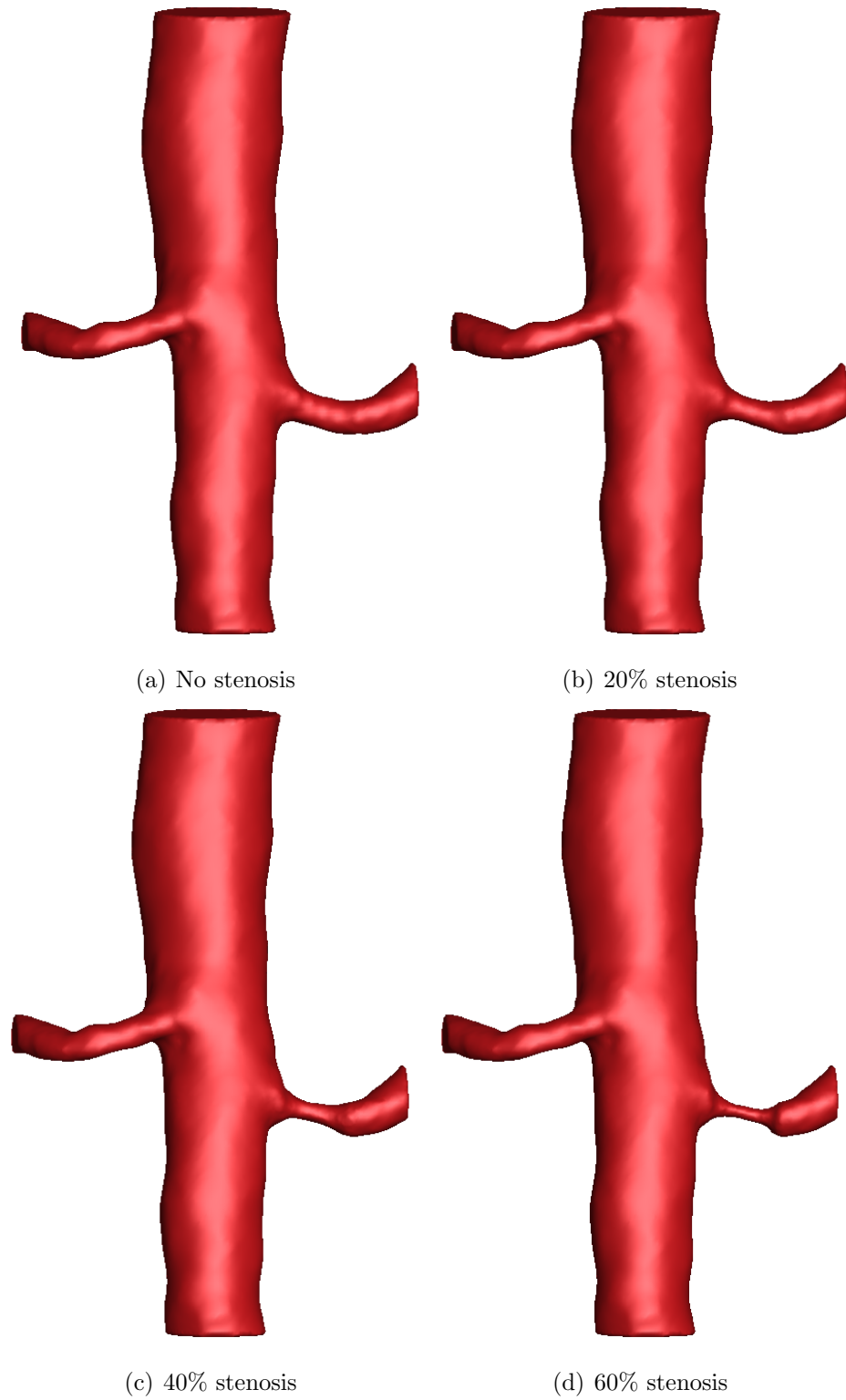


Figure 4.2. : Parametric deterioration of the RAS characterized by volume reduction of lumen: Case IV LR artery

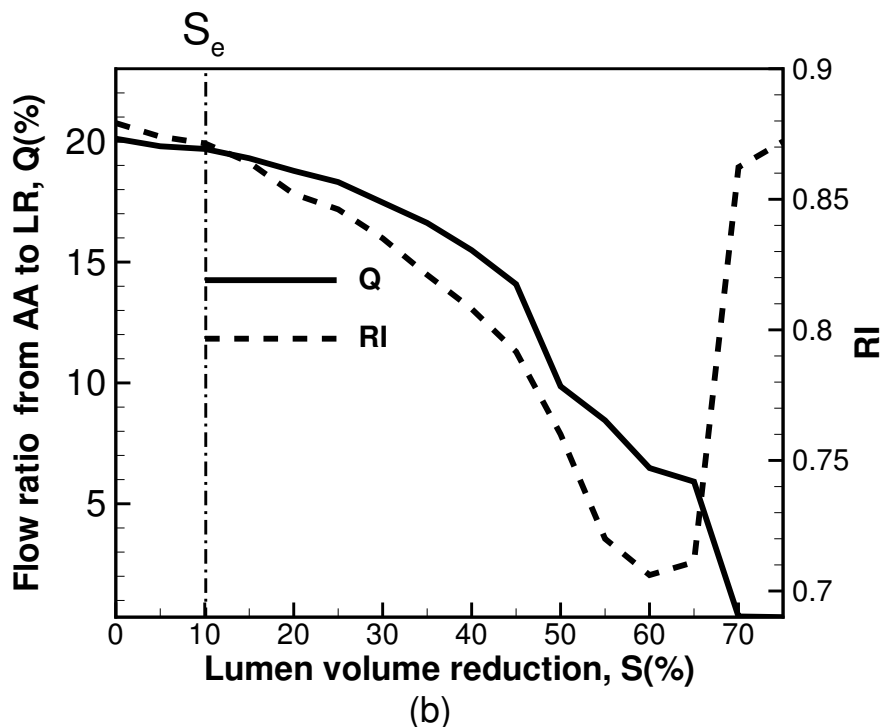
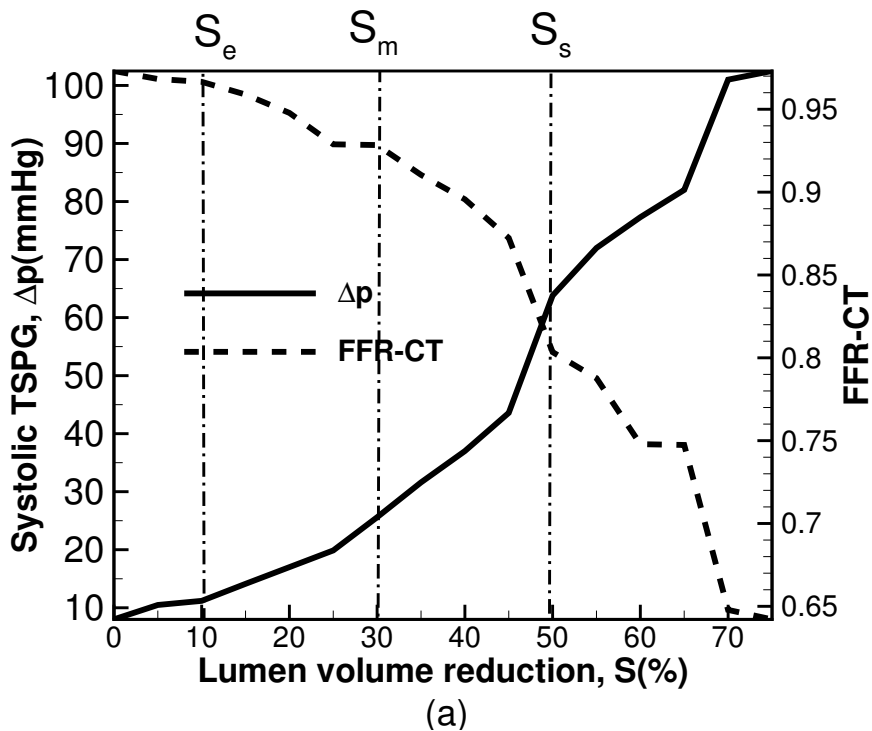


Figure 4.3. : Severity of the existing RAS in Case IV with volumetric lumen reduction 10%.(a) Correlation of pick systolic trans-stenotic pressure gradient, (left, solid line) and FFR-CT (right, dashed line) (b) Flow ratio from aorta to LR ,Q(left, solid line) and RI (right, dashed line) vs. volumetric stenosis degree.

4.2.2 Case IV-right renal artery

As shown in Figure 4.4, mild RAS were observed in right renal artery from CTA and stenting therapy were not done in the clinical setting.

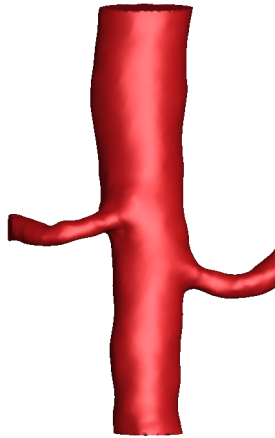


Figure 4.4. : Existing RAS extracted from CTA : Case IV RR artery

For determining the severity for the particular patients, computational analysis were performed through a parametric study of right RAS by increasing lumen reduction, S , from 0% to 75% with an increment of 5%. Through CFD analysis, the correlation of systolic Peak systolic TSPG (left, solid line) and mean FFR-CT (right, dashed line) vs S were shown in Figure 4.6. Based on the slope of the curves, S_m (mild) and S_s (severe) are identified as 30% and 50% for the particular patient respectively. The therapeutic guidelines for the RAS would be if $S_e < 30\%$, no stenting is needed and if $S_e > 50\%$, stenting therapy would be suggested. Since the $S_e (= 15\%)$ of the existing stenosis is smaller than 30%, the existing stenosis is assessed as mild and stenting therapy is not recommended, which agrees with the clinical patients for the patient. The dependence of the mean flow ration Q from AA to RR artery (left, solid line) and RI (right, dashed line) on S are shown. From the Q-S correlation, 12% blood is supplied from AA to RR artery, suggesting that the kidney is getting enough blood and no sign of ischemia. The RI does not show a monotonic relationship with S .

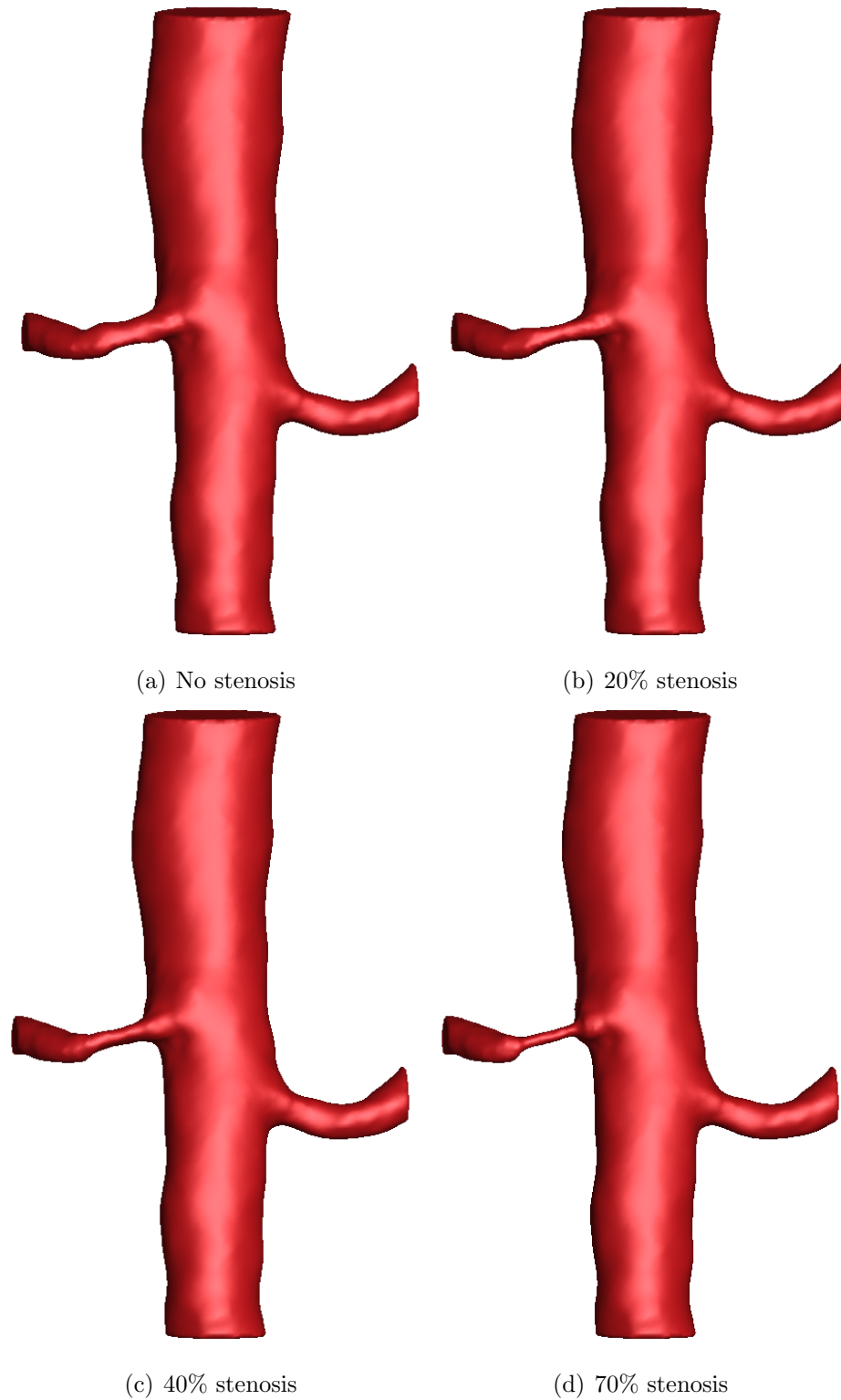


Figure 4.5. : Parametric deterioration of the RAS characterized by volume reduction of lumen: Case IV LR artery

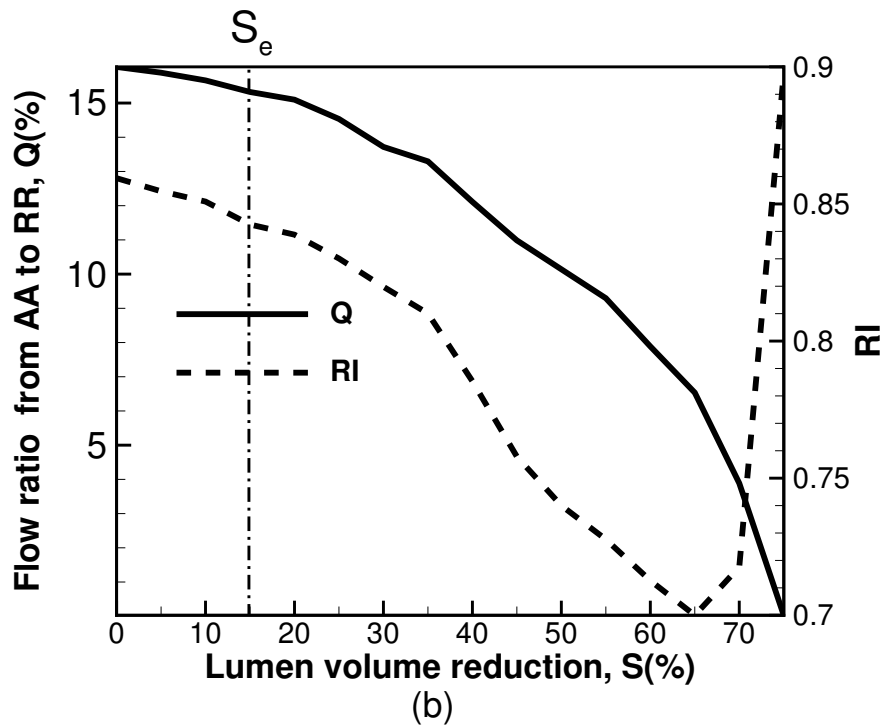
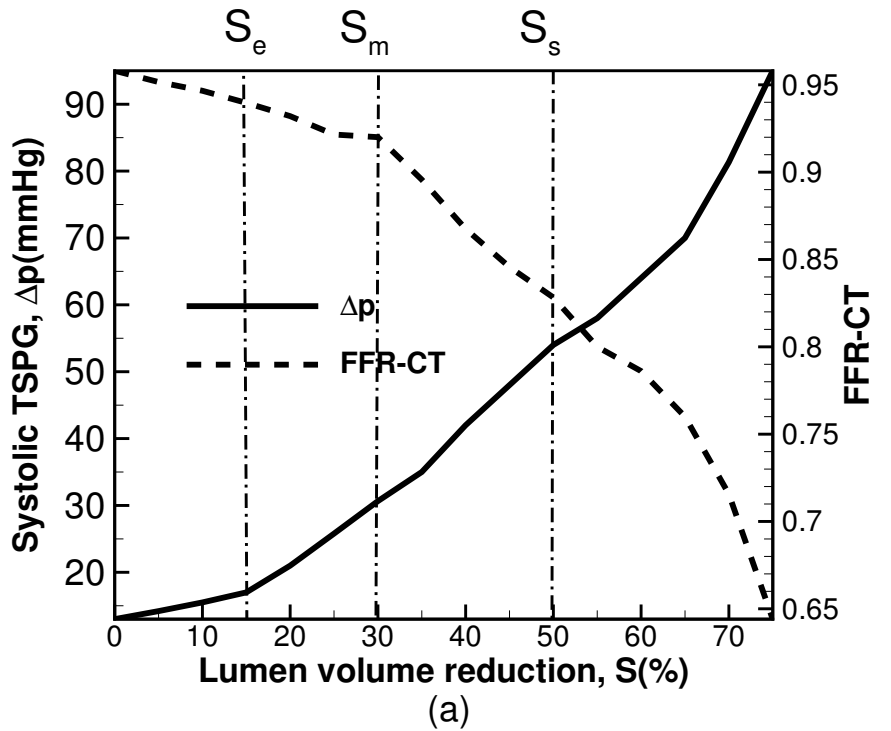


Figure 4.6. : Severity of the existing RAS with volumetric lumen reduction 15%.(a) Correlation of pick systolic TSPG, (left, solid line) and FFR-CT (right, dashed line) (b) Flow ratio from aorta to RR Q(left, solid line) RI (right, dashed line) vs. volumetric stenosis degree

4.2.3 Case V

As shown in Figure 4.7 , severe RAS were observed from CTA and stenting therapy were done in the clinical setting.

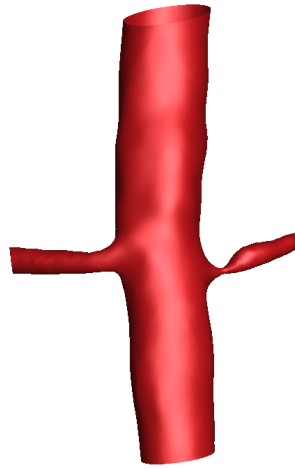


Figure 4.7. : Existing RAS extracted from CTA : Case V

For determining the severity for the particular patients, computational analysis were performed through a parametric study of RAS by increasing lumen reduction, S , from 0% to 75% with an increment of 5%. Through CFD analysis, the correlation of systolic Peak systolic TSPG (left, solid line) and mean FFR-CT (right, dashed line) vs S . were shown in Figure 4.9. Based on the slope of the curves, S_m (mild) and S_s (severe) are identified as 30% and 45% for the particular patient respectively. The therapeutic guidelines for the RAS would be if $S_e < 30\%$, no stenting is needed and if $S_e > 45\%$, stenting therapy would be suggested. Since the $S_e (= 55\%)$ of the existing stenosis is larger than 45%, the existing stenosis is assessed as severe and stenting therapy is suggested, which agrees with the clinical practice for the patient. The dependence of the mean flow ration Q from AA to LR artery (left, solid line) and RI (right, dashed line) on S are shown. From the Q-S correlation, only 5% blood is supplied from AA to LR artery, suggesting that the therapeutic treatment might benefit the patient. The RI does not show a monotonic relationship with S .

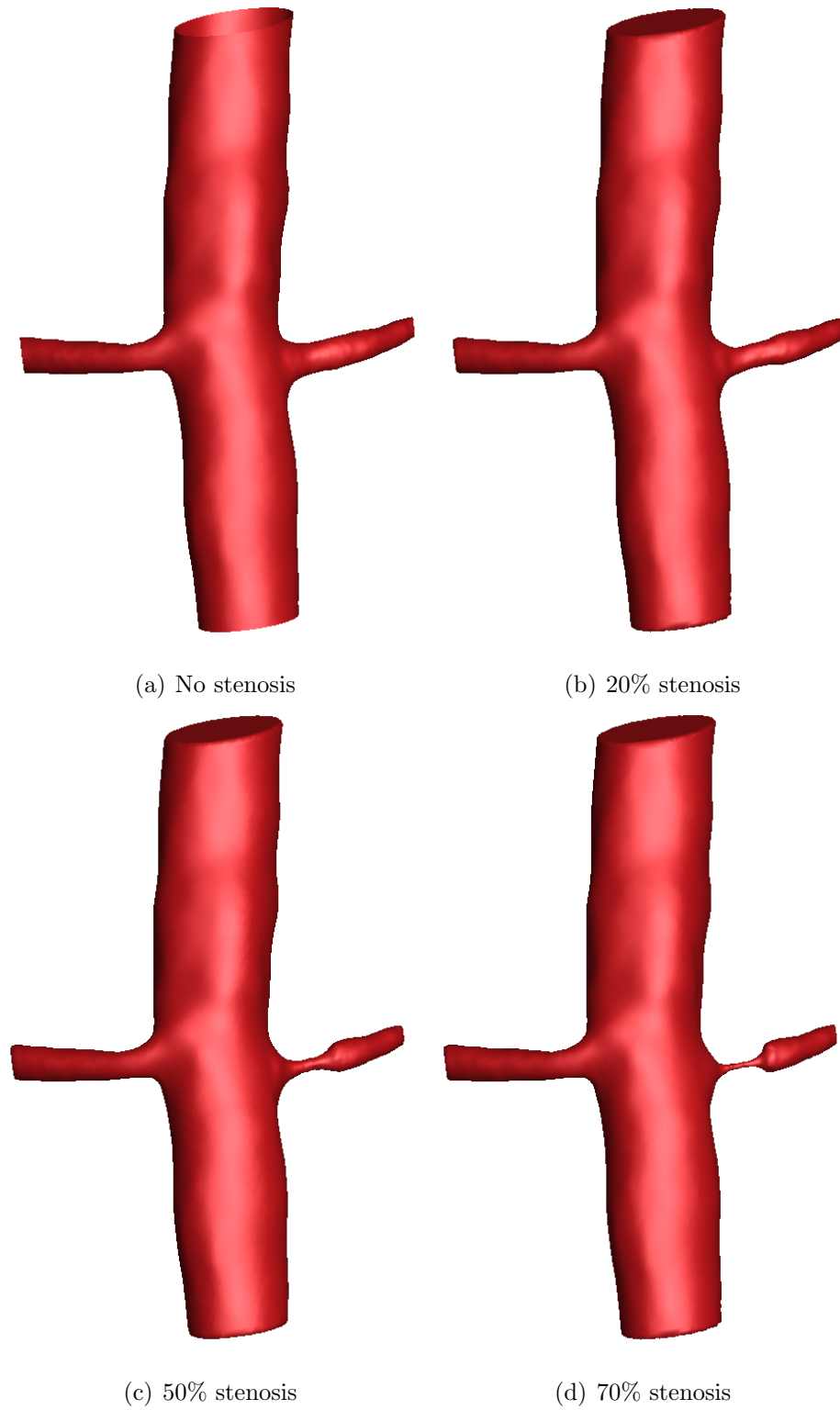


Figure 4.8. : Parametric deterioration of the RAS characterized by volume reduction of lumen: Case V

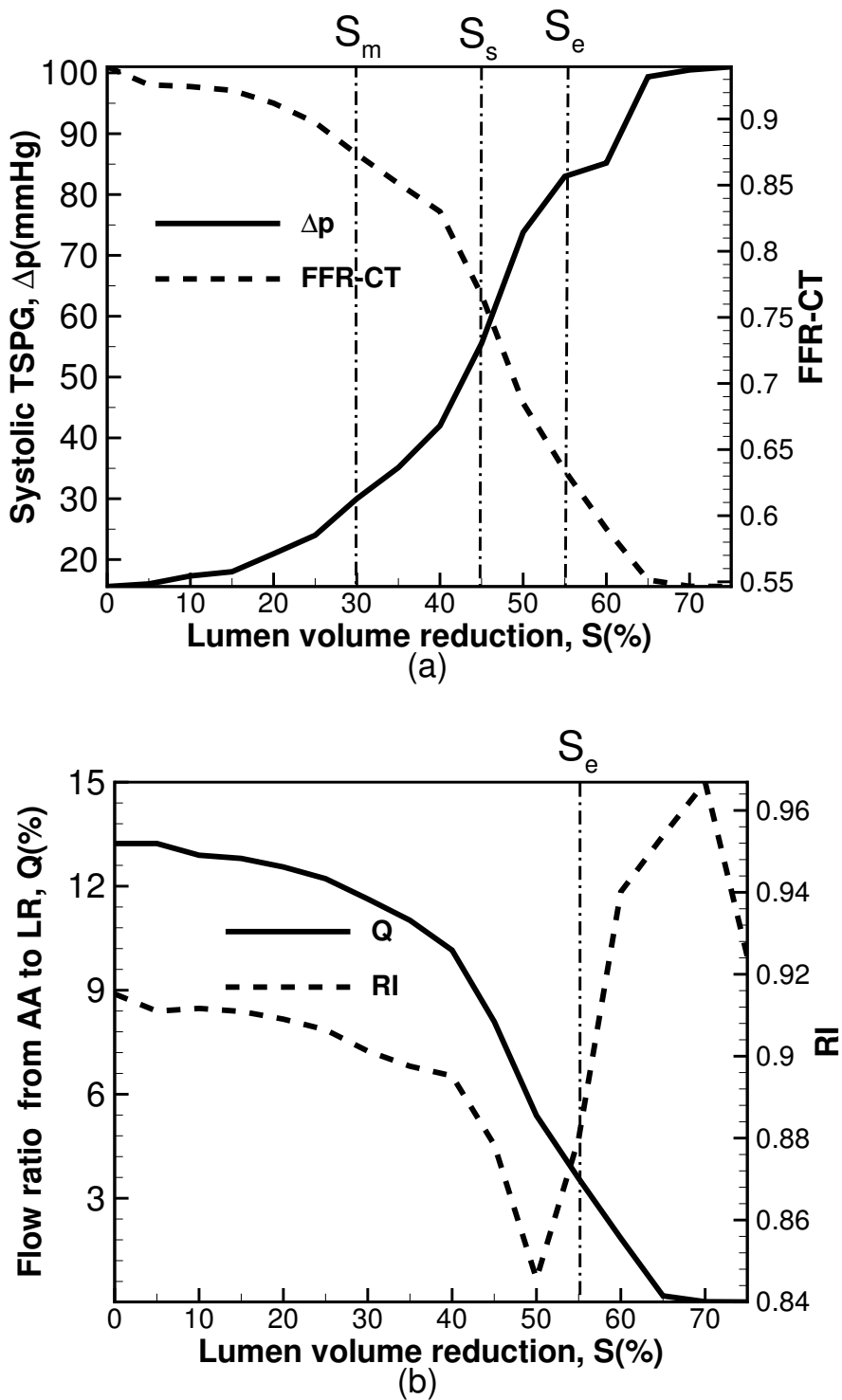


Figure 4.9. : Severity of the existing RAS in case V with volumetric lumen reduction 55%. (a) Correlation of pick systolic TSPG, (Δp (mmHg) and FFR-CT (right, dashed line) (b) Flow ratio from aorta to LR Q (left, solid line) and RI (right, dashed line) vs. volumetric stenosis degree

4.2.4 Case VI

As shown in Figure 4.13, severe RAS were observed from CTA and stenting therapy were done in the clinical setting.

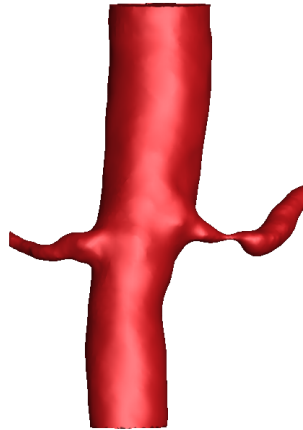


Figure 4.10. : Existing RAS extracted from CTA : Case VI

For determining the severity for the particular patients, computational analysis were performed through a parametric study of RAS by increasing lumen reduction, S , from 0% to 80% with an increment of 5%. Through CFD analysis, the correlation of systolic Peak systolic TSPG (left, solid line) and mean FFR-CT (right, dashed line) vs S . were shown in Figure 4.12. Based on the slope of the curves, S_m (mild) and S_s (severe) are identified as 30% and 40% for the particular patient respectively. The therapeutic guidelines for the RAS would be if $S_e < 30\%$, no stenting is needed and if $S_e > 40\%$, stenting therapy would be suggested. Since the $S_e (= 60\%)$ of the existing stenosis is larger than 40%, the existing stenosis is assessed as severe and stenting therapy is suggested, which agrees with the clinical practice for the patient. The dependence of the mean flow ration Q from AA to LR artery (left, solid line) and RI (right, dashed line) on S are shown. From the Q-S correlation, only 3% blood is supplied from AA to LR artery, suggesting that the therapeutic treatment might benefit the patient. The RI does not show a monotonic relationship with S .

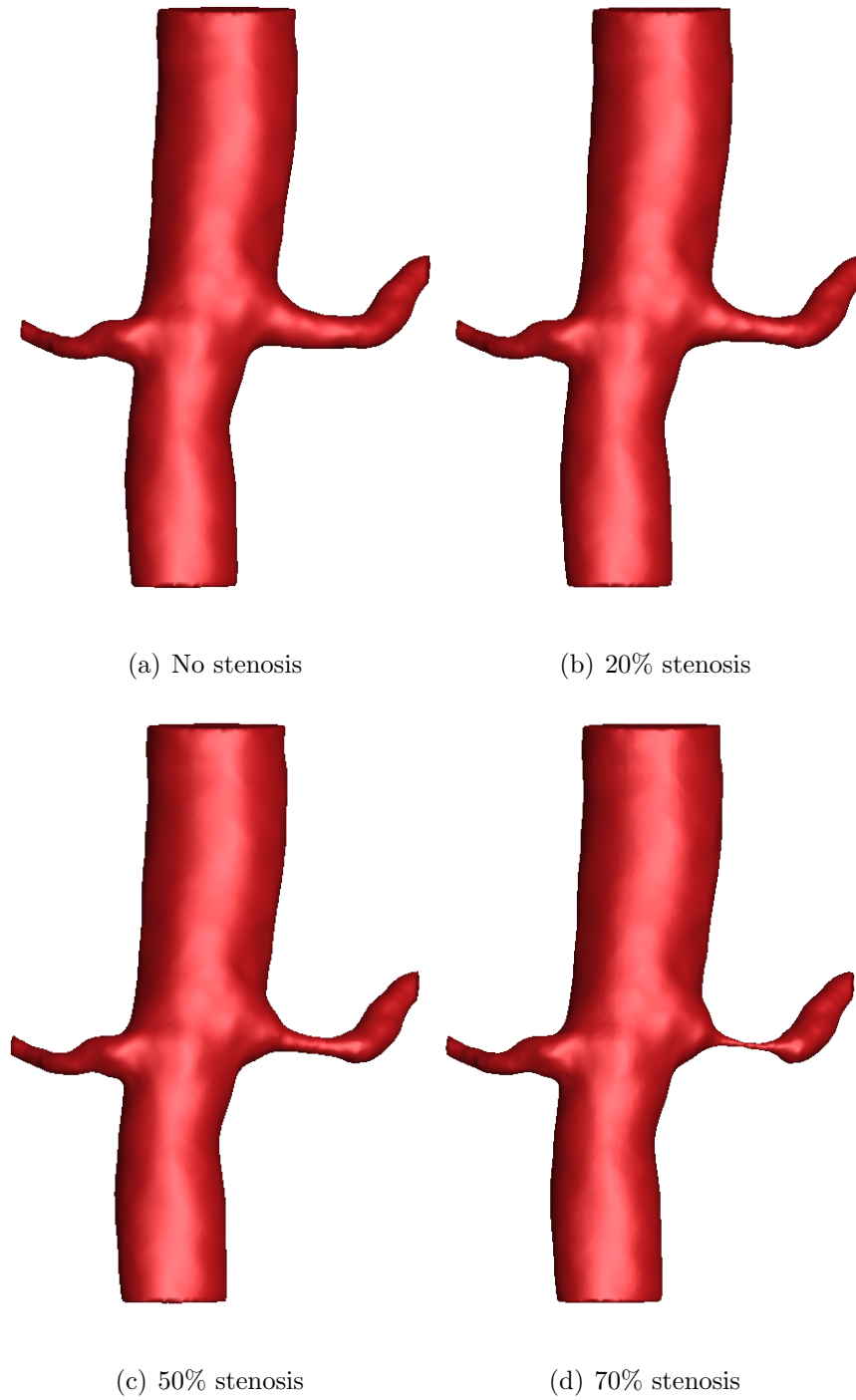


Figure 4.11. : Parametric deterioration of the RAS characterized by volume reduction of lumen: Case VI

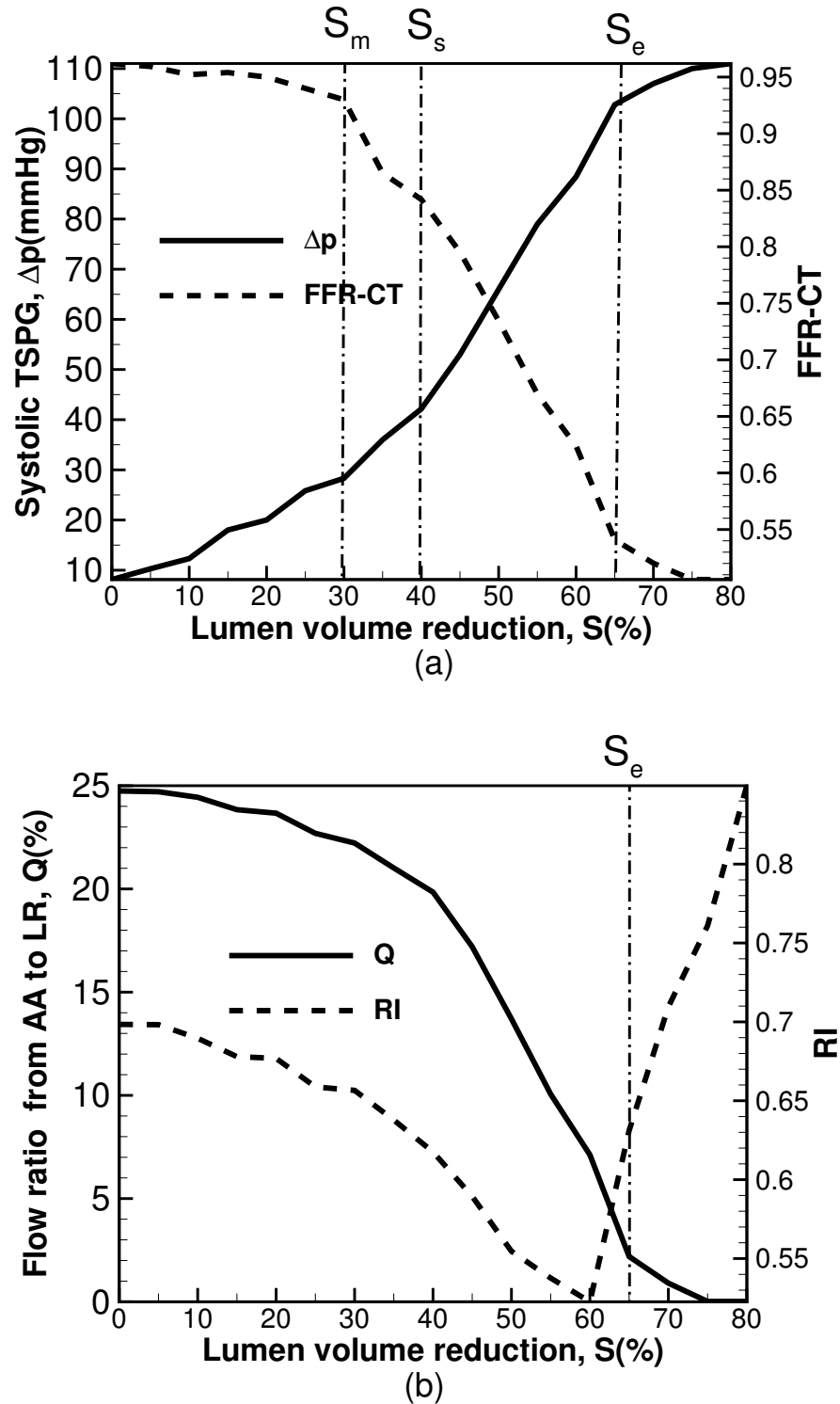


Figure 4.12. : Severity of the existing RAS in case VI with volumetric lumen reduction 65% .(a) Correlation of pick systolic TSPG, (left, solid line) and FFR-CT (right, dashed line) (b) Flow ratio from aorta to LR Q(left, solid line) and resistive index (RI) (right, dashed line) vs. volumetric stenosis degree.

4.3 Assessment of true severity of coronary arterial stenosis

Parametric analysis was performed for the selected patient case, in which mild stenosis were observed in clinical setting.

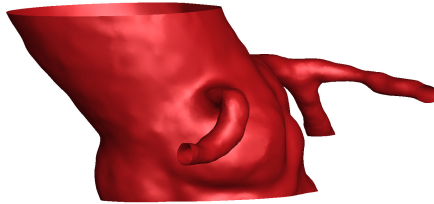


Figure 4.13. : Existing CAS extracted from CTA

From invasive study, FFR was 0.88 which conveys the stenosis as mild. We got close comparison between our noninvasive computation and invasive measurement in determining FFR. The main objective to do parametric study is to find FFR value noninvasively and find if TSPG can be a suitable guideline to determine the severity. Computational analysis were performed by varying the CAS from 0% to 70% with an increment of 5%. It is noted that 0% of lumen volume reduction represents the scenario of no remaining stenosis. Through *InVascular* quantification, the correlation of peak systolic TSPG (left, solid line) and mean FFR-CT (right, dashed line) vs. S were established in Figure 4.15(a). Based on the slope of the the curve and gold standard of the coronary assessment S_m (mild) and S_s (severe) are identified as 30% and 40%. Since the existing stenosis, $S_e < 30\%$, the CAS was assessed as mild which agrees with the clinic practice. So beside FFR, TSPG can be used to determine the true severity of coronary arterial stenosis, and *InVascular* is reliable to asses the CAS. From 4.15(b), we see the current flow througth the LCX artery is $0.085 \text{ m}^3/\text{s}$ which indicates no sign of ischemia. Also from our quantification, doctor can determine the flow in the coronary artery after stenting (0% stenosis) that will help to find the potential benefit of the stenting for particular patient. Till now, we can not comment on RI over CAS, as we have only completed single case.

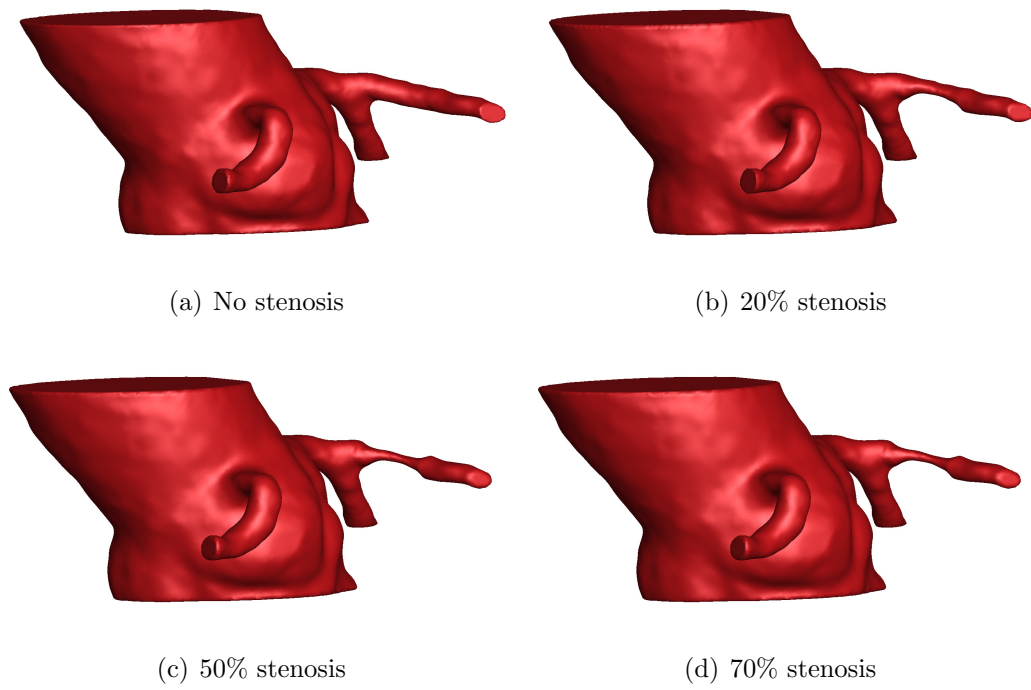


Figure 4.14. : Parametric deterioration of the CAS characterized by volume reduction of lumen

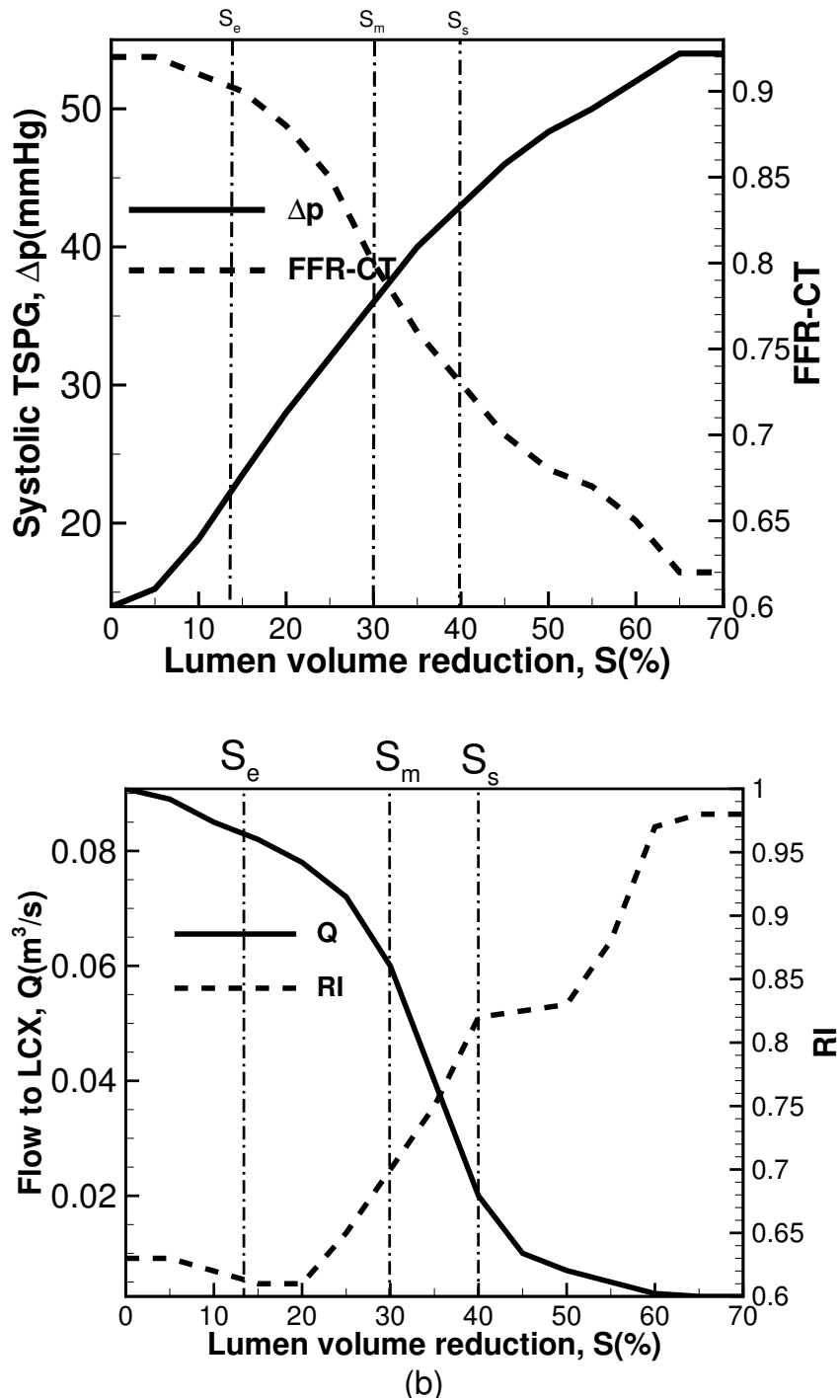


Figure 4.15. : Severity of the existing CAS with volumetric lumen reduction 13%. (a) Correlation of pick systolic TSPG, (left, solid line) and FFR-CT (right, dashed line) (b) Flow from aorta to LCX Q (left, solid line) and resistive index (RI) (right, dashed line) vs. volumetric stenosis degree

5. SUMMARY

In this study, the noninvasive *InVascular* was applied to the coronary and renovascular bed. The good agreement between computed and measured pressure in all aortic artery, coronary artery, left and right renal arteries demonstrate the reliability of *InVascular*. The derivation of the critical stenosis degrees S_m (mild) and S_s (severe) indicates the potential applicability of *InVascular* to provide useful guidelines for decision making of therapeutic intervention. It is noted that *InVascular* is robust and can potentially be applied to not only the renal and coronary vascular bed but also other vascular beds such as carotid, cerebral, mesentric, aortoiliac and femoropopliteal to assess the benefits of vascular interventions before an intervention is done. This will greatly aid in surgical decision making to plan procedures which might benefit a patient and limit procedures, which may not be beneficial. This methodology will be applied to these other vascular beds broadening its applicability.

Although *InVascular* well quantifies the systolic pressure with no statistical difference ($P < 0.001$) from the invasive measurement, the computed diastolic pressure has a marginal deviation from the measured diastolic pressure ($P = 0.02$) and larger difference is seen between mean computed and measured pressure ($P = 0.22$). It is speculated that disagreement might be due to the invasive catheterization that possibly disturbs the local blood flow, more significantly in diastole than systole. In order to confirm this speculation, we have built a laboratory experiment to measure the blood pressure in the aortorenal and coronary system (from 3-D) system with the same flow environment. If the computed and lab measured pressure have much smaller deviations, the impact of catheterization to the quantification of TSPG or FFR can be assessed. Due to lack of available data, the validation of the velocity quantification has not been conducted. The determination of the thresholds of S_m (mild) and S_s (severe), which are the key values for surgical decision making, is preliminary

for renal artery as there does not exist a gold standard for either TSPG or FFR-CT for RAS. But for coronary artery S_m (mild) and S_s (severe) was determined based on the gold standard. The current work primarily focuses on the methodology of the new technique and its reliability for medical application. The data obtained from this work are crucial for translational studies to move to medical use. While noninvasive and patient-specific assessment of the true severity of RAS and CAS is promising to advance the vascular surgery management with cost reduction and better quality of life, there remains critical questions to be answered such as "Which is more appropriate to determine the severity of RAS, TSPG or FFR-CT?" "Is there a gold standard for RAS?" "What patient group will be benefited?" and so on so forth. To answer these questions, a powerful research tool such as *InVascular* is critical for non-invasive evaluating patients who might be potential candidate for large medical trials. Meanwhile, real blood flow is non-Newtonian and real vessels are deformable. There often exists multiple or bilateral stenosis in one patient. Adding more modeling components to mimic the real-world vascular system in *InVascular* will be a continuous effort.

Currently, FFR-CT analysis for coronary stenosis with an existing gold standard for invasive FFR is solely available via a centralized commercial web-based service of the HeartFlow company. Time-consuming computational demands, high cost, limited outcome-6 hours, \$200USD, and an FFR number to process a case-hamper widespread clinical adoption. The requisite offsite handling of sensitive confidential patient information and their associated medical conditions is highly delicate issue involving IT-security, potential for data abuse, and other issues. In terms of FFR-CT calculation, our platform *InVascular* is capable to be faster, less costly and capable of providing more hemodynamic information and thus suitable for clinical setting. Due to the suitability of LBM for GPU parallel computing, *InVascular* features with exceptionally fast computation speed. With a great potential to further acceleration through parallel optimization and/or multiple GPU cards, the current computation time is around 10 minutes per cardiac cycle. Such a computation capability is critically important for clinical use, enabling massive numerical analysis

though parametrization to assess the true degree of an existing of an existing arterial stenosis. It is believed that *InVascular* which is expected to provide reliable therapeutic guidelines within 30 minutes after the radiological imaging data are available, is promising for these medical application. In summary *InVascular* is a novel and reliable means for noninvasive and patient-specific assessment of RAS and CAS severity that might help to guide therapeutic interventions. The assessment can be completed at the clinical site in a short period of time. It may provide a robust and low cost means of determining a significant stenosis in the arterial system which can then be used to drive medical verses interventional care. It is a robust technique that may be able to quantify the expected results of vascular intervention before they are done.

REFERENCES

REFERENCES

- [1] Robert D Safian and Stephen C Textor. Renal-artery stenosis. *New England Journal of Medicine*, 344(6):431–442, 2001.
- [2] L Barajas. Anatomy of the juxtaglomerular apparatus. *American Journal of Physiology-Renal Physiology*, 237(5):F333–F343, 1979.
- [3] Bruce M Koeppen and Bruce A Stanton. *Renal Physiology E-Book: Mosby Physiology Monograph Series (with Student Consult Online Access)*. Elsevier Health Sciences, 2012.
- [4] Astral Investigators. Revascularization versus medical therapy for renal-artery stenosis. *New England Journal of Medicine*, 361(20):1953–1962, 2009.
- [5] Liesbeth Bax, Arend-Jan J Woittiez, Hans J Kouwenberg, Willem PTM Mali, Erik Buskens, Frederik JA Beek, Branko Braam, Frans TM Huysmans, Leo J Schultze Kool, Matthieu JCM Rutten, et al. Stent placement in patients with atherosclerotic renal artery stenosis and impaired renal function: a randomized trial. *Annals of internal medicine*, 150(12):840–848, 2009.
- [6] Christopher J Cooper, Timothy P Murphy, Donald E Cutlip, Kenneth Jamerson, William Henrich, Diane M Reid, David J Cohen, Alan H Matsumoto, Michael Steffes, Michael R Jaff, et al. Stenting and medical therapy for atherosclerotic renal-artery stenosis. *New England Journal of Medicine*, 370(1):13–22, 2014.
- [7] IV Mohan and V Bourke. The management of renal artery stenosis: an alternative interpretation of astral and coral. *European Journal of Vascular and Endovascular Surgery*, 49(4):465–473, 2015.
- [8] Jeffrey W Olin, Marion R Piedmonte, Jess R Young, Susan DeAnna, Michael Grubb, and Mary Beth Childs. The utility of duplex ultrasound scanning of the renal arteries for diagnosing significant renal artery stenosis. *Annals of internal medicine*, 122(11):833–838, 1995.
- [9] Fabio Mangiacapra, Catalina Trana, Giovanna Sarno, Giedrius Davidavicius, Marcin Protasiewicz, Olivier Muller, Argyrios Ntalianis, Nerijus Misonis, Bruno Van Vlem, Guy R Heyndrickx, et al. Translesional pressure gradients to predict blood pressure response after renal artery stenting in patients with renovascular hypertension. *Circulation: Cardiovascular Interventions*, 3(6):537–542, 2010.
- [10] JH Rundback, D Sacks, KC Kent, C Cooper, D Jones, T Murphy, K Rosenfield, C White, M Bettmann, S Cortell, et al. Aha councils on cardiovascular radiology, high blood pressure research, kidney in cardiovascular disease, cardio-thoracic and vascular surgery, and clinical cardiology, and the society of interventional radiology fda device forum committee. american heart association. guidelines for the reporting of renal artery revascularization in clinical trials. *Circulation*, 106(12):1572–1585, 2002.

- [11] Nico HJ Pijls, Bernard De Bruyne, Kathinka Peels, Pepijn H Van Der Voort, Hans JRM Bonnier, Jozef Bartunek, and Jacques J Koolen. Measurement of fractional flow reserve to assess the functional severity of coronary-artery stenoses. *New England Journal of Medicine*, 334(26):1703–1708, 1996.
- [12] Jason A Mitchell, Rajesh Subramanian, Christopher J White, Peter A Soukas, Yaron Almagor, Richard E Stewart, and Kenneth Rosenfield. Predicting blood pressure improvement in hypertensive patients after renal artery stent placement: renal fractional flow reserve. *Catheterization and Cardiovascular Interventions*, 69(5):685–689, 2007.
- [13] Jean-Paul Beregi, Claire Mounier-Vehier, Patrick Devos, Corinne Gautier, Christian Libersa, Eugene P McFadden, and Alain Carre. Doppler flow wire evaluation of renal blood flow reserve in hypertensive patients with normal renal arteries. *Cardiovascular and interventional radiology*, 23(5):340–346, 2000.
- [14] Ganesh Manoharan, Nico HJ Pijls, Norbert Lameire, Katia Verhamme, Guy R Heyndrickx, Emanuele Barbato, William Wijns, Juraj Madaric, Xanden Tielbeebe, Jozef Bartunek, et al. Assessment of renal flow and flow reserve in humans. *Journal of the American College of Cardiology*, 47(3):620–625, 2006.
- [15] Noah J Jones, Eric R Bates, Stanley J Chetcuti, Robert J Lederman, and P Michael Grossman. Usefulness of translesional pressure gradient and pharmacological provocation for the assessment of intermediate renal artery disease. *Catheterization and cardiovascular interventions*, 68(3):429–434, 2006.
- [16] Rajesh Subramanian, Christopher J White, Kenneth Rosenfield, Riyaz Bashir, Yaron Almagor, David Meerkin, and Evgeny Shalman. Renal fractional flow reserve: a hemodynamic evaluation of moderate renal artery stenoses. *Catheterization and cardiovascular interventions*, 64(4):480–486, 2005.
- [17] Jacek Kadziela, Andrzej Januszewicz, Aleksander Prejbisz, Ilona Michałowska, Magdalena Januszewicz, Elżbieta Florczak, Łukasz Kalińczuk, Bożena Norwa-Otto, Ewa Warchoń, and Adam Witkowski. Prognostic value of renal fractional flow reserve in blood pressure response after renal artery stenting (prefer study). *Cardiology journal*, 20(4):418–422, 2013.
- [18] B Frauchiger, R Zierler, RO Bergelin, JA Isaacson, and DE Strandness Jr. Prognostic significance of intrarenal resistance indices in patients with renal artery interventions: a preliminary duplex sonographic study. *Cardiovascular Surgery*, 4(3):324–330, 1996.
- [19] Wayne Rosamond. American heart association statistics committee and stroke statistics subcommittee. heart disease and stroke statistics-2007 update: a report from the american heart association statistics committee and stroke statistics subcommittee. *Circulation*, 115:e69–e171, 2007.
- [20] Erling Falk. Plaque rupture with severe pre-existing stenosis precipitating coronary thrombosis. characteristics of coronary atherosclerotic plaques underlying fatal occlusive thrombi. *Heart*, 50(2):127–134, 1983.
- [21] Task Force Members, Gilles Montalescot, Udo Sechtem, Stephan Achenbach, Felicita Andreotti, Chris Arden, Andrzej Budaj, Raffaele Bugiardini, Filippo Crea, Thomas Cuisset, et al. 2013 esc guidelines on the management of stable

- coronary artery disease: the task force on the management of stable coronary artery disease of the european society of cardiology. *European heart journal*, 34(38):2949–3003, 2013.
- [22] Manesh R Patel, Eric D Peterson, David Dai, J Matthew Brennan, Rita F Redberg, H Vernon Anderson, Ralph G Brindis, and Pamela S Douglas. Low diagnostic yield of elective coronary angiography. *New England Journal of Medicine*, 362(10):886–895, 2010.
- [23] W Bob Meijboom, Carlos AG Van Mieghem, Niels van Pelt, Annick Weustink, Francesca Pugliese, Nico R Mollet, Eric Boersma, Eveline Regar, Robert J van Geuns, Peter J de Jaegere, et al. Comprehensive assessment of coronary artery stenoses: computed tomography coronary angiography versus conventional coronary angiography and correlation with fractional flow reserve in patients with stable angina. *Journal of the American College of Cardiology*, 52(8):636–643, 2008.
- [24] Bernard De Bruyne, Nico HJ Pijls, Bindu Kalesan, Emanuele Barbato, Pim AL Tonino, Zsolt Piroth, Nikola Jagic, Sven Möbius-Winkler, Gilles Rioufol, Nils Witt, et al. Fractional flow reserve–guided pci versus medical therapy in stable coronary disease. *New England Journal of Medicine*, 367(11):991–1001, 2012.
- [25] Nils P Johnson, Gábor G Tóth, Dejian Lai, Hongjian Zhu, Göksel Açar, Pierfrancesco Agostoni, Yolande Appelman, Fatih Arslan, Emanuele Barbato, Shao-Liang Chen, et al. Prognostic value of fractional flow reserve: linking physiologic severity to clinical outcomes. *Journal of the American College of Cardiology*, 64(16):1641–1654, 2014.
- [26] Nico HJ Pijls, Pepijn van Schaardenburgh, Ganesh Manoharan, Eric Boersma, Jan-Willem Bech, Marcel van’t Veer, Frits Bär, Jan Hoorntje, Jacques Koolen, William Wijns, et al. Percutaneous coronary intervention of functionally non-significant stenosis: 5-year follow-up of the defer study. *Journal of the American College of Cardiology*, 49(21):2105–2111, 2007.
- [27] Pim AL Tonino, Bernard De Bruyne, Nico HJ Pijls, Uwe Siebert, Fumiaki Ikeno, Marcel vant Veer, Volker Klauss, Ganesh Manoharan, Thomas Engstrøm, Keith G Oldroyd, et al. Fractional flow reserve versus angiography for guiding percutaneous coronary intervention. *New England Journal of Medicine*, 360(3):213–224, 2009.
- [28] Rou Chen, Huidan Yu, and Likun Zhu. Effects of initial conditions on the coalescence of micro-bubbles. *Proceedings of the Institution of Mechanical Engineers, Part C: Journal of Mechanical Engineering Science*, 232(3):457–465, 2018.
- [29] Alan Sawchuk, Raveena Patil, Hongkun Zhu, Huidan Yu, Raghunandan Motaganahalli, and Michael Dalsing. Noninvasive measurement of renovascular resistance and the meaning and limitations of the renal resistance index. *Journal of Vascular Surgery*, 64(3):876–877, 2016.
- [30] Huidan W YU, Anurag Deb, Xi Chen, Rou Chen, Dongfang Wang, and I-Wen Wang. A non-invasive technique for fast assessment of optimal lvad outflow graft implant sites. *Circulation Research*, 121(suppl_1):A221–A221, 2017.

- [31] Alison L Marsden and Mahdi Esmaily-Moghadam. Multiscale modeling of cardiovascular flows for clinical decision support. *Applied Mechanics Reviews*, 67(3):030804, 2015.
- [32] Christian Tesche, Carlo N De Cecco, Moritz H Albrecht, Taylor M Duguay, Richard R Bayer, Sheldon E Litwin, Daniel H Steinberg, and U Joseph Schoepf. Coronary ct angiography-derived fractional flow reserve. *Radiology*, 285(1):17–33, 2017.
- [33] Liang Zhong, Jun-Mei Zhang, Boyang Su, Ru San Tan, John C Allen, and Ghas-san S Kassab. Application of patient-specific computational fluid dynamics in coronary and intra-cardiac flow simulations: Challenges and opportunities. *Frontiers in physiology*, 9, 2018.
- [34] Otto VanGeet et al. Best practices guide for energy-efficient data center design. Technical report, EERE Publication and Product Library, 2010.
- [35] MB Liu and GR Liu. Smoothed particle hydrodynamics (sph): an overview and recent developments. *Archives of computational methods in engineering*, 17(1):25–76, 2010.
- [36] Huidan Yu, Xi Chen, Zhiqiang Wang, Debanjan Deep, Everton Lima, Ye Zhao, and Shawn D Teague. Mass-conserved volumetric lattice boltzmann method for complex flows with willfully moving boundaries. *Physical Review E*, 89(6):063304, 2014.
- [37] Luca Formaggia, Daniele Lamponi, and Alfio Quarteroni. One-dimensional models for blood flow in arteries. *Journal of engineering mathematics*, 47(3-4):251–276, 2003.
- [38] Irene E Vignon-Clementel, CA Figueroa, KE Jansen, and CA Taylor. Outflow boundary conditions for 3d simulations of non-periodic blood flow and pressure fields in deformable arteries. *Computer methods in biomechanics and biomedical engineering*, 13(5):625–640, 2010.
- [39] Irene E Vignon-Clementel, C Alberto Figueroa, Kenneth E Jansen, and Charles A Taylor. Outflow boundary conditions for three-dimensional finite element modeling of blood flow and pressure in arteries. *Computer methods in applied mechanics and engineering*, 195(29-32):3776–3796, 2006.
- [40] Irene E Vignon-Clementel, Alison L Marsden, and Jeffrey A Feinstein. A primer on computational simulation in congenital heart disease for the clinician. *Progress in Pediatric Cardiology*, 30(1-2):3–13, 2010.
- [41] J Alastruey, KH Parker, J Peiró, and SJ Sherwin. Lumped parameter outflow models for 1-d blood flow simulations: effect on pulse waves and parameter estimation. *Communications in Computational Physics*, 4(2):317–336, 2008.
- [42] N Stergiopulos, DF Young, and TR Rogge. Computer simulation of arterial flow with applications to arterial and aortic stenoses. *Journal of biomechanics*, 25(12):1477–1488, 1992.
- [43] Philippe Reymond, Fabrice Merenda, Fabienne Perren, Daniel Rufenacht, and Nikos Stergiopulos. Validation of a one-dimensional model of the systemic arterial tree. *American Journal of Physiology-Heart and Circulatory Physiology*, 297(1):H208–H222, 2009.

- [44] Mirko Bonfanti, Stavroula Balabani, John P Greenwood, Sapna Puppala, Sherwanthi Homer-Vanniasinkam, and Vanessa Díaz-Zuccarini. Computational tools for clinical support: a multi-scale compliant model for haemodynamic simulations in an aortic dissection based on multi-modal imaging data. *Journal of The Royal Society Interface*, 14(136):20170632, 2017.
- [45] S Pirola, Z Cheng, OA Jarral, DP O’Regan, JR Pepper, T Athanasiou, and XY Xu. On the choice of outlet boundary conditions for patient-specific analysis of aortic flow using computational fluid dynamics. *Journal of biomechanics*, 60:15–21, 2017.
- [46] Umberto Morbiducci, Diego Gallo, Diana Massai, Filippo Consolo, Raffaele Ponzini, Luca Antiga, Cristina Bignardi, Marco A Deriu, and Alberto Redaelli. Outflow conditions for image-based hemodynamic models of the carotid bifurcation: implications for indicators of abnormal flow. *Journal of biomechanical engineering*, 132(9):091005, 2010.
- [47] S Succi, E Foti, and F Higuera. Three-dimensional flows in complex geometries with the lattice boltzmann method. *EPL (Europhysics Letters)*, 10(5):433, 1989.
- [48] Roberto Benzi, Sauro Succi, and Massimo Vergassola. The lattice boltzmann equation: theory and applications. *Physics Reports*, 222(3):145–197, 1992.
- [49] Senyou An, Huidan Whitney Yu, and Jun Yao. Gpu-accelerated volumetric lattice boltzmann method for porous media flow. *Journal of Petroleum Science and Engineering*, 156:546–552, 2017.
- [50] Rou Chen, Huidan Whitney Yu, Likun Zhu, Raveena M Patil, and Taehun Lee. Spatial and temporal scaling of unequal microbubble coalescence. *AIChE Journal*, 63(4):1441–1450, 2017.
- [51] Zhiqiang Wang, Ye Zhao, Alan P Sawchuck, Michael C Dalsing, and Huidan Whitney Yu. Gpu acceleration of volumetric lattice boltzmann method for patient-specific computational hemodynamics. *Computers & Fluids*, 115:192–200, 2015.
- [52] Kartik Jain, Jingfeng Jiang, Charles Strother, and Kent-André Mardal. Transitional hemodynamics in intracranial aneurysms—comparative velocity investigations with high resolution lattice boltzmann simulations, normal resolution ansys simulations, and mr imaging. *Medical physics*, 43(11):6186–6198, 2016.
- [53] Derek Groen, Robin A Richardson, Rachel Coy, Ulf D Schiller, Hoskote Chandrashekar, Fergus Robertson, and Peter V Coveney. Validation of patient-specific cerebral blood flow simulation using transcranial doppler measurements. *Frontiers in physiology*, 9, 2018.
- [54] Hanieh Mirzaee, Thomas Henn, Mathias J Krause, Leonid Goubergrits, Christian Schumann, Mathias Neugebauer, Titus Kuehne, Tobias Preusser, and Anja Hennemuth. Mri-based computational hemodynamics in patients with aortic coarctation using the lattice boltzmann methods: Clinical validation study. *Journal of Magnetic Resonance Imaging*, 45(1):139–146, 2017.
- [55] N Hafizah Mokhtar, Aizat Abas, NA Razak, Muhammad Najib Abdul Hamid, and Soon Lay Teong. Effect of different stent configurations using lattice boltzmann method and particles image velocimetry on artery bifurcation aneurysm problem. *Journal of theoretical biology*, 433:73–84, 2017.

- [56] Xiuying Kang, Wenwen Tang, and Siyuan Liu. Lattice boltzmann method for simulating disturbed hemodynamic characteristics of blood flow in stenosed human carotid bifurcation. *Journal of Fluids Engineering*, 138(12):121104, 2016.
- [57] Alan P Sawchuk, Monsurul Khan, Anurag Deb, Raghu L Motaganahalli, Xin Fang, Fangke Chen, and Huidan Whitney Yu. Noninvasive and patient-specific assessment of true severity of renal artery stenosis for new guidelines for planning stent therapy. *Journal of Vascular Surgery*, 68(3):e64–e65, 2018.
- [58] Huidan W Yu, Xi Chen, Zhiqiang Wang, Rou Chen, Chen Lin, Stephen F Kralik, and Raveena Patil. Integration of patient-specific computational hemodynamics and vessel wall shear stress into mri diagnosis of vascular diseases. *Circulation Research*, 119(suppl_1):A235–A235, 2016.
- [59] Nico Westerhof, Jan-Willem Lankhaar, and Berend E Westerhof. The arterial windkessel. *Medical & biological engineering & computing*, 47(2):131–141, 2009.
- [60] HJ Kim, IE Vignon-Clementel, JS Coogan, CA Figueroa, KE Jansen, and CA Taylor. Patient-specific modeling of blood flow and pressure in human coronary arteries. *Annals of biomedical engineering*, 38(10):3195–3209, 2010.
- [61] Dibyendu Sengupta, Andrew M Kahn, Jane C Burns, Sethuraman Sankaran, Shawn C Shadden, and Alison L Marsden. Image-based modeling of hemodynamics in coronary artery aneurysms caused by kawasaki disease. *Biomechanics and modeling in mechanobiology*, 11(6):915–932, 2012.
- [62] Hugo G Bogren, Richard H Klipstein, David N Firmin, Raad H Mohiaddin, S Richard Underwood, R Simon O Rees, and Donald B Longmore. Quantitation of antegrade and retrograde blood flow in the human aorta by magnetic resonance velocity mapping. *American heart journal*, 117(6):1214–1222, 1989.
- [63] Kevin R Johnson, Salil J Patel, Amy Whigham, Alex Hakim, Roderic I Pettigrew, and John N Oshinski. Three-dimensional, time-resolved motion of the coronary arteries. *Journal of Cardiovascular Magnetic Resonance*, 6(3):663–673, 2004.
- [64] Simvascular web page. <http://simvascular.github.io/index.html>.
- [65] Rolf Holenstein and David N Ku. Reverse flow in the major infrarenal vessels—a capacitive phenomenon. *Biorheology*, 25(6):835–842, 1988.
- [66] Andrea S Les, Shawn C Shadden, C Alberto Figueroa, Jinha M Park, Maureen M Tedesco, Robert J Herfkens, Ronald L Dalman, and Charles A Taylor. Quantification of hemodynamics in abdominal aortic aneurysms during rest and exercise using magnetic resonance imaging and computational fluid dynamics. *Annals of biomedical engineering*, 38(4):1288–1313, 2010.

VITA

VITA

Md Monsurul Islam khan received Bachelor of Science in Mechanical Engineering with Honors from Bangladesh University of Engineering and technology. During his bachelor degree, he received university merit scholarship for seven semester and was awarded Dean's Listed for 3 academic year of undergraduate study. After completing BSc. he joined Military Institute of Science and Technology as a lecturer in the Dept. of Nuclear Engineering. He joined Purdue University as a recipient of MS university fellowship for year of 2017-2018. In his master program, Mr. Khan has achieved a perfect GPA of 4.0 (out of 4.0 scale) with grade A+ in every single course he took. His research achievements include 5 journal papers, one published (2nd author), two accepted (1st and 3rd author), and two in review (1st author), and 4 conference papers (1st or 2nd author). His MS degree is expected in summer 2019.